ANALYSIS OF JET ENGINE INLETS

Annual Report

J. L. Volakis
H. Anastassiu
D. Ross

Wright Laboratories/AARA
Wright Patterson AFB
OHIO 45433-7001

Veda, Inc
Suite 200
5200 Springfield Pike
Dayton, OH 45431

December 1994

030395-6-T
December 1994

ANALYSIS OF JET ENGINE INLETS

Annual Report

John L. Volakis
Hristos T. Anastassiu
Daniel C. Ross

Radiation Laboratory
Electrical Engineering and Computer Science Dept.
University of Michigan
1301 Beal Ave.
Ann Arbor, MI 48109-2122

volakis@engin.umich.edu
dross@engin.umich.edu
hristosa@engin.umich.edu
Phone: (313)764-0500
Fax:(313)747-2106

Background and Executive Summary

The University of Michigan activity on the electromagnetic characterization of jet engine inlets began in January 1993 with the goal of developing robust hybrid methods for the electromagnetic analysis of cavities terminated with jet engines, i.e. cavities terminated with an array of blades which normally form the compressor of the engine configuration. Since high frequency techniques cannot be used for the characterization of the complex engine face, our method of analysis called for a hybrid approach. Specifically, we proposed to use a numerical method for modeling the engine face and a well known high frequency method for propagating the fields to and from the engine face. Among some of the obvious challenges to be confronted in this implementation were

- Large Computational Domains (actual engine is 10-50λ in diameter).
- Complexity of the Engine Face.
- Lack of Experience in Interfacing Numerical and High Frequency Methods.
- Lack of Validation/Reference Data.

The lack of any reference data was a major impediment from the start of the project and to address this issue we initiated a parallel effort aimed at developing solutions and scattering data for simplistic engine-type of configurations. This effort proved invaluable to the whole process and led to the development of reference codes and data used by the entire cavity-team of the NCTI project for validating the numerical codes. Three reference geometries (see Fig. 1) were considered using the Mode-Matching method and one of these involved a class of curved blades which to a reasonable degree could approximate actual blade configurations(see Fig. 2). Therefore, this Mode-Matching code can be used as a first order model in simulating the engine front. Also, the success of the Mode-Matching code influenced the construction of measurement models which were within the modeling capability of the available software. This report is the first to present comparisons of measured and computed data

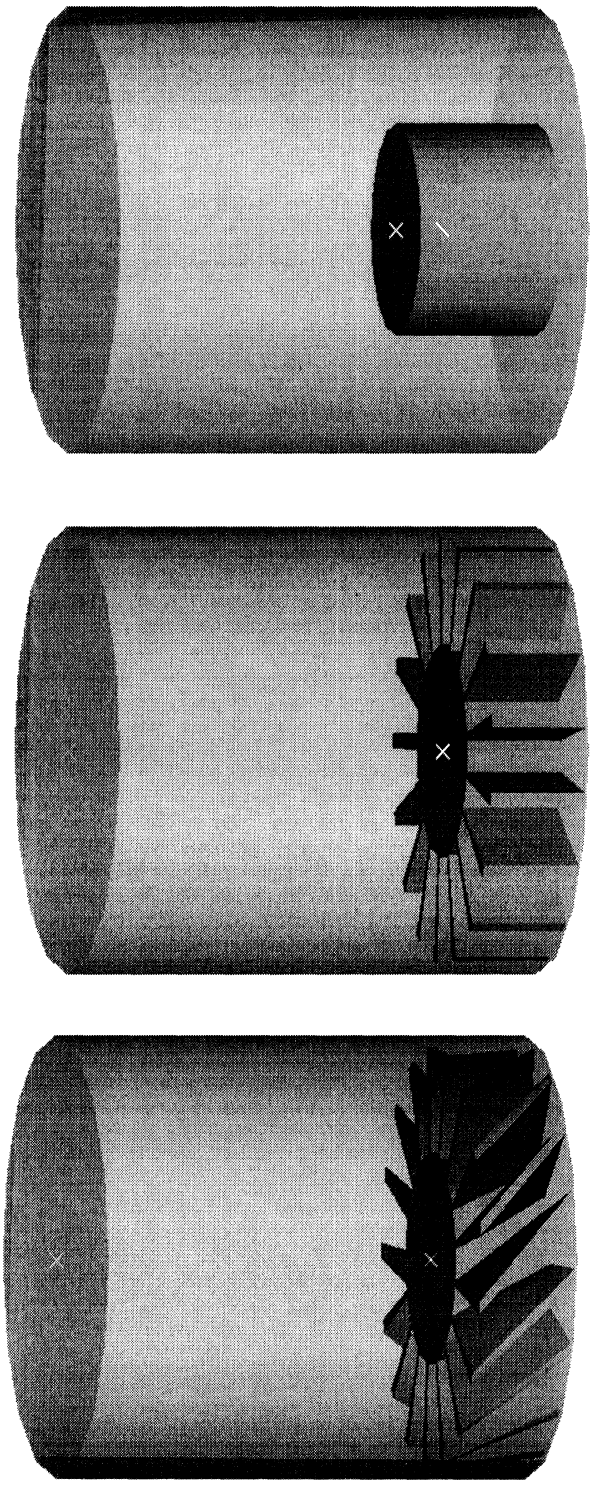

Figure 1. Geometries analyzed using the Mode-Matching method in conjunction with the generalized telegraphists equations

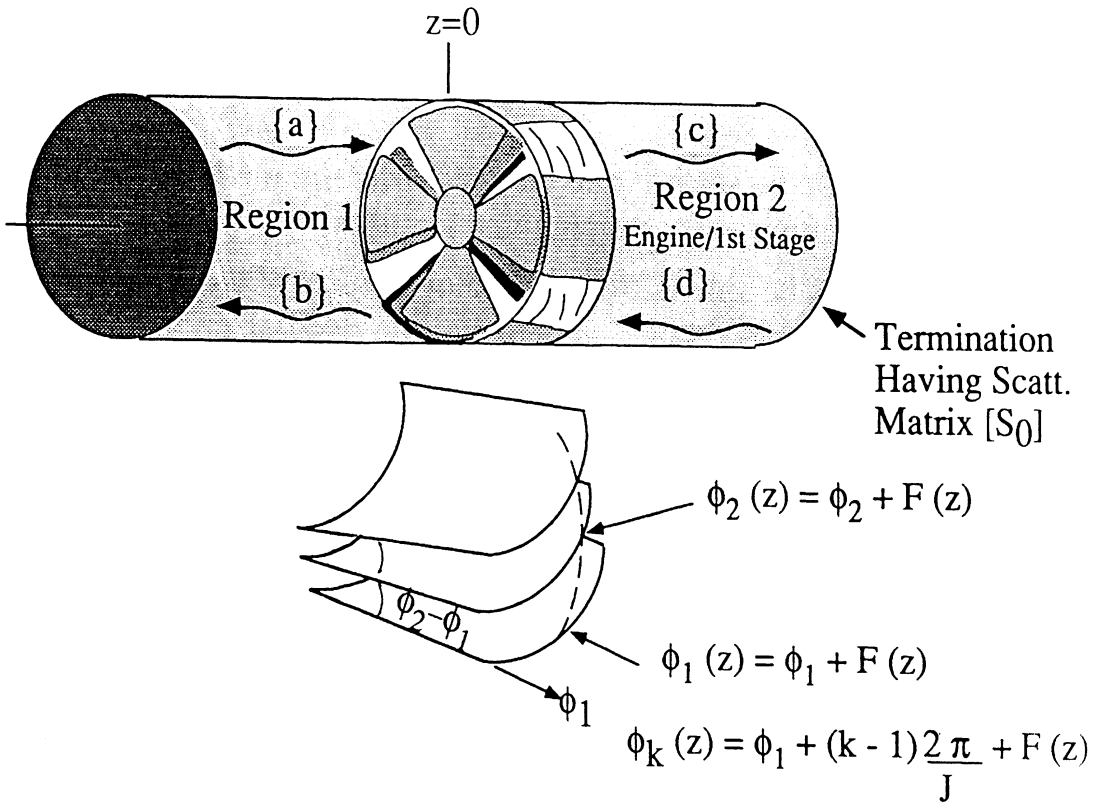

Figure 2. Definition and illustration of the engine blades analyzed via the GTE-MM method.

for engine-like blade configurations such as those shown in Fig. 3 and 4. These configurations were designed at the University of Michigan and were measured at the General Electric Aircraft Engine Co., Cincinnati, Ohio. The agreement between measured and calculated data is relatively quite good for the straight as well as curved blade terminations. Configuration with up to 10λ in diameter were considered and in all cases good agreement was observed demonstrating that the code is ready for release. To our knowledge this is the first validation for curved blade analysis and represent a most important accomplishment.

Our initial effort in developing a general-purpose code for engine analysis was based on a hybrid finite element method described in [1]. This FEM-Modal method allows for the isolated analysis of the engine configuration whereas the fields in the inlet region can be analyzed using a ray-technique such as the Shooting and Bouncing Ray (SBR) method or the Generalized Ray Expansion (GRE) method. Thus, the developed hybrid method allows for the interface of different analysis methods with the hand-off between the two computational regions taking place at a surface near the engine face as illustrated in Fig. 5. Several challenges had to be overcome in

specializing the FEM to engine analysis. Among them, the mesh termination was the most difficult task and before this issue was adequately addressed a number of analytical and numerical absorbing boundary conditions were considered. Nevertheless, in spite of its adaptability, the FEM approach led to large computational domains and prohibitively large systems to be

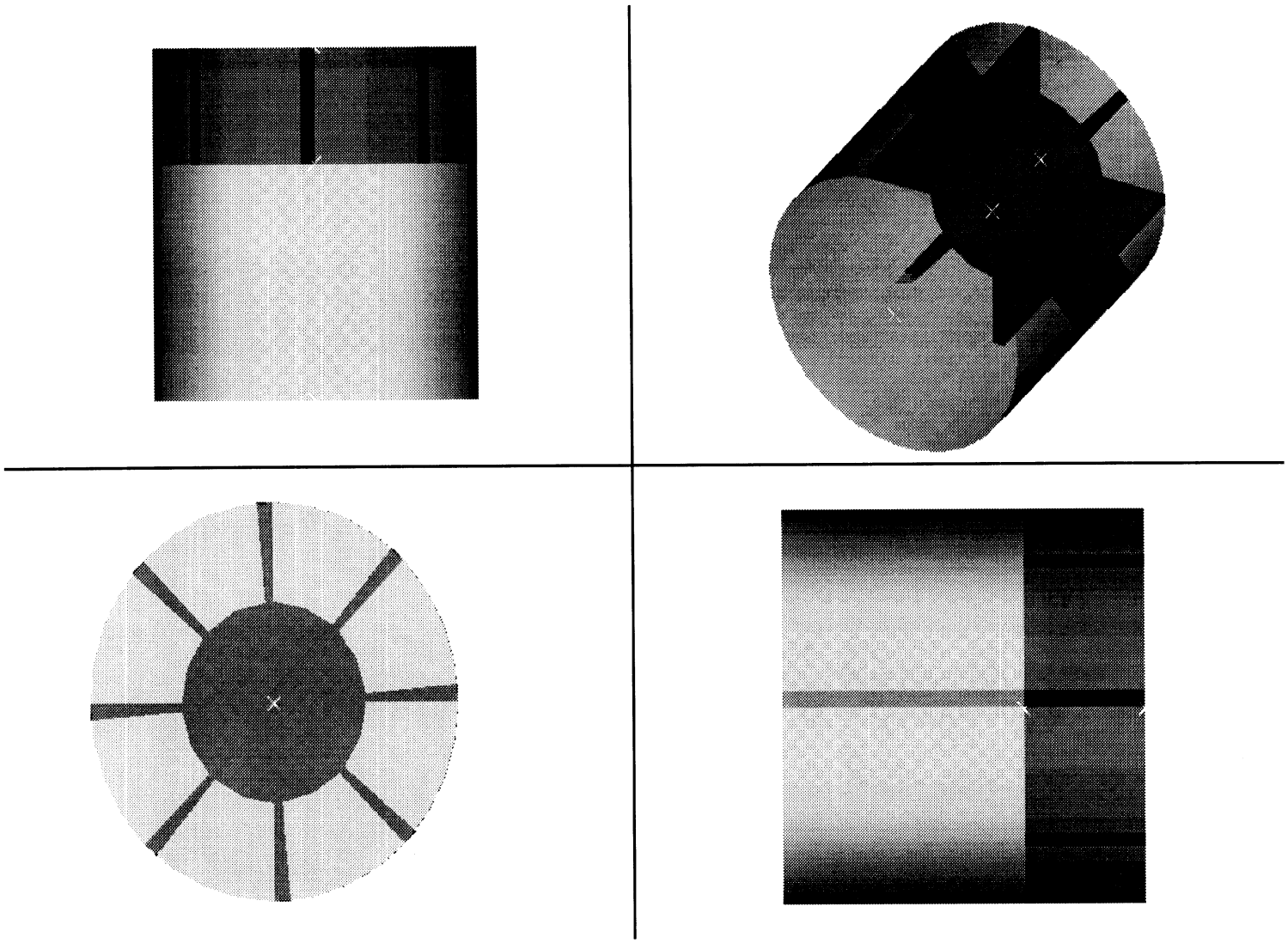

Figure 3. Different views of the straight blade termination geometry

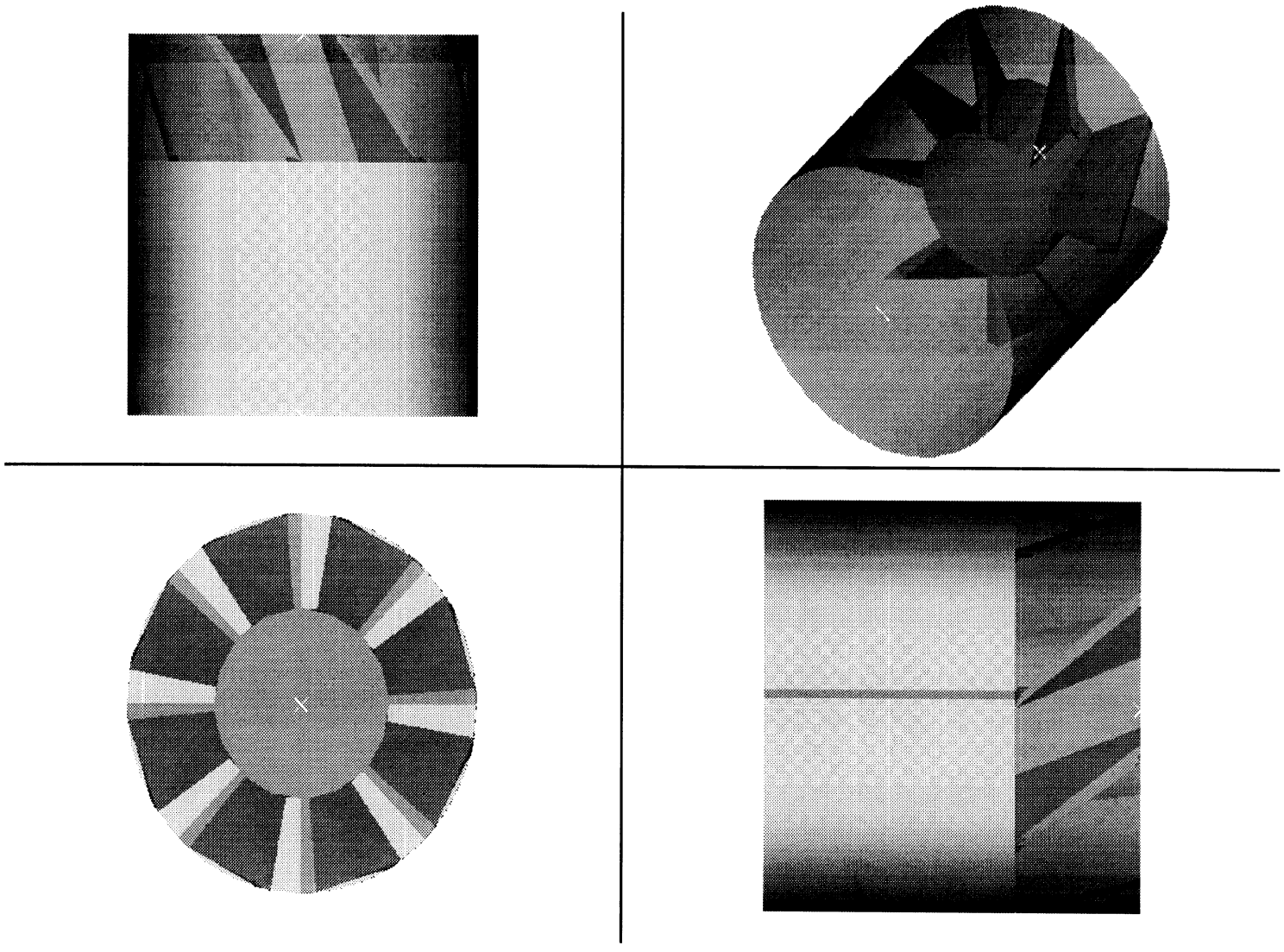

Figure 4. Different views of the curved blade termination geometry.

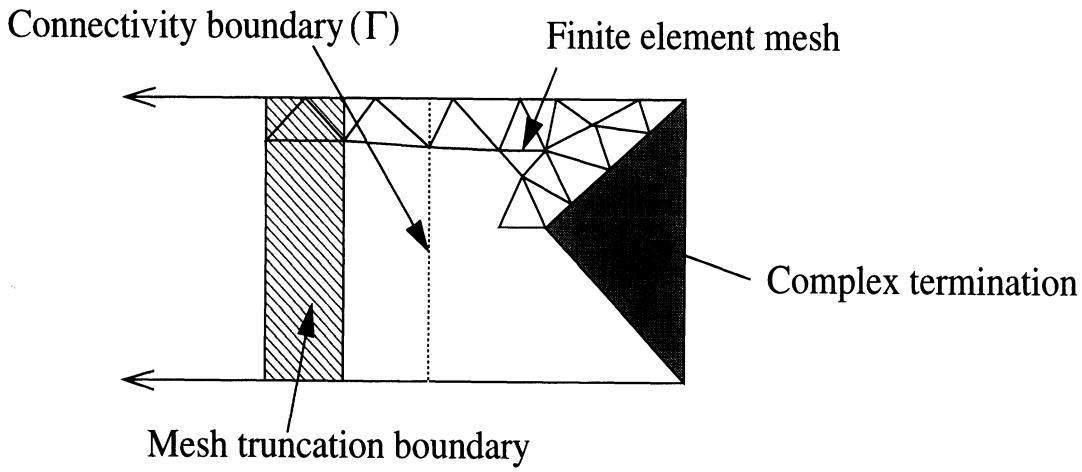

Figure 5. Decomposition of the jet engine inlet for application of the finite element-modal method. The hand-off surface is labeled as the connectivity boundary.

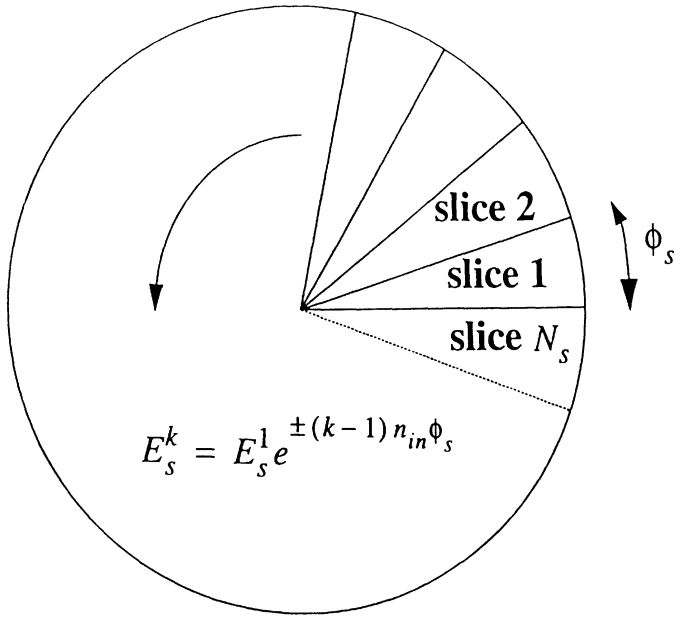

Figure 6. Slicing of the engine's periodic face. Since the modal fields among the slices differ only be a phase factor, the computational domain is reduced to a single slice or engine blade sector.

practical, even when implemented on current state-of-the-art parallel processors. This prompted us to look at alternative analysis approaches which exploit the inherent geometrical features of the engine face. Specifically, we proposed a periodic FEM analysis which reduced the computational domain to a periodic slice (see Fig. 6). This led to a dramatic reduction in computational cost and, more importantly, it revealed that the scattering matrix has a few non-zero elements which can be identified *a priori.* That is, each incoming modal field can only excite a limited number of modes whose mode number is known *a priori.* By exploiting this concept, the full three-dimensional engine structure can be analyzed much like a body of revolution and the computational complexity is essentially reduced from a three-dimensional to a two-dimensional level.

To fully exploit the physics of the engine periodicity, we again looked at an integral equation approach. The key to this approach is the use of a limited mode Green's function which includes only those modes known to be excited (includes propagating and evanescent modes) by the periodic engine configuration. A surface mesh is only required which spans one periodic cell (equivalent to a single blade) of the engine and the limited mode Green's function involves a single summation rather than a double sum. Consequently, this approach holds the promise of developing general-purpose large scale engine scattering codes.

Our major achievements during the past year are as follows:

- Introduced and developed the Mode-Matching analysis code for modeling a class of engine configurations.

- Validated analysis codes using measured data for the configurations in Fig. 3 and 4.

- Curved blade Mode-Matching is ready for interface with CAVERN and xpatch_ca.

- Exploited engine periodicity and developed a finite element code whose computational domain is limited to a single engine periodic cell.

- Developed an understanding of the scattering matrix scarcity structure and mode coupling characteristics.

- Introduced the limited mode model for engine analysis.

Our goals over the next year are as follows:

- Work with MDC to integrate the curved blade Mode-Matching code into xpatch_ca.

- Finalize development of the Limited Mode integral equation code.

  Code's computational domain will be limited to a single blade.

  Green's function will be a single sum.

  Code will have no restriction on blade geometry and any number of stages can be incorporated.

  Frequency shifting can be easily simulated without code re-execution.

  No memory limitations as expected

  Several basis functions will be investigated, including wavelets and other approaches to increase matrix scarcity, if necessary.

- Develop formulation for modeling non-metallic blades and other material sections of the engine structure as well as non-periodic discontinuities.

Report Structure

This contains four independent documents which are arranged in somewhat historical order. They are:

1. Hybrid Finite Element-Modal Analysis of Jet Engine Inlet Scattering
This document summarizes the theory and implementation of the hybrid finite element code and include results for small inlets. It summarizes earlier University of Michigan reports 030395-1-T and 030395-4-T. The document is scheduled to appear next year in the *IEEE Transactions on Antennas and Propagation*..

2. The Mode Matching Technique for Electromagnetic Scattering by Cylindrical Waveguides with Canonical Terminations.
This document summarize and updates earlier University of Michigan reports 030395-2-T and 030395-3-T. It describes the formulation of the Mode-Matching code and contains extensive validation data. Most importantly, it compares the Mode-Matching code's results with measurements based on the straight and curved blade terminations shown in Figures 3 and 4. This is a most important accomplishment since it represents the first validation of scattering analysis for curved blade terminations. The included validation demonstrates that the code can be released.

3. Overlapping Modal and Geometry Symmetries in the Simulation of Jet Engine Inlet Scattering
This document demonstrates how the computational domain of the finite element code can be reduced to a single periodic engine slice. It is shown that the scattering matrix is sparse and its non-zero elements can be pre-determined. A finite element code was written on the basis of this formulation and it was necessary to develop phase boundary conditions to close the computational domain of the slice. The requirement for coincident nodes on each face of the slice required special volume meshes. To avoid this requirement and to more fully exploit the scarcity of the scattering matrix we looked at the limited mode model described in the next document.

4. A Limited-Mode Model for Engine Face Analysis
This document described the limited mode model which fully exploits all aspects of the engine's overlapping geometrical and modal symmetries. It is demonstrated that a much simpler (single sum) Green's function can be used in conjunction with a surface (rather than a volume) formulation. The computational domain is again limited to a single engine slice and consequently this is our most efficient (to date) computational model. This approach does not carry restrictions on the engine geometry or material properties and a preliminary code has already been written. It remains to appropriately treat the Green's function's singularity before we begin full testing of the code.

Hybrid Finite Element-Modal Analysis of Jet Engine Inlet Scattering

Daniel C. Ross, John L. Volakis and Hristos T. Anastassiu

Radiation Laboratory

University of Michigan

Ann Arbor MI 48109-2122

abstract **--** With the goal of characterizing jet engine inlets, a hybrid finite element-modal formulation is presented for the analysis of cavities with complex terminations. The finite element method is used to find the generalized scattering matrix for an N-port representation of the complex termination, where N is the number of traveling modes in the cavity. The cavity is assumed to be circular at the termination (engine) but the remainder of the cavity can be of arbitrary cross section. The scattered fields are obtained by tracing the fields back out of the cavity via a high frequency or modal technique with the generalized scattering matrix used in determining the fields at an aperture near the irregular cavity termination. "Proof of concept" results are presented and several issues relating to the implementation of the FEM are addressed. Among these, a new artificial absorber is developed for terminating the FEM mesh and the suitability of edge or node based elements is examined.

1.0 Introduction

The simulation of radar scattering from jet engine inlets is an important step towards the characterization of aircraft structures. While high frequency techniques can accurately simulate many scattering mechanisms on a typical aircraft, these techniques are not suitable for resonant or guiding structures such as antennas/radomes and jet engine inlets. The engine face is an intricate target, possessing complex geometrical features at the wavelength level or less, and is therefore inappropriate for high frequency analysis. By comparison, the finite element method (FEM) [1][2] is well suited for the analysis of geometrically complex, inhomogeneous volumetric targets such as the engine face. However, in spite of its inherent O(n) storage demand, the FEM analysis would still require prohibitive computational resources were it to be also used for modeling the volume enclosed by the inlet leading to the engine. To overcome this difficulty, in this paper we describe a new hybrid finite element method for the analysis of the inlet-engine configuration.

The proposed hybrid FEM was originally proposed in [3] and combines ray techniques (for propagating the field to and from the engine face) and the FEM (for computing the fields scattered from the engine face). Figure 1 shows the regions to be characterized either by the finite element method or some high frequency technique. Obviously, the high frequency method is best suited for modeling the fields in the large cavity region between the inlet mouth and the engine face. Any of the well known ray methods such as the shooting and bouncing ray (SBR) [4], the generalized ray expansion (GRE) [5] or even a modal decomposition technique can be used for coupling the fields into the inlet region and guiding them from the inlet mouth to the engine face. The same ray or modal technique can also be used for propagating the fields scattered by the engine back out of the inlet.

Of importance in this analysis is the interface between the ray/modal and FEM methods, and the truncation of the finite element mesh. Given that the inlet cross section near and at the engine location is circular, and our desire to propose an efficient and flexible coupling scheme, the coupling of the FEM and ray fields in this paper is accomplished via the generalized modal scattering matrix. That is, the FEM analysis generates the modal scattering matrix which can then be interfaced with any high frequency technique for computing the engine scattered fields without reference to the geometry of the jet engine. Regarding the truncation of the FEM mesh, several schemes are considered including absorbing bound-

ary conditions, the unimoment method and a new artificial broadband absorber, with the later found most effective for this application.

The paper begins with a section describing the proposed hybrid FEM method, termed as the FEM-modal method because it generates the modal scattering matrix. This section describes the role of the modal scattering matrix for interfacing with the FEM and ray techniques used for propagating the fields to and from the engine face. The next sections discuss implementation issues of the FEM technique including elements, application of boundary conditions and truncation of the FEM mesh. Finally, results are presented for three different inlet terminations. These terminations are rather simple and serve to validate the proposed hybrid FEM-modal methods since reference calculations using different techniques are available. Given that the emphasis of the paper is on the development of the FEM-modal technique and not on the inlet field propagator, calculations refer to straight circular inlets. However, the inherent flexibility of the generalized scattering matrix allows the characterization of the same inlet terminations connected to different inlet geometries.

2.0 Finite Element-Modal Formulation

Consider the three-dimensional cavity configuration shown in Figure 1. The cavity is excited by an arbitrary field (typically a plane wave) through its opening at the left side and is assumed to have a complex geometrical configuration (an engine) at its right end. We are interested in computing the field scattered by this complex cavity termination due to a given excitation which is assumed to be specified at the left opening of the cavity. In our analysis, the cross section of the cavity is assumed to be arbitrary and of diameter greater than a free space wavelength up to the connectivity boundary as shown in Figure 1. Beyond this connectivity boundary, the cavity's outer perimeter is assumed to be circular but may enclose complex geometrical configurations such as an engine.

In accordance with the proposed hybrid FEM-modal formulation, the fields entering the left opening of the inlet will be modeled and propagated up to the connectivity boundary using some ray technique (such as the SBR [4] and the GRE [5] or modal method [6]) These techniques are well understood and this paper is not concerned with their description and implementation. Instead, our emphasis is on the proposed techniques for modeling the complex cavity termination and coupling of the fields associated with the different

techniques at the connectivity boundary. As noted earlier, the FEM will be used to model the fields in the vicinity of the complex cavity termination (i.e. to the right of the connection boundary). We could indeed use the modal or ray techniques to generate the excitation to the FEM system of equations. However, this approach would require the solution of the FEM system for each field excitation, a rather inefficient way of characterizing the interior cavity scattering at all incidence angles of the impinging plane wave. Instead, given that the cavity is circular at the connectivity boundary, a convenient way to characterize the termination is by determining its generalized modal scattering matrix. Since each field distribution at the connectivity boundary can be expressed as a sum of incoming (or outgoing) cylindrical waveguide modes, the modal scattering matrix provides us with a unique method for characterizing the cavity termination without consideration of the technique used for modeling the fields to the left or right of the connectivity boundary.

The generalized scattering matrix $[S]$ of a given termination relates the coefficients of the incoming modes to the coefficients of the corresponding outgoing modes. That is

$$[S]\{a\} = \{b\} \tag{1}$$

where the elements of the vectors $\{a\}$ and $\{b\}$ are simply the coefficients of the incoming and outgoing modes respectively. They are defined by

$$a_m = \frac{\int_\Gamma \bar{e}^{inc}(x, y, z_0) \cdot \bar{\Psi}^*_m(x, y, z_0)\, ds}{\int_\Gamma \bar{\Psi}_m(x, y, z_0) \cdot \bar{\Psi}^*_m(x, y, z_0)\, ds} \tag{2}$$

$$b_m = \frac{\int_\Gamma \bar{e}^{s}(x, y, z_0) \cdot \bar{\Psi}^{s*}_m(x, y, z_0)\, ds}{\int_\Gamma \bar{\Psi}^{s}_m(x, y, z_0) \cdot \bar{\Psi}^{s*}_m(x, y, z_0)\, ds} \tag{3}$$

for $m = 1, 2, 3, \ldots N$, in which $\bar{e}^{inc}$ and $\bar{e}^{s}$ are the incident and scattered transverse electric fields respectively, on the connectivity boundary surface Γ, and $\bar{\Psi}_m$ denotes the mode functions of the circular waveguide of a given radius. A single mode index is used to compactly represent the totality of the even/odd, TE or TM modes, each of which is associated with indices n and p. Additionally, each Ψ_m is an odd/even pair, having either $\sin[n\varphi]$ or $\cos[n\varphi]$ angular dependance.

In accordance with the proposed FEM-modal method, the entries of the generalized scattering matrix are computed from the solution of the FEM system. More specifically, the FEM solution proceeds as follows:

Given that the cavity accommodates N traveling modes

(a) Use the q'th mode as the excitation

(b) Find a_q at the connectivity boundary Γ

(c) Solve the finite element system to find the scattered field

(d) Calculate the inner product of the scattered field with each out-going traveling mode on the connectivity boundary Γ to find b_p $(p = 1, 2, 3, \ldots N)$

(e) Calculate the q'th column of the scattering matrix as $S_{pq} = \frac{b_p}{a_q}$

(f) Repeat for all $q = 1, 2, 3, \ldots N$

It was observed that if the connectivity boundary is placed $\lambda/4$ from the termination, the coefficients of the outgoing evanescent modes were quite small ($< 10^{-2}$) and were not therefore included in the final caculation of the scattering pattern.

We note that the generalized scattering matrix has certain distinct properties:

- Its size is N x N, where N is the number of traveling modes (See Table 1).
- It is symmetric and unitary since all modes are defined to have unit power.
- It has so far been observed to be sparse since the incoming modes tend to couple more strongly to those outgoing modes having indices in the proximity of the incoming mode. As an example, we illustrate in Figure 2 the scattering matrix for a stub terminated inlet as a function of the mode index using the ordering given in Table 3. The shown results were generated via the theoretically exact mode-matching technique [7] and the characteristic sparseness of the scattering matrix has been observed for all terminations investigated so far.

Given the generalized scattering matrix of the termination, the evaluation of the scattered field from the structure is feasible. Since the incident field is known, the coefficients $\{a\}$

of the incoming modes are also known [8], therefore the coefficients $\{b\}$ of the outgoing modes can be readily evaluated by (1). In the context of the modal technique, all outgoing modes are tracked to the open end, where an aperture integration is performed to calculate the radiated field. Since Aperture Integration is based on the Physical Optics approximation, it is often necessary to correct the result by including the effect of the rim, i.e. by considering the contribution of the fringe-wave currents [9]. The total far field can be evaluated in closed form for rectangular or cylindrical inlet cross-sections [10]. Although there can be higher order scattering mechanisms involving diffraction of the outgoing modes from the mouth which scatter back into the inlet, since the rim effects have been observed to be rather small, these higher order mechanisms are not included in the analysis.

If the inlet is electrically very wide, one can employ high frequency techniques to model the propagation through the inlet body. The most commonly used techniques are the Shooting and Bouncing Ray method (SBR) [4], and the Generalized Ray Expansion (GRE) [5]. Neither of them is as accurate as the exact modal method, but they are much simpler from a computational point of view. Moreover, unlike the modal technique, they do not require that the geometry be of canonical shape.

In the context of the SBR method, the incident field on the open end is decomposed into a set of parallel ray tubes which are tracked into the cavity. When using the GRE method, the open end aperture is divided into a number of subapertures, and the incident field is decomposed into a set of rays emanating from each subaperture. Unlike the SBR, the rays are not necessarily parallel to each other, and GRE is thus capable of tracing non-planar wavefronts. Regardless of which method is used (SBR or GRE), as soon as the rays reach the connectivity boundary, the incoming field is transformed into a superposition of modes using (2) (it is assumed that modes can be defined in the vicinity of the connectivity boundary). The generalized scattering matrix is then computed via the FEM analysis and the amplitudes of the out-going modes are computed from (1). The scattered field can be evaluated by means of the Reciprocity Integral method [11] thus eliminating the need to track the rays back to the open end.

3.0 Finite Element Analysis

The traditional FEM analysis involves the solution of the time harmonic, weak form of the wave equation in a bounded volumetric region of space. Being a partial differential equation method, the FEM analysis leads to sparse matrices (with about 10 to 50 nonzero entries per row) and permits the modeling of complex inhomogeneous regions without a need for special care and considerations. For our problem at hand, the FEM analysis region is shown inFigure 1 and is seen to extend a bit beyond the connectivity boundary Γ to a mesh termination boundary Γ'. On Γ' it is necessary to enforce an absorbing boundary condition (ABC) or some other mesh termination scheme which ensures the outgoing nature of the waves. That is, Γ' must be a non-reflecting boundary and this will be discussed later in more detail. We remark that the cross section between Γ and Γ' is again assumed circular for this analysis but this assumption has no bearing on the actual cavity of Figure 1.

On the basis of the FEM-modal formulation, we are interested in computing the fields scattered by the cavity termination due to the modal excitation

$$\bar{E}^{inc} = \bar{\Psi}_q \tag{4}$$

The total field in the FEM region is then given by

$$\bar{E} = \bar{E}^{inc} + \bar{E}^{s} \tag{5}$$

and it is well known that the unknown scattered electric field satisfies the weak wave equation (see for example [1],[2] and [13])

$$\begin{aligned} &\int_{\Gamma'}\int \left(\frac{1}{\mu_r}\bar{T}\cdot\left[\hat{n}\times\left(\nabla\times\bar{E}^{s}\right)\right]\right) ds + \int_{\Omega}\int\int \left(\frac{1}{\mu_r}\left(\nabla\times\bar{E}^{s}\right)\left(\nabla\times\bar{T}\right) - k_0^2\varepsilon_r\bar{T}\cdot\bar{E}^{s}\right) dV = \\ &-\int_{\Gamma'}\int \left(\frac{1}{\mu_r}\bar{T}\cdot\left[\hat{n}\times\left(\nabla\times\bar{E}^{inc}\right)\right]\right) ds - \int_{\Omega}\int\int \left(\frac{1}{\mu_r}\left(\nabla\times\bar{E}^{inc}\right)\left(\nabla\times\bar{T}\right) - k_0^2\varepsilon_r\bar{T}\cdot\bar{E}^{inc}\right) dV \end{aligned} \tag{6}$$

where $\bar{T}$ is referred to as a testing function and must be at least square integrable. For Galerkin implementations, $\bar{T}$ is set equal to one of the expansion basis and for each basis, a system equation is constructed. However, before proceeding with the system construc-

tion, it is necessary to first introduce the magnetic field $\bar{H}^s = \frac{\nabla\times\bar{E}^s}{j\omega\mu_0\mu_r}$ and rewrite the above weak equation as

$$\iiint_{\Omega}\{\frac{1}{\mu_r}(\nabla\times\bar{E}^s\cdot\nabla\times\bar{T}) - \bar{T}\cdot k_0^2\varepsilon_r\bar{E}^s\}\,dv - \iint_{\Gamma'}\{jk_0\eta\bar{T}\cdot(\hat{n}\times\bar{H}^s)\}\,ds +$$
$$\iiint_{\Omega}\{\frac{1}{\mu_r}(\nabla\cdot\bar{E}^s)\tau_1(\nabla\cdot\bar{T})\}\,dv = \iiint_{\Omega_d}\{\bar{T}\cdot\left(\nabla\times\frac{1}{\mu_r}\nabla\times\bar{E}^{inc} - k_0^2\varepsilon_r\bar{E}^{inc}\right)\}\,dv \quad (7)$$

in which Ω_d is the volume occupied by the dielectric not including the fictitious absorber (which will be discussed in the next section.) Also, the third term on the left hand side of (7) is the usual penalty term which ensures that the divergence condition be satisfied in the Galerkin least squares sense and is discussed in the next section.

On our way to discretizing the weighted residual equation given above, it is necessary to: (a) tessellate the volume Ω into smaller elements, (b) choose an expansion for the field in each element and (c) to relate $\bar{H}^s$ and $\bar{E}^s$ on the outer boundary of Ω including Γ'. These issues are addressed in the next section.

4.0 Implementation of the FEM Solution

Since the focus of the paper is to present the hybrid FEM-modal analysis, only those aspects of the implementation that are unique to this application will be discussed.

Although both edge-based and node-based elements were investigated, node-based elements were used in the final implementation because it was found that edge elements [13] broke down when the field was purely TE (no z component of the scattered electric field) for large problems. This breakdown was highly mesh dependent and was manifested in the form of a poorly conditioned global system. Clearly, if a vector field at the center of an element edge is orthogonal to that edge, as may occur in the case of purely TE fields, edge-based elements cannot represent that field. When a large volume (100,000 elements or more) is filled with a free tetrahedral mesh and the solution is purely TE, a nearly singular system may result. Thus, although edge elements are attractive for imposing the

boundary conditions on metallic surfaces and corners, we nevertheless resorted to node elements because of this breakdown.

It is well known that node based elements can have difficulties when applied to electromagnetic problems. The source of these problems has been reported from different points of view [12][14] [15][16] and remedies have been proposed. Among them, the penalty-term method has been widely used but a recent formulation using potentials rather than fields [15] appears promising. However, difficulties again appear with the imposition of boundary conditions on the potentials when dealing with disjointed structures. Since the engine face is a large target with many disconnected components we resorted to the traditional node-based formulation where the penalty term [16] was used for enforcing the divergenceless condition in a least square sense.

Although not rigorous, the traditional node-based implementation [16] gave good results provided care was exercised when enforcing the boundary conditions at metallic boundaries and edges.For a node lying on a conductor, the boundary conditions are

$$\begin{aligned} \hat{t}_1 \cdot \bar{E}^s &= -\hat{t}_1 \cdot \bar{E}^{inc} \\ \hat{t}_2 \cdot \bar{E}^s &= -\hat{t}_2 \cdot \bar{E}^{inc} \end{aligned} \tag{8}$$

where $\hat{t}_{1,2}$ denote the orthonormal unit vectors tangent to the metallic surface. There are many possible ways of coupling the global equations to enforce the boundary conditions (8), but there is always a best way which preserves the system's condition. If the boundary conditions are enforced arbitrarily, it is then possible to completely destroy the condition of the system and to generate wrong results. The following procedure will guarantee a well conditioned final system:

Given the metal surface normal $\hat{n}$ at the node, find the two tangent vectors $\hat{t}_1$ and $\hat{t}_2$ as follows

- if $|\hat{y} \times \hat{n}| > 0.15$ then set $\hat{t}_1 = \dfrac{\hat{y} \times \hat{n}}{|\hat{y} \times \hat{n}|}$

else set $\hat{t}_1 = \dfrac{\hat{x} \times \hat{n}}{|\hat{x} \times \hat{n}|}$

- $\hat{t}_2 = \dfrac{\hat{t}_1 \times \hat{n}}{|\hat{t}_1 \times \hat{n}|}$

• Given the three global equations for E_x^a, E_y^a and E_z^a at the node

- find the largest component of $\hat{t}_1$ (x, y or z) and replace the corresponding global equation with $\hat{t}_1 \cdot \bar{E}^s = -\hat{t}_1 \cdot \bar{E}^{inc}$

- find the largest component of $\hat{t}_2$ (x, y or z) and replace the corresponding global equation with $\hat{t}_2 \cdot \bar{E}^s = -\hat{t}_2 \cdot \bar{E}^{inc}$

At the open end of the mesh, the fields radiate into an infinite, cylindrical waveguide. The boundary condition at this open end must absorb all traveling modes in the guide (see Figure 1) and the most obvious choice for terminating the FEM mesh is to expand the scattered field as a sum of alltraveling modes and couple this expansion directly to the FEM equations. While this scheme worked well for shorted inlets, it was found to be unstable for the stub terminated inlet. Even if it were not for this instability, the full submatrix resulting from this scheme would make it impractical for large radius cavities. The full submatrix has a size of $M \times N_\Gamma$ where M is the number of modes in the cavity (including some evanescent modes) and N_Γ is the number of degrees of freedom on the connectivity boundary Γ. Both M and N_Γ increase as (approximately) the square of the radius of the guide. A more efficient scheme is to use a fictitious material absorber designed especially for cylindrical, traveling modes. The use of material absorbers in FEM computation also preserves the sparsity of the overall system and results in a better conditioned system than other mesh termination schemes such as numerical absorbing boundary conditions.

The design of a fictitious material absorber to absorb all traveling modes is complicated because the impedance and propagation constants of these modes vary greatly. The impedance of the first eight traveling modes for a guide of radius 0.66λ is given in Table 2. These eight modes were used to design an optimized absorber. Clearly, if the absorber was allowed to be very long, it could then be designed to have nearly perfect absorption. However, since the absorber will be part of the FEM mesh, as a design constraint it should be no more than about a half of a free space wavelength long to be practical.

A Monte Carlo optimization scheme based on [17] was used that has the desirable property of finding not only the best performing but also the most stable design. A five section, metal backed absorber was used as a starting point with ε_r and μ_r are set to unity in each

section. The length of each section was set initially to $.1\lambda$. The 15 parameters (material constants and lengths of each section) were varied randomly, independent of one another. Transmission line theory was used to calculate the reflection coefficient for each mode (see Figure 3), and the algebraic sum of reflection coefficients (the sum of absolute values) was used as the global optimization parameter. A pass/fail criterion on the global parameter was set to give about a 50% yield. For each random design, a pass or fail was noted for each parameter and after a number of designs have been sampled, a pattern begins to emerge. Some parameters indicate a tightening up is in order since most of the 'good' designs were centered about a certain value. Other parameters indicate a don't care condition as all values worked equally well. A new set of initial values and ranges is chosen and the process is restarted. Again, the global parameter threshold is chosen to give about a 50% yield. This global threshold continues to drop each iteration until a stable design is found.

The final design and its performance is shown in Figure 4. Note that the reflection coefficient for all modes is less than .1 (-10 dB). The performance of this absorber was tested for a larger guide of radius 2λ having 77 traveling modes and from Figure 5 it is seen to have good broad-band performance.

There are many advantages to using the optimized fictitious absorber for terminating the mesh. First, the condition of the FEM system is actually improved through the use of this type of truncation scheme. While a local or global ABC would require a smaller mesh, this savings becomes less important as the problem size increases since the absorber will take up a smaller fraction of the total volume.

5.0 Examples

Example 1

The simplest configuration that could be analyzed is a cylindrical cavity terminated with a flat plate. To terminate the FEM mesh the absorber was placed 0.33λ away from the cavity base. We remark that no mode coupling is present in this configuration and that the mesh was generated using SDRC I-DEAS with a global element size of $\frac{1}{12}\lambda$. For this calculation, the connectivity boundary was placed 0.15λ from the base and the scattering matrix calculated using the FEM-modal formulation was used to calculate the outgoing

mode coefficients. These modes were then traced back out of the inlet to find the radiated field. The results are shown in Figure 6 for a 1λ long and 1.32λ wide cylindrical cavity. Good agreement is seen as compared to a mode matching solution [7]. We note that the penalty parameter τ_1 in (7) was simply set to unity for this example.

Example 2

The next simplest cavity termination is a circular stub. This geometry also can be analyzed via a mode matching solution [7] since all of the conductors are on curves of constant coordinates. The absorber was placed 0.33λ from the stub and the scattering matrix was computed at a distance of 0.25λ in front of the stub. The co-polarized backscatter patterns are given in Figure 7.

It was found that the proper handling of the boundary conditions at the inner edge (the rim of the stub) was critical. If the total field were set to zero at this inner edge, the results were not as good. However, if only the component tangential to the edge (E_ϕ) was set to zero, whereas $\bar{E}_z$ was allowed to float, the results were much improved as is depicted in Figure 7.

While the shown results are in good agreement for horizontal polarization, there is some discrepancy in the vertical polarization. Finer sampling around the rim does improve the comparison slightly but with very slow convergence. The result shown were obtained using a global element size of $\frac{1}{12}\lambda$ and an element size of $\frac{1}{20}\lambda$ around the rim. Again, the penalty term was set to unity.

Example 3

The third example is for an inlet with a ridge termination as shown in Figure 8. The termination consists of four ridges (grooves) each with an angular span of 45 degrees. The absorber was placed 0.5λ from the ridge interface and the scattering matrix was evaluated at a distance of 0.25λ from the discontinuity.

For this problem, it was found that the implementation of the penalty term had modest effects on the results. The penalty term contains an arbitrary parameter τ_1 which in the previous examples was set to unity. However, by using an analytical solution as a reference, or by fitting the formulation to a higher order scheme, it is possible to find an expres-

sion for τ_1 as a function of the element size and local material parameters that minimizes the net error in the FEM solution. This type of approach has been used with success in the field of applied mechanics [18],[19]. For this example we have set

$$\tau_1 = 842.1 \frac{V^{(\frac{2}{3})}}{2} \tag{9}$$

where V is the volume of the element and this value of τ_1 was determined numerically by minimizing the error for the shorted inlet of the same radius. It is noted that for a global mesh size of about $\frac{1}{12}\lambda$ the value of τ_1 is unity. Additional implementation considerations for the penalty term have been made but are beyond the scope of this paper.

Again, boundary conditions at the internal edges and corners needed to be handled properly in order to achieve physically meaningful results. From example 2 it was found that only the tangential field to the edges should be specified at the internal edges while the other components remained as degrees of freedom. For this example, the additional complexity of the ridge geometry gives rise to corners as well, and it was found that the boundary conditions at these corners could modestly affect the scattering patterns. The boundary conditions imposed at the corners must of course be consistent with the known field behavior and discontinuities. With this in mind, the total field components at the corners formed by the ridges and the outer cylindrical guide were all set to zero. At the inner corners, where the ridge meets the inner cylinder, the geometry is discontinuous in the z direction only and thus the z directed electric field was a degree of freedom while the other components of the total field were set to zero.

Figure 8 shows the principle plane, co-polarized RCS patterns computed via the modal-FEM scheme and a mode matching solution [7]. It is seen that the RCS patterns compare well with the mode matching solution especially around normal incidence. For this example a global mesh size of $\frac{1}{13}\lambda$ was used with a local mesh size of $\frac{1}{26}\lambda$ around the discontinuities. It is suspected that the errors in the modal-FEM results are due to the simplistic penalty term and not due to the material absorber (based on the good results achieved for the shorted inlet.) It is of course, also possible that there are errors in the mode matching result due to the necessary truncation of the infinite series.

6.0 Conclusions

The benchmark tests show the validity of the overall FEM-modal scheme and the utility of the broadband cylindrical mode absorber for terminating the mesh. Also, the results indicate that node-based elements can be used for scattering analysis if boundary conditions are handled properly so as not to disturb the condition of the FEM system. Additional consideration must however be given to the proper implementation of the penalty term by fitting the numerical scheme to known, analytical solutions and selecting a penalty function to minimize the net error. Since the edge elements broke down for the pure TE case, no comparison between edge and node-based elements was possible for this problem.

Several different methods and schemes tried before the above formulation was settled on. A mode matching technique for terminating the mesh was tried but was found to be unstable in addition to its large storage requirements. A mathematical absorbing boundary condition was considered, but have been found to produce poorly conditioned systems in comparison to fictitious material absorbers. Thus, we resorted to a specially designed material absorber for terminating the mesh and this was shown to have good modal absorption for inlets larger than was initially considered.

The validation of the method for non-trivial cavity terminations and the proper implementation of the boundary conditions near edges and discontinuities were indeed challenging tasks. With regards to the validation, a mode-matching code was written which was crucial to the validation of the modal-FEM formulation since it is difficult to isolate the termination scattering by measurement techniques. As seen, the comparison between the results from the two methods were quite good given the geometric complexity and diversity of the solution procedures.

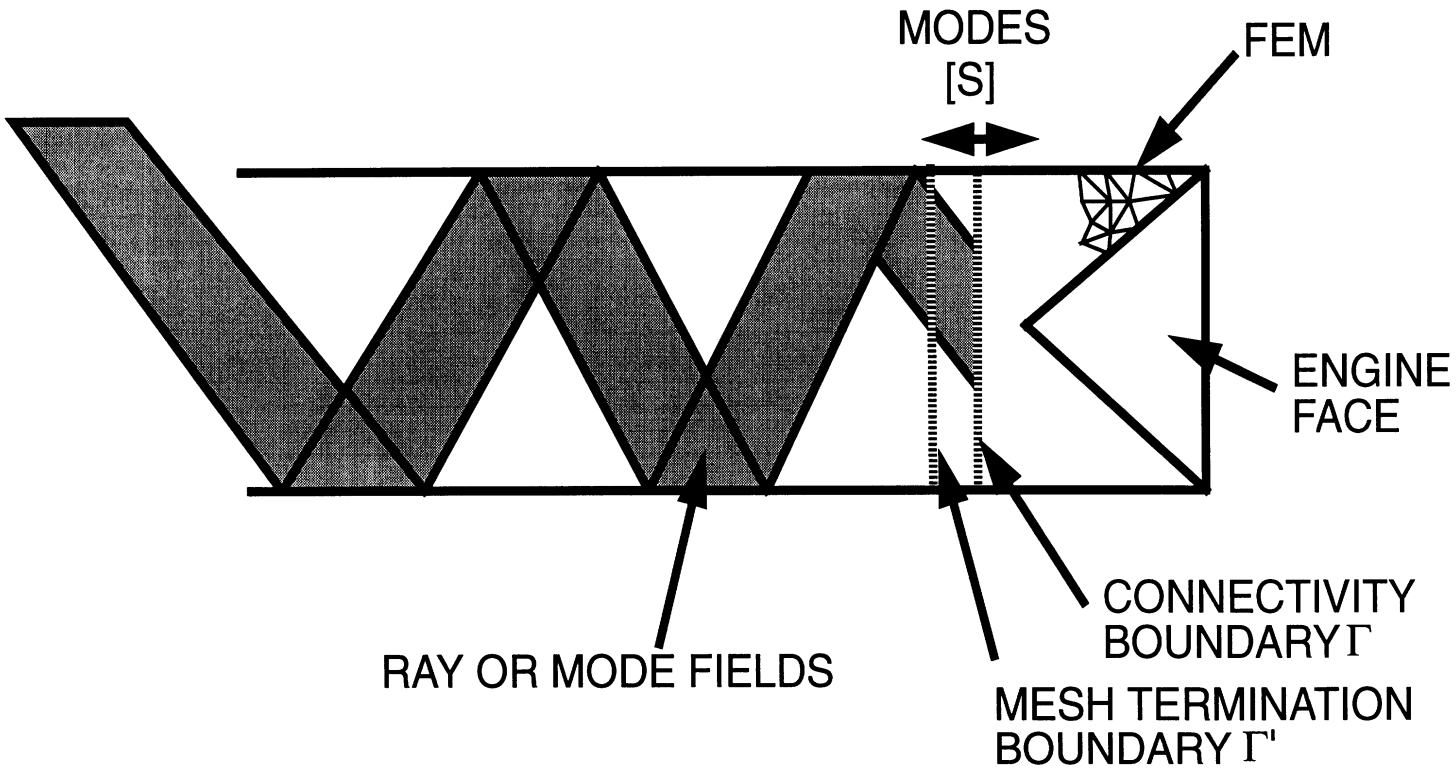

FIGURE 1. Hybrid jet engine inlet analysis.

radius (λ)	.5	.66	1.66	3	4	5	10
N	6	10	60	186	328	508	2008

TABLE 1. Number of traveling modes for different radii cylindrical guides.

Mode	TM^e_0	TM^e_1	TE^o_1	TE^o_2	TM^o_1	TE^e_0	TE^e_1	TE^e_2
Z (Ω)	307	144	421	557	144	986	421	557

TABLE 2. Impedance of the eight different traveling modes in a cylindrical guide with radius 0.66λ.

m	Mode
1-10	$TM^e_{0,1}$ - $TM^e_{0,10}$
11-20	$TM^e_{1,1}$ - $TM^e_{1,10}$
21-30	$TM^e_{2,1}$ - $TM^e_{2,10}$
31-40	$TE^o_{0,1}$ - $TE^o_{0,10}$
41-50	$TE^o_{1,1}$ - $TE^o_{1,10}$
51-60	$TE^o_{2,1}$ - $TE^o_{2,10}$

TABLE 3. Mode indices corresponding to the results in Figure 2

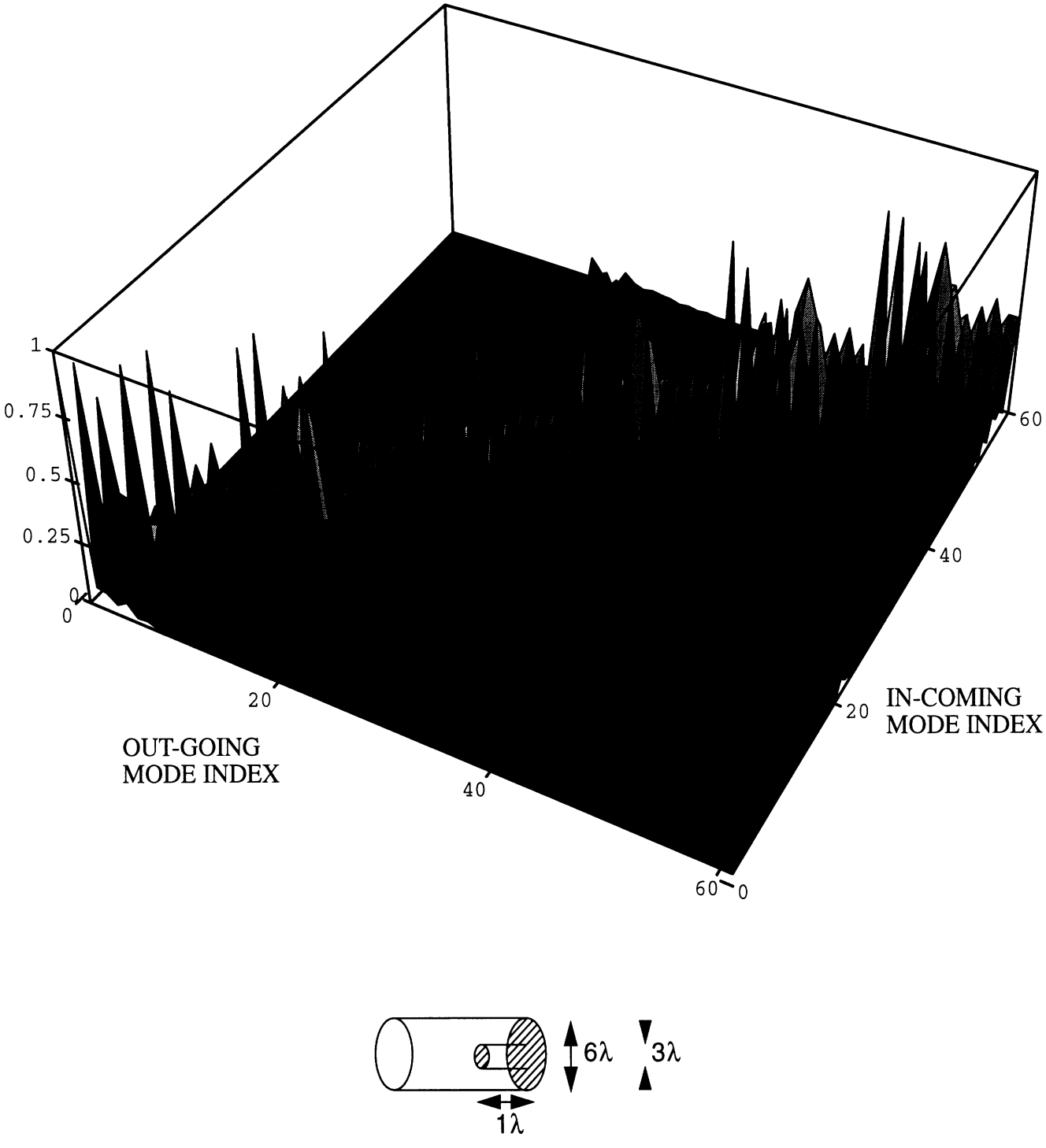

FIGURE 2. Amplitudes of the elements of the generalized scattering matrix calculated by mode-matching for a hub termination.

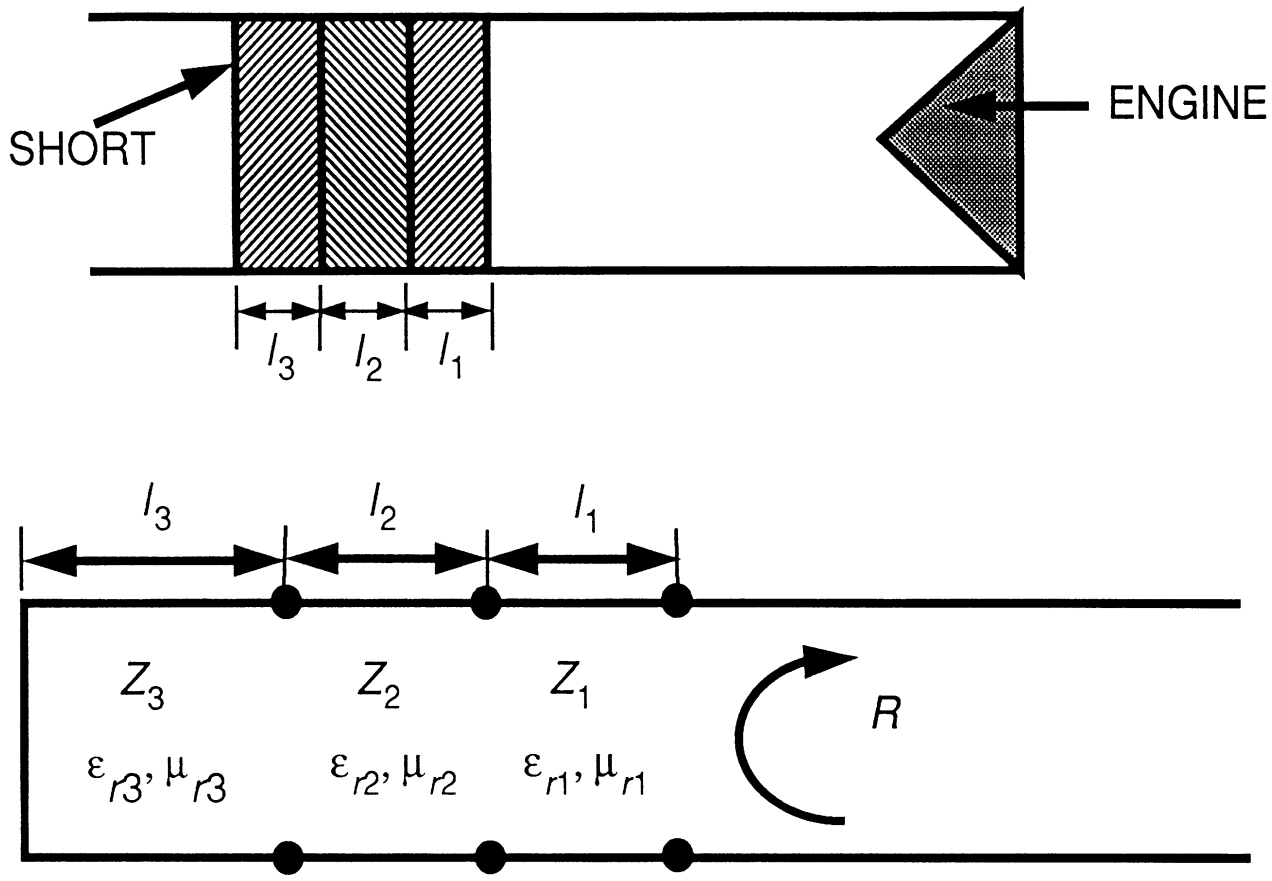

$$Z_i^{TE} = \frac{Z_i k_i}{k_{zi}} \qquad Z_i^{TM} = \frac{Z_i k_{zi}}{k_i}$$

$$Z_i = Z_0 \sqrt{\frac{\mu_{ri}}{\varepsilon_{ri}}} \qquad k_i = k_0 \sqrt{\varepsilon_{ri} \mu_{ri}}$$

FIGURE 3. Transmission line model of cylindrical waveguide absorber.

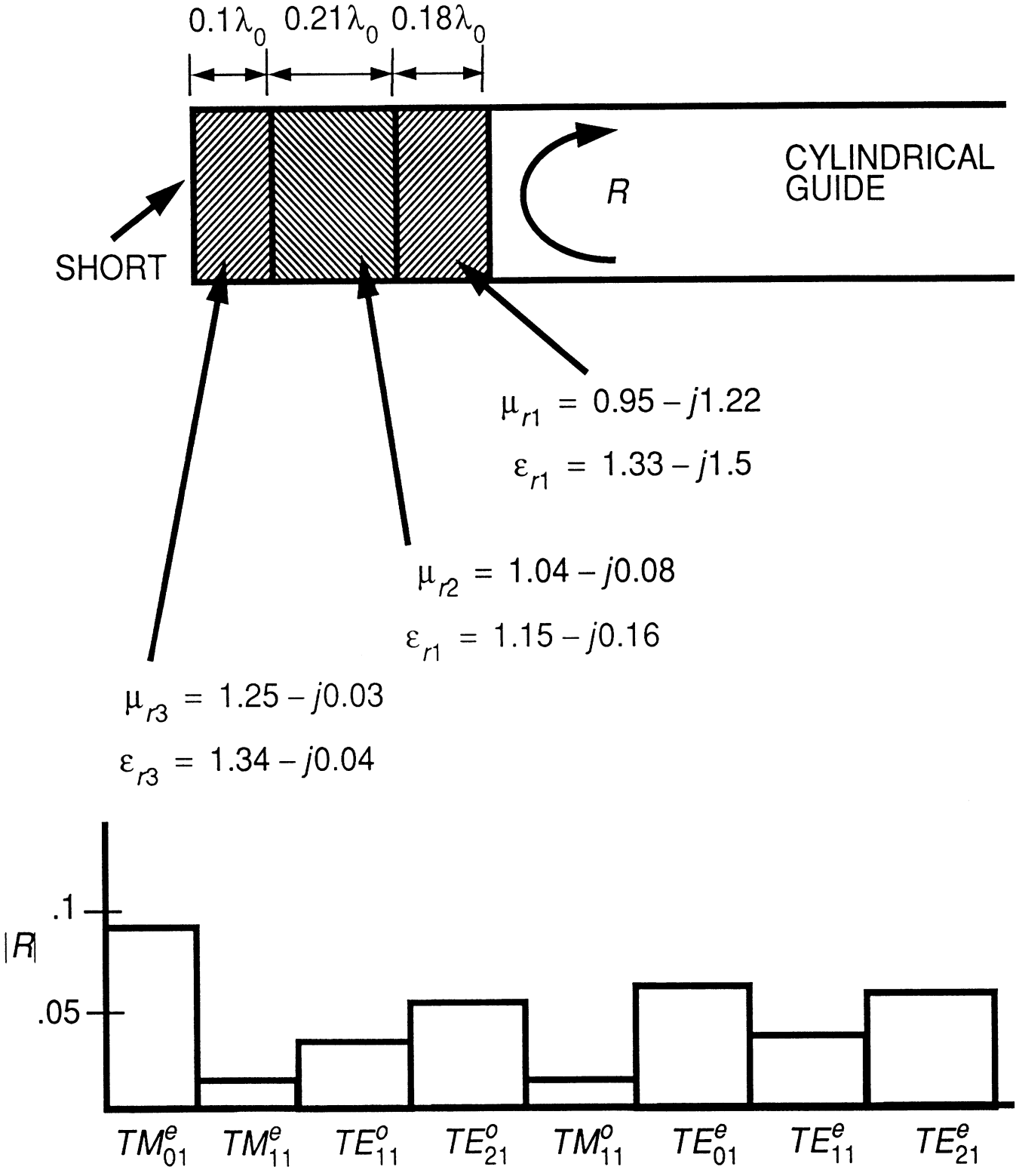

Modal Reflection Coefficients from Optimum Absorber

FIGURE 4. Optimum cylindrical waveguide absorber.

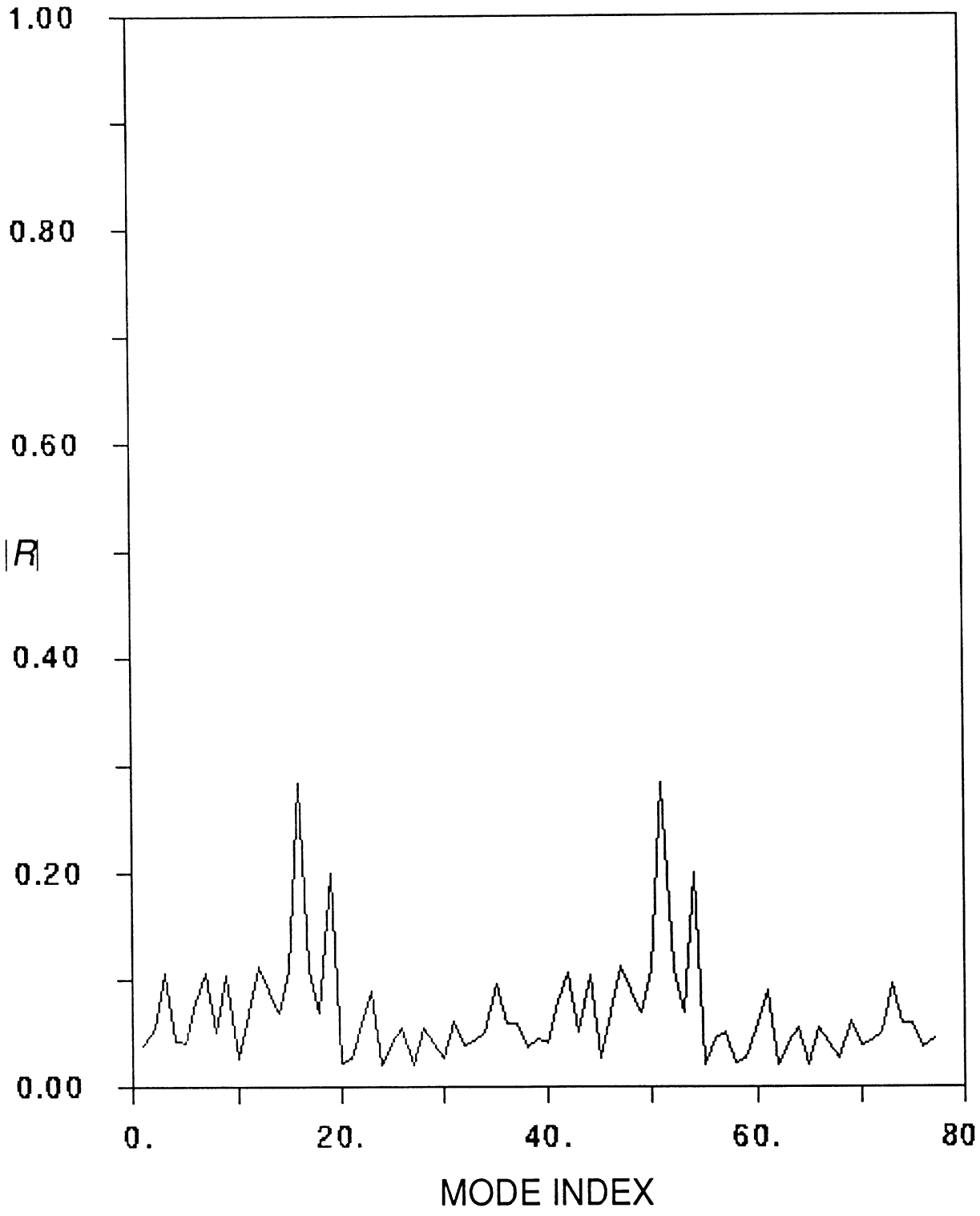

FIGURE 5. Performance of optimum absorber for the 77 traveling modes in a guide of radius 2λ.

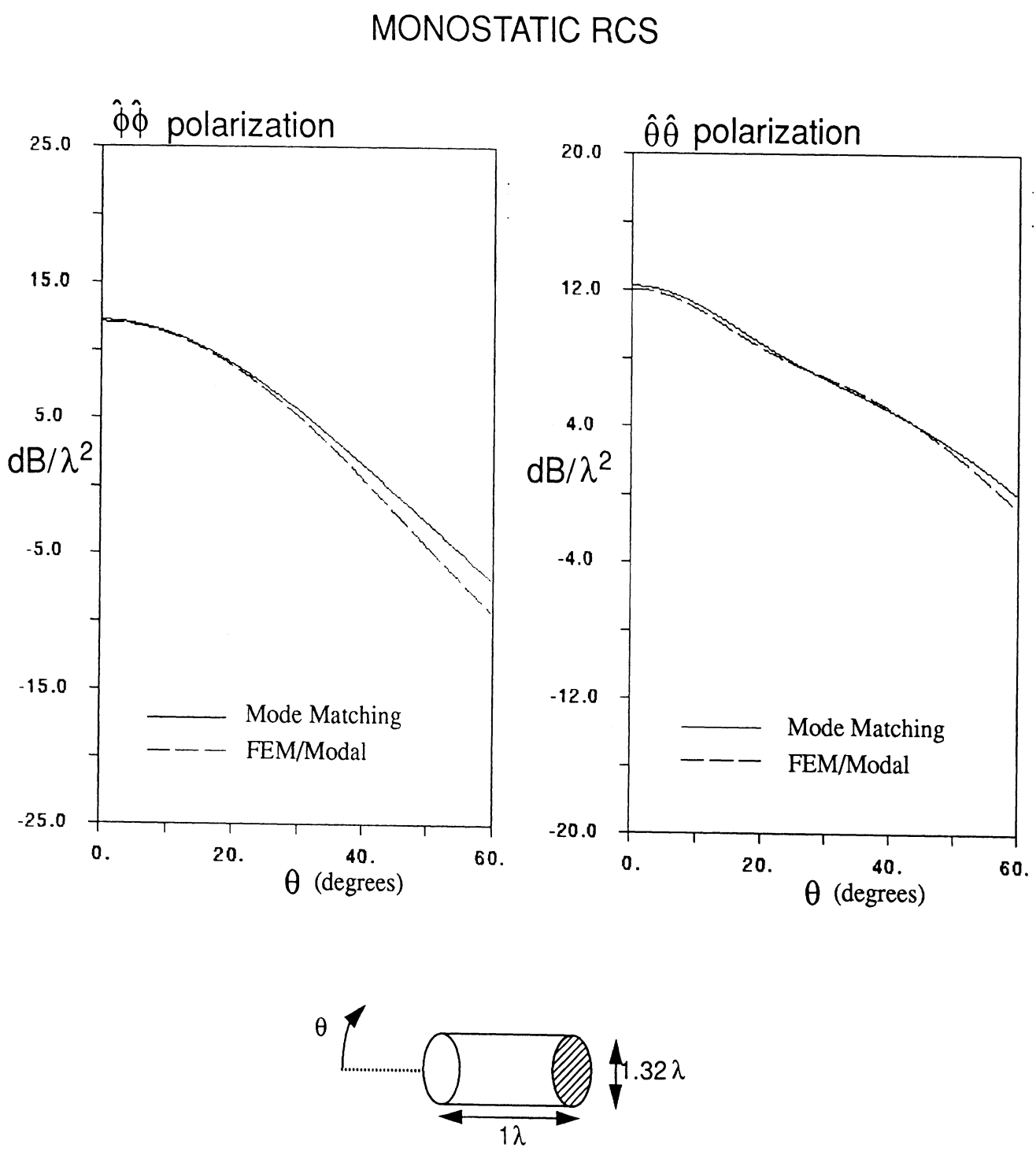

FIGURE 6. Results for example 1: a shorted cylindrical cavity.

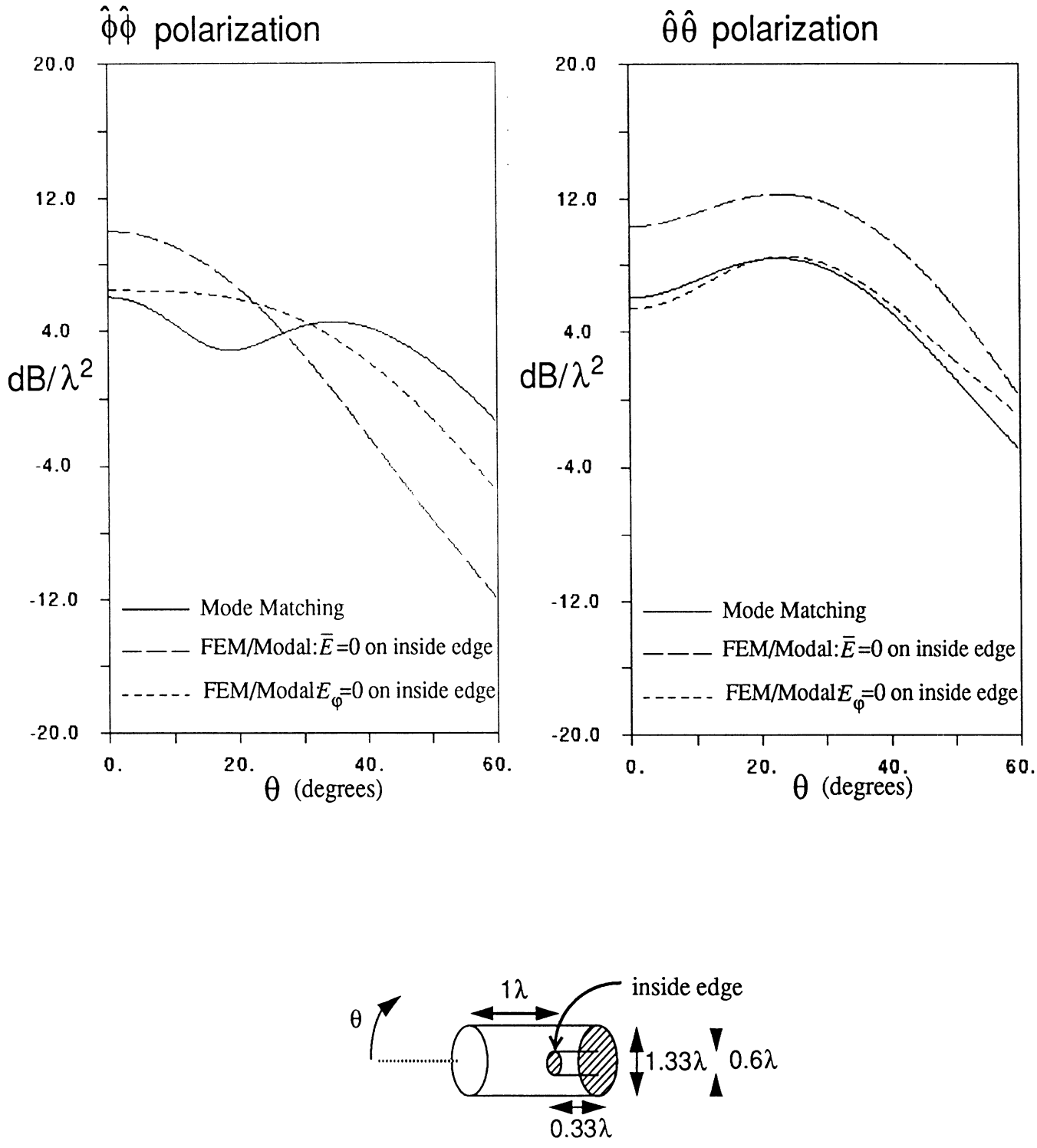

FIGURE 7. Results for example 2. A stub terminated inlet.

MONOSTATIC RCS

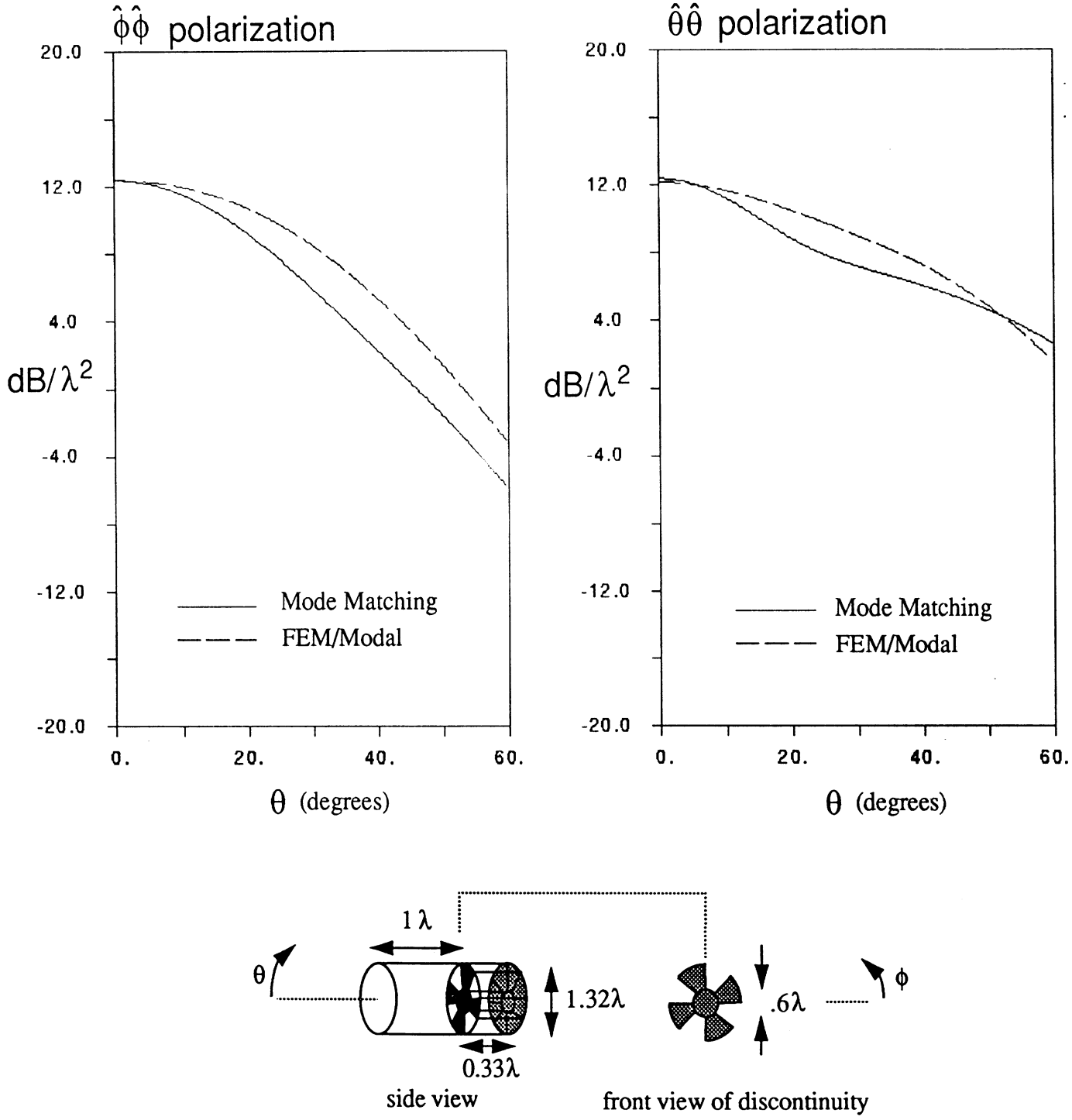

FIGURE 8. Example 3: A ridged terminated structure

References

[1]P. P. Silvester and R. L. Ferrari, *Finite Elements for Electrical Engineers*, Cambridge, 1986.

[2]J. L. Volakis, A. Chatterjee and L. C. Kempel, "A review of the finite element method for three-dimensional electromagnetic scattering." *J. Opt. Soc. Amer.-A, pp. 1422-1433, April 1994.*

[3]D. C. Ross, J. L. Volakis and T. Ozdemir, "A New Finite Element Formulation for Modeling Circular Inlets with Irregular Terminations", Technical Report 030395-1-T, The University of Michigan, EECS Radiation Laboratory, Ann Arbor MI, May 1993.

[4]H. Ling, R. Chou and S. W. Lee, "Shooting and Bouncing Rays: Calculating the RCS of an Arbitrary Shaped Cavity", *IEEE Transactions on Antennas and Propagation,* vol. AP-37, no. 2, pp. 194-205, Feb. 1989.

[5]P. H. Pathak and R. J. Burkholder, "High Frequency EM Scattering by Open-Ended Waveguide Cavities", *Radio Science*, vol. 26, no. 1, pp. 211-218, Jan.-Feb. 1991.

[6]A. Altintas, P. H. Pathak and M. C. Liang, "A Selective Modal Scheme for the Analysis of EM Coupling into or Radiation from Large Open-ended Waveguides", *IEEE Transactions on Antennas and Propagation,* vol. AP-36, no. 1, pp. 84-96, Jan. 1988.

[7]H. T. Anastassiu and J. L. Volakis, "The Mode Matching Technique for Electromagnetic Scattering by Inlets with Complex Terminations", Technical Report 030395-3-T, The University of Michigan, EECS Radiation Laboratory, Ann Arbor MI, October 1993.

[8]Ching-Chao Huang, "Ray Analysis of EM Backscatter from a Cavity Configuration", Ph.D. Dissertation, The Ohio State University, ElectroScience Laboratory, Columbus OH, 1982.

[9]P. Ya. Ufimtsef, "Method of Edge Waves in the Physical Theory of Diffraction" (in Russian) *Izd-Vo Sov. Radio,* pp. 1-243, 1962. (English Translation, U.S. Foreign Techn. Office Div., Doc. ID FTD-HC-23-259-71, Wright-Patterson AFB, Dayton OH, 1971).

[10]P. H. Pathak, C. W. Chuang, M. C. Liang, "Inlet Modeling Studies", Technical Report 717674-1, The Ohio State University, ElectroScience Laboratory, Columbus OH, October 1980.

[11]P. H. Pathak and R. J. Burkholder, "A Reciprocity Formulation for the EM Scattering by an Obstacle Within a Large Open Cavity", *IEEE Transactions on Microwave Theory and Techniques*, vol. MTT-41, no. 4, pp. 702-707, Apr. 1993.

[12]D.R. Lynch and K.D. Paulsen, "Origin of vector parasites in numerical Maxwell solutions," *IEEE Transactions on Microwave Theory and Techniques*, vol. MTT-39, no. 3, pp. 383-394, Mar. 1991.

[13]M. L. Barton and Z. J. Cendes, "New vector finite elements for three-dimensional magnetic field computation", *J. Appl. Phys.*, vol. 61, no. 8, pp. 3919-3921, Apr. 1987.

[14]Werner Schroder and Ingo Wolff, "The Origin of Spurious Modes in Numerical Solutions of Electromagnetic Field Eigenvalue Problems", *IEEE Transactions on Microwave Theory and Techniques*, vol. MTT-42, no. 4, pp. 644-653, Mar. 1994

[15]Keith D. Paulsen, William E. Boyse and Daniel R. Lynch, "Continuous Potential Maxwell Solutions on Nodal-Based Finite Elements", *IEEE Transactions on Antennas and Propagation,* vol. AP-40, no. 10, pp. 1192-1200, Oct. 1992.

[16]B. M. Azizur Rahman and J. B. Davies, "Penalty Function Improvement of Waveguide Solutions by Finite Elements", *EEE Trans. Microwave Theory Tech.*, vol. 32, no. 8, pp 922-928, Aug. 1984.

[17]A. B. MacFarland, "Parameter Centering and Tolerancing", Master's Thesis, Electrical Engineering Graduate School, Univ. of Idaho, Aug. 86.

[18]F. Brezzi, M. Bristeau, L. P. franca, M. Mallet, G. Roge, "A relationship between stabilized finite element methods and the Galerkin method with bubble functions", *Computer Methods in Applied Mechanics and Engineering*, vol 96, pp 117-129, 1992.

[19]R. Pierre, "Simple C^0 approximations for the computation of incompressible flows", *Computer Methods in Applied Mechanics and Engineering*, vol 68, pp 205-227, 1988.

The Mode Matching Technique for Electromagnetic Scattering by Cylindrical Waveguides with Canonical Terminations.

Hristos T. Anastassiu, John L. Volakis and Daniel C. Ross

Radiation Laboratory
Department of Electrical Engineering and Computer Science
University of Michigan
Ann Arbor MI 48109-2122

December 1994

Abstract

The Mode Matching Technique is employed for the evaluation of the Radar Cross-Section (RCS) of cylindrical inlets terminated by a perfectly conducting cylindrical hub or a cylindrical array of grooves that may be straight or curved. In the case of curved grooves, the geometry is analyzed via the generalized transmission line theory and a closed form solution is given for the first time. The method is formally exact, and yields accurate RCS patterns for geometries that have not been previously investigated. Analytical expressions are derived for the coupling factors between the various modes and RCS results are presented which may be used as a reference in validating other, more general numerical techniques.

1 Introduction

The problem of scattering by open ended cavities is important in scattering analysis because jet engine inlets are significant contributors to the radar cross-section (RCS) of aircraft configurations. Indeed, numerous studies have been published on the analysis of propagation through ducts of rectangular and cylindrical cross-sections. Among them, Johnson and Moffat [1] presented a rigorous Wiener-Hopf analysis for the circular straight duct terminated by a short, and Ching-Chao Huang [2] considered a GTD/modal analysis of circular ducts terminated by a simple blade configuration. In the case of large size, arbitrary cross-section ducts, high frequency methods have been introduced. Among them, the Shooting and Bouncing Ray (SBR) method [3] has been succesfully employed to track the ray fields within the duct. The SBR decomposes the aperture fields into a set of parallel rays which are then tracked into the duct in accordance with Geometrical Optics (GO) laws. An important advantage of the SBR is its simplicity and ease of interfacing with solid modeling packages [4]. However, although the SBR is attractive for general-purpose calculations, it lacks accuracy because it neglects rim diffraction and fails at caustics. Some of the disadvantages of the SBR method can be overcome by subdividing the aperture into smaller subapertures, and this is the basic concept of the Generalized Ray Expansion (GRE) method [5]. Unlike the SBR, the rays are not necessarily parallel to each other, and consequently the GRE is capable of tracing non-planar wavefronts.

Although the above ray methods have been quite successful in modeling the field propagation through large cross section ducts, they are not suited for characterizing ray reflections from complex jet engine terminations which have irregular boundaries and edges. With this in mind, our motivation in this report is to present methods for the characterization of irregular engine-like terminations placed at the back end of the duct. Specifically, the Mode Matching (MM) precedure is applied to three different cavity terminations. The simplest of these is the cylindrical hub termination illustrated in Fig. 1. Its analysis is presented first with the intent of illustrating the MM procedure for this application. The technique is then applied to a termination consisting of an array of grooves as illustrated in Fig. 2. This termination geometry is, of course, much more complex than the hub, but nevertheless the MM analysis parallels that of the hub.

The most significant contribution of the report is the analysis of a termination consisting of an array of curved blades (see Fig. 3). Again, the MM procedure is applied, but the challenge in this case is the expansion of the fields propagating within the array of grooves. It is demonstrated in section 4 that the fields between a pair of curved blades can be expressed in analytical form, provided the blades are curved in a specific manner.

We note that this report is not concerned with the characterization of the fields within the duct. These can be successfully described by the SBR and GRE methods. Consequently, throughout the report the duct is assumed to be straight, with circular cross-section.

2 Cylindrical Hub Termination

2.1 Mode Matching Formulation

In this section we apply the MM technique to the geometry of Fig. 1. We assume that a plane wave is incident on the open end of the cylindrical duct and we are interested in evaluating the scattered field as a function of the incidence angle. In accordance with the MM technique, the fields in regions 1 and 2 are first expressed as a weighted sum of waveguide modes propagating either along the positive or negative z direction. Of course, the coefficients of the expansion are then determined by enforcing tangential field continuity across the interface separating regions 1 and 2. Before the application of the method it is necessary to evaluate the coupling of the incident plane wave with the forward propagating modes of region 1.

The geometries of regions 1 and 2 are separable, and therefore Helmholtz's equation can be solved analytically to yield the appropriate mode representations in each region [6]. These representations are given explicitly in Appendix I. As in Appendix I, the transverse fields of each mode are denoted by $\mathbf{e}_{i,n}$, $\mathbf{h}_{i,n}$, where $\mathbf{e}$ stands for the electric field, and likewise $\mathbf{h}$ stands for the magnetic field. The subscript i may be either 1 or 2, corresponding to regions 1 and 2 respectively, and n is the characteristic integer of the mode. In region 1 the modes can be TM or TE, whereas in region 2 they are TM, TE or TEM.

Using the mode functions given in Appendix I, the transverse components of the incident field are represented as a superposition of modes propagating

along the $-z$ direction, viz.

$$\mathbf{E}_1^{ti} = \sum_{n=1}^{\infty} a_n \mathbf{e}_{1,n} \exp\{j\beta_{1,n} z\} \tag{1}$$

$$\mathbf{H}_1^{ti} = \sum_{n=1}^{\infty} a_n \mathbf{h}_{1,n} \exp\{j\beta_{1,n} z\} \tag{2}$$

with the a_n coefficients given by [2]

$$a_n = \frac{\pi r e^{jkr}}{j\omega\mu} \mathbf{E}_{inc} \cdot \mathbf{E}_{rad,n}(\mathbf{r}) \tag{3}$$

$\mathbf{E}_{inc}$ denotes the incident plane wave at the center of the open end before it couples into the cylinder and $\mathbf{E}_{rad,n}$ is the radiated field of the n^{th} outgoing mode of unit power impinging at the inlet mouth from the interior of the waveguide. Also, in (3) $\mathbf{r}$ is the spherical far zone distance from the center of the open end of the cavity. The transverse fields reflected at the interface take similar forms, namely

$$\mathbf{E}_1^{tr} = \sum_{n=1}^{\infty} b_n \mathbf{e}_{1,n} \exp\{-j\beta_{1,n} z\} \tag{4}$$

$$\mathbf{H}_1^{tr} = -\sum_{n=1}^{\infty} b_n \mathbf{h}_{1,n} \exp\{-j\beta_{1,n} z\} \tag{5}$$

where b_n are unknown coefficients to be determined. The transverse fields in region 2 can be expressed as

$$\begin{aligned} \mathbf{E}_2^t &= \sum_{m=1}^{\infty} c_m \mathbf{e}_{2,m} \exp\{j\beta_{2,m} z\} + \\ &+ \sum_{m=1}^{\infty} d_m \mathbf{e}_{2,m} \exp\{-j\beta_{2,m} z\} \end{aligned} \tag{6}$$

$$\begin{aligned} \mathbf{H}_2^t &= \sum_{m=1}^{\infty} c_m \mathbf{h}_{2,m} \exp\{j\beta_{2,m} z\} - \\ &- \sum_{m=1}^{\infty} d_m \mathbf{h}_{2,m} \exp\{-j\beta_{2,m} z\} \end{aligned} \tag{7}$$

The latter are sums of $+z$ and $-z$ propagating modes, where the coefficients c_m, d_m, b_m must be determined by enforcing continuity of the tangential fields at the interface ($z = 0$) and the required boundary condition at the back of the guide ($z = -l_2$). Mathematically, field continuity at $z = 0$ implies

$$\mathbf{E}_1^{ti}|_{z=0} + \mathbf{E}_1^{tr}|_{z=0} = \mathbf{E}_2^{t}|_{z=0} \tag{8}$$

$$\mathbf{H}_1^{ti}|_{z=0} + \mathbf{H}_1^{tr}|_{z=0} = \mathbf{H}_2^{t}|_{z=0} \tag{9}$$

$$\forall \rho \in [a, b], \forall \phi \in [0, 2\pi]$$

and

$$\mathbf{E}_1^{ti}|_{z=0} + \mathbf{E}_1^{tr}|_{z=0} = \mathbf{0} \tag{10}$$

$$\forall \rho \in [0, a], \forall \phi \in [0, 2\pi]$$

To facilitate the analysis, we introduce the vectors

$$\{\mathbf{a}\} \equiv [a_1, ..., a_{M_1}]^T \tag{11}$$

$$\{\mathbf{b}\} \equiv [b_1, ..., b_{M_1}]^T \tag{12}$$

$$\{\mathbf{c}\} \equiv [c_1, ..., c_{M_2}]^T \tag{13}$$

$$\{\mathbf{d}\} \equiv [d_1, ..., d_{M_2}]^T \tag{14}$$

where M_i is the number of modes in the i^{th} region. Evidently, for an exact modal representation, $M_i \to \infty$.

Substituting (1), (4) and (6) into (8) and (10), taking the dot product of the resulting equations with $\mathbf{e}_{1,m}$, and then integrating over the cross-section of the interface yields

$$[\mathbf{U}](\{\mathbf{a}\} + \{\mathbf{b}\}) = [\mathbf{P}]^T(\{\mathbf{a}\} + \{\mathbf{b}\}) \tag{15}$$

where the superscript T denotes the transpose of the matrix. The elements of the square matrices [**P**] and [**U**] are given by

$$P_{mn} \equiv \int_a^b \int_0^{2\pi} \mathbf{e}_{2,m} \cdot \mathbf{e}_{1,n} \rho d\rho d\phi \tag{16}$$

$$U_{mn} \equiv \delta_{mn} \int_0^b \int_0^{2\pi} \mathbf{e}_{1,m} \cdot \mathbf{e}_{1,m} \rho d\rho d\phi \tag{17}$$

in which δ_{mn} is the Kronecker delta. Next, on substituting (2), (5) and (7) into (9), upon taking the dot product of (9) with $\mathbf{h}_{2,m}$ and integrating over the portion of the interface which excludes the perfectly conducting disk defined by $\rho \leq a$ yields

$$[\mathbf{R}]\left(\{\mathbf{a}\} - \{\mathbf{b}\}\right) = [\mathbf{V}]\left(\{\mathbf{a}\} - \{\mathbf{b}\}\right) \tag{18}$$

where

$$R_{mn} \equiv \int_a^b \int_0^{2\pi} \mathbf{h}_{2,m} \cdot \mathbf{h}_{1,n} \rho d\rho d\phi \tag{19}$$

$$V_{mn} \equiv \delta_{mn} \int_a^b \int_0^{2\pi} \mathbf{h}_{2,m} \cdot \mathbf{h}_{2,m} \rho d\rho d\phi \tag{20}$$

Finally, upon enforcing the boundary condition at the back end ($z = -l_2$) we obtain the system

$$[\mathbf{D}]^{-1}\{\mathbf{d}\} = [\mathbf{S}_{end}][\mathbf{D}]\{\mathbf{c}\} \tag{21}$$

where

$$D_{mn} \equiv \delta_{mn} \exp\{-j\beta_{2,m} l_2\} \tag{22}$$

and $[\mathbf{S}_{end}]$ denotes the scattering matrix at the back end of the termination.

It can be shown [7] that

$$[\mathbf{P}][\mathbf{U}]^{-1} = [\mathbf{V}]^{-1}[\mathbf{R}] \equiv [\mathbf{L}] \tag{23}$$

provided the modes in both regions are normalized to unity power according to (68) of Appendix I. Using this identity, it follows from (15), (18), (21) and (23) that

$$\{\mathbf{b}\} = \left([\mathbf{W}] + [\mathbf{I}]\right)^{-1}\left([\mathbf{W}] - [\mathbf{I}]\right)\{\mathbf{a}\} \equiv [\mathbf{S}]\{\mathbf{a}\} \tag{24}$$

where

$$[\mathbf{W}] = [\mathbf{L}]^T \Big([\mathbf{I}] + [\mathbf{D}][\mathbf{S}_{end}][\mathbf{D}] \Big) \Big([\mathbf{I}] - [\mathbf{D}][\mathbf{S}_{end}][\mathbf{D}] \Big)^{-1} [\mathbf{L}] \tag{25}$$

and $[\mathbf{I}]$ is the unit matrix. The matrix

$$[\mathbf{S}] = ([\mathbf{W}] + [\mathbf{I}])^{-1} ([\mathbf{W}] - [\mathbf{I}]) \tag{26}$$

is the generalized scattering matrix of the termination and is independent of the excitation. It is worth mentioning that the elements of $[\mathbf{L}]$ for this geometry can be evaluated in closed form (see [8] for the relevant analytical expressions).

It is evident from (24) that the infinite modal scattering matrix must be truncated for a numerical evaluation of the vector $\{\mathbf{b}\}$ and extreme care is necessary to achieve an appropriately convergent result. Mittra and Lee [10] discuss these difficulties, and point out that reliable convergence can be achieved by choosing an appropriate ratio M_1/M_2 of the number of modes used in the two regions. This ratio depends on the geometry, and it can be shown [11] that once the relative convergence problem is resolved by appropriately choosing the ratio M_1/M_2, good conditioning of the system is guaranteed.

Once $\{\mathbf{b}\}$ is determined, the far zone radiated fields from the open end are obtained by integrating the modal fields over the aperture (Kirchhoff approximation) and the appropriate expressions are given in Appendix II. Summing over all the modes, using the b_m coefficients as weights, yields the total scattered field of the structure.

2.2 Numerical Results

Figure 4 shows some numerical results for the geometry shown in Fig. 1. In generating the calculated data, 420 modes were used to represent the fields in each region, i.e. the order of the cylindrical functions ranged from $n = 0$ to $n = 14$ and 7 modes for each n were taken into account (i.e. we used $15 \cdot 7 = 105$ TM modes, plus 105 TE modes, multiplied by 2 for even and odd angular behavior. For region 2, the TEM mode substituted one of the less important evanescent TM modes). Clearly, the MM calculations are in good agreement with data based on the Hybrid Modal Technique [12], where the termination is modeled by the method of moments. It is worth noting that the MM results converge rather slowly, and a smaller number of modes may not yield correct values for the RCS. On the other hand, the inclusion of more modes requires the inversion of larger matrices which may be possibly associated with worse matrix condition numbers.

Figure 5 depicts the amplitudes of the elements of the generalized scattering matrix [**S**] corresponding to the above geometry. It is evident that coupling exists only among modes of the same order (of the cylindrical function), and this can be proven analytically. Also, TM and TE modes do not couple to TM and TE modes (respectively) of different angular variation, e.g. a TM mode of $\cos n\phi$ variation does not couple to a TM of $\sin n\phi$ variation. However, intercoupling among TM and TE modes does occur *only* for modes having different angular variation (i.e. one of them having a $\cos n\phi$ and the other a $\sin n\phi$ variation). Moreover, the coupling between any two given modes is invariant if the angular variations of *both* modes are switched. Finally, all modes couple significantly only to their closest neighbors, resulting to almost banded scattering matrices. Large off-diagonal elements (whenever they occur) correspond to evanescent modes.

3 Periodic Array of Grooves Termination

3.1 Mode Matching Formulation

In this section we apply the Mode Matching (MM) technique to the more complicated geometry of a hollow cylinder terminated by a cylindrical array of grooves as shown in Fig. 2. Evidently, the modes in region 1 are identical to those of the previous geometry. To provide a modal representation of the fields in region 2, we will assume that the array consists of J grooves, that are essentially cylindrical (pie-shell) sectors of angular extent ϕ_w. In each of the pie-shell sectors the wave equation can be solved analytically, leading to the modal solution given in Appendix I. The modes in Appendix I refer to the κ^{th} groove whose rightmost edge makes an angle

$$\phi_\kappa = \phi_1 + (\kappa - 1)\frac{2\pi}{J} \tag{27}$$

with the x-axis. Note that no TEM mode exists within the grooves, since there is no seperation among the conducting surfaces of each groove.

The fields in each region can be again represented by (1)- (7), with the understanding that $\mathbf{e}_{2,n}$ and $\mathbf{h}_{2,n}$ are different. To find the coefficients c_m, d_m, b_m we proceed with the enforcement of the continuity conditions of the tangential fields at the interface ($z = 0$), viz.

$$\mathbf{E}_1^{ti}|_{z=0} + \mathbf{E}_1^{tr}|_{z=0} = \mathbf{E}_2^{t}|_{z=0} \tag{28}$$

$$\mathbf{H}_1^{ti}|_{z=0} + \mathbf{H}_1^{tr}|_{z=0} = \mathbf{H}_2^{t}|_{z=0} \tag{29}$$

$$\forall \rho \in [a,b], \forall \phi \in [\phi_\kappa, \phi_\kappa + \phi_w], \forall \kappa \in \{1,...,J\}$$

and to these we must add

$$\mathbf{E}_1^{ti}|_{z=0} + \mathbf{E}_1^{tr}|_{z=0} = \mathbf{0} \qquad \text{elsewhere} \tag{30}$$

i.e. on the metallic portion of the interface. Following the same mode matching procedure used for the previous geometry, (28)-(30) can be used to determine the scattering matrix of the structure. As before, upon applying the MM technique at the interface we obtain a system of equations for the mode coefficients. Then, on eliminating the coefficients of the modes in region 2 (groove region) we deduce that (26) is again valid except that the matrix [**W**] must be replaced by

$$[\mathbf{W}] = \sum_{\kappa=1}^{J} [\mathbf{L}_\kappa]^T \Big([\mathbf{I}] + [\mathbf{D}]\,[\mathbf{S}_{\kappa,end}]\,[\mathbf{D}] \Big)\Big([\mathbf{I}] - [\mathbf{D}]\,[\mathbf{S}_{\kappa,end}]\,[\mathbf{D}] \Big)^{-1} [\mathbf{L}_\kappa] \tag{31}$$

in which [**I**] is the unit matrix and $[\mathbf{S}_{\kappa,end}]$ is the modal scattering matrix of the back end of each groove. The elements of the $[\mathbf{L}_\kappa]$ and [**D**] matrices are given by

$$L_{\kappa,mn} \equiv \frac{P_{\kappa,mn}}{U_n} \tag{32}$$

$$P_{\kappa,mn} \equiv \int_a^b \int_{\phi_\kappa}^{\phi_\kappa+\phi_w} \mathbf{e}_{2,\kappa,m} \cdot \mathbf{e}_{1,n} \rho d\rho d\phi \tag{33}$$

$$U_n \equiv \int_0^b \int_0^{2\pi} \mathbf{e}_{1,n} \cdot \mathbf{e}_{1,n} \rho d\rho d\phi \tag{34}$$

$$D_{mn} \equiv \delta_{mn} \exp\{-j\beta_{2,m} l_2\} \tag{35}$$

Clearly, the expressions derived for the scattering matrix of the periodic groove termination are quite similar to the corresponding ones for the cylindrical hub. However, apart from the sum in (31) over the total number of

grooves, there are a few additional important differences. The order of the cylindrical functions in region 2 is, in general, non-integer and, of course, the ϕ-integration is performed only over the angular extent of the groove. Consequently, in general, all modes between regions 1 and 2 couple to each other, leading to a fully populated matrix $[\mathbf{L}_\kappa]$. In the case of the stub termination, orthogonality among the trigonometric functions resulted in coupling only among those modes of the same order (i.e. same order of the Bessel functions), leading to banded matrices. Nevertheless, the scattering matrix $[\mathbf{S}]$ must be banded [7], and this indeed occurs after carrying out the matrix operations specified in (26),(31). Finally, we note that as opposed to the single hub termination, the elements of the $[\mathbf{L}_\kappa]$ matrix must be evaluated by numerical integration.

3.2 Numerical Results

Fig. 6 shows RCS results for the geometry of Fig. 2. The number of modes used in region 1 was 1000 (i.e. 25 orders of the Bessel functions, by 10 modes per order, by 2 for both TM and TE modes, by 2 for both angular variations), and 140 modes were used in region 2 (7 orders by 10 modes per order by 2 for both TM and TE modes). The pattern was obtained by integrating the aperture equivalent currents, without including rim diffraction. To validate the computer code, we computed and compared the transverse fields at both sides of the interface separating regions 1 and 2. Fig. 7*a* depicts the ρ component of the total field at both sides of the interface, whereas Fig. 7*b* depicts the ϕ component. The waveguide field is plotted at $\rho = 3\lambda$, as a function of ϕ, for an incidence angle of $\theta_i = 0^o$ and ϕ polarization. It is apparent that the transverse fields are continuous across the interface between regions 1 and 2, implying that the boundary conditions (28) and (29) are satisfied. Moreover, the total tangential field on the metallic surface of the blades is 20 or so dB below the field values elsewhere. The transverse field values on the top surface of the hub were also found to be very low, implying that the boundary condition (30) is also satisfied fairly well. Consequently, since all boundary conditions are satisfied, the RCS patterns given in Fig. 6 must be accurate within the limits of the Kirchhoff approximation employed at the aperture of the cylinder's open end.

4 Periodic Array of Curved Blades Termination

4.1 Mode Matching Formulation

None of the previously considered geometries represents a realistic jet inlet termination. With the goal of characterizing the scattering of more realistic jet inlet terminations, in this section we present a mode matching solution for an inlet termination consisting of a special class of curved blades (see Fig. 3) Basically, each blade is allowed to be curved with the restriction that its base still remains perpendicular to the hub at any point of intersection (see Fig. 3, front view). However, the angle formed by the rightmost edge of the boundary of the blade and the x-axis is allowed to vary with z. Specifically the blade or groove boundary is now allowed to make an angle

$$\phi_\kappa(z) = \phi_1(0) + (\kappa - 1)\frac{2\pi}{J} + F(z) \tag{36}$$

with the x axis, where F is an arbitrary function of the longitudinal coordinate z and is measured in radians. Of course, at the face of the fan ($z = 0$), the condition

$$F(0) = 0 \tag{37}$$

should be satisfied, so that (36) is self-consistent. Note that (36) is valid provided all blades have the same z-dependence, resulting in grooves of constant width for any z; that is each pair of blades is assumed to form an identical guiding region, as is typically the case with realistic engine compressor configurations.

To analytically characterize the fields within each groove formed by a pair of these curved blades, we note its similarities with the straight groove. We observe that for any given z the cross-section of the curved blade pair is identical to that of a straight blade pair, the only difference being the rotation about the z axis. Consequently, the modes expressed in Appendix I still satisfy the appropriate boundary conditions, provided ϕ_κ is a function of z satisfying (36). It is therefore reasonable to assume that the transverse fields within the κ^{th} groove (i.e. the waveguide region between the $(\kappa - 1)^{th}$ and the κ^{th} blades) can be expressed as a superposition of the aforementioned modes, viz.

$$\mathbf{E}_\kappa^t = \sum_{i=1}^{\infty} V_{\kappa,i}(z)\mathbf{e}_{\kappa,i}(\rho,\phi;z) \tag{38}$$

$$\mathbf{H}_\kappa^t = \sum_{i=1}^{\infty} I_{\kappa,i}(z)\mathbf{h}_{\kappa,i}(\rho,\phi;z) \tag{39}$$

It can be shown [14] that the coefficients $V_{\kappa,i}(z), I_{\kappa,i}(z)$ satisfy the following infinite system of differential equations:

$$\frac{d}{dz}\begin{Bmatrix} V_{\kappa,1}(z) \\ V_{\kappa,2}(z) \\ \cdots \\ I_{\kappa,1}(z) \\ I_{\kappa,2}(z) \\ \cdots \end{Bmatrix} = \begin{bmatrix} T_{11}(z) & T_{12}(z) & \cdots & -j\beta_1 Z_1 & 0 & \cdots \\ T_{21}(z) & T_{22}(z) & \cdots & 0 & -j\beta_2 Z_2 & \cdots \\ \cdots & \cdots & \cdots & \cdots & \cdots & \cdots \\ -\frac{j\beta_1}{Z_1} & 0 & \cdots & -T_{11}(z) & -T_{21}(z) & \cdots \\ 0 & -\frac{j\beta_2}{Z_2} & \cdots & -T_{12}(z) & -T_{22}(z) & \cdots \\ \cdots & \cdots & \cdots & \cdots & \cdots & \cdots \end{bmatrix} \begin{Bmatrix} V_{\kappa,1}(z) \\ V_{\kappa,2}(z) \\ \cdots \\ I_{\kappa,1}(z) \\ I_{\kappa,2}(z) \\ \cdots \end{Bmatrix} \tag{40}$$

where

$$T_{ij}(z) \equiv \int\int_{S_\kappa(z)} \mathbf{e}_{\kappa,j} \cdot \frac{\partial \mathbf{e}_{\kappa,i}}{\partial z} d^2S \tag{41}$$

β_i is the propagation constant, Z_i is the impedance of the i^{th} mode and $S_\kappa(z)$ is the cross-section of the κ^{th} groove at z. Given $F(z)$, analytical evaluation of $\frac{\partial \mathbf{e}_{\kappa,i}}{\partial z}$ is feasible. Also, in (41) the integration over ϕ can be performed in closed form, but the integration over ρ must be done numerically.

It is possible to solve (40) analytically, provided the geometry obeys certain restrictions. First we note that the cross-section of all grooves remains invariant in shape along the axis, and thus the propagation constants and the mode impedances do not depend on the longitudinal coordinate z. Therefore, (40) can be rewritten more compactly as

$$\frac{d}{dz}\{\mathbf{U}_\kappa(z)\} = [\mathbf{M}(z)]\{\mathbf{U}_\kappa(z)\} \tag{42}$$

where

$$\{\mathbf{U}_\kappa(z)\} \equiv \left\{ \begin{array}{c} V_{\kappa,1}(z) \\ V_{\kappa,2}(z) \\ \cdots \\ Z_1 I_{\kappa,1}(z) \\ Z_2 I_{\kappa,2}(z) \\ \cdots \end{array} \right\} \tag{43}$$

$$[\mathbf{M}(z)] \equiv \left[\begin{array}{cc} [\mathbf{P}] F'(z) & [\mathbf{D}] \\ [\mathbf{D}] & -[\mathbf{P}]^T F'(z) \end{array} \right] \tag{44}$$

$$[\mathbf{D}] = \mathbf{diag}[-j\beta_1, -j\beta_2 ...] \tag{45}$$

$$P_{ij} \equiv -\int\int_{S_\kappa(z)} \mathbf{e}_{\kappa,j} \cdot \frac{\partial \mathbf{e}_{\kappa,i}}{\partial \phi_\kappa} d^2 S \tag{46}$$

and the prime on $F(z)$ denotes differentation with respect to z. From the explicit expressions of $\mathbf{e}_{\kappa,i}$ in Appendix I, we conclude that P_{ij} does not depend on z. Most importantly, the elements of $[\mathbf{M}]$ carry a dependence on z only through the presence of $F'(z)$. That is if $F'(z) = const.$, $[\mathbf{M}]$ becomes independent of z and this can be exploited to obtain a closed form solution of $\{\mathbf{U}_\kappa(z)\}$. Specifically, it follows that if $F(z)$ is linear in z, the explicit solution for $\{\mathbf{U}_\kappa(z)\}$ is

$$\{\mathbf{U}_\kappa(z)\} = \exp(z[\mathbf{M}])\{\mathbf{U}_\kappa(0)\} \tag{47}$$

where $\{\mathbf{U}_\kappa(0)\}$ is the value of $\{\mathbf{U}_\kappa(z)\}$ at $z = 0$. Although this is an explicit expression, the numerical evaluation of the matrix exponential is not necessarily an easy task. To evaluate it, the standard approach is to rewrite it as [15]

$$\mathrm{e}^{z[\mathbf{M}]} = [\mathbf{K}]\,\mathbf{diag}\left[\mathrm{e}^{z\lambda_1}, \mathrm{e}^{z\lambda_2}, ..., \mathrm{e}^{z\lambda_n}\right][\mathbf{K}]^{-1} \tag{48}$$

where λ_i denote the eigenvalues of $[\mathbf{M}]$ and $[\mathbf{K}]$ is the matrix of the corresponding eigenvectors [15]. The latter expression is valid provided the eigenvalues are distinct, which is expected to hold in this situation, unless degenerate generalized modes exist. In theory, the matrix $[\mathbf{M}]$ is infinite, but for practical purposes it must be truncated, taking into account only the traveling and most significant evanescent modes. It is important to note that,

as shown in [7], if λ is an eigenvalue of $[\mathbf{M}]$, then $-\lambda$ is also an eigenvalue of $[\mathbf{M}]$. This is an expected property since each guiding region supports identical pairs of modes propagating along the $+z$ and $-z$ directions. By making use of this property, (47) can be rewritten as

$$\left\{ \begin{array}{c} \mathbf{V}_\kappa(z) \\ \mathbf{J}_\kappa(z) \end{array} \right\} = \left[\begin{array}{cc} [\mathbf{K}_{11}] & [\mathbf{K}_{12}] \\ [\mathbf{K}_{21}] & [\mathbf{K}_{22}] \end{array} \right] \left[\begin{array}{cc} \mathrm{e}^{[\mathbf{\Lambda}]z} & \mathbf{0} \\ \mathbf{0} & \mathrm{e}^{-[\mathbf{\Lambda}]z} \end{array} \right] \left[\begin{array}{cc} [\mathbf{K}_{11}] & [\mathbf{K}_{12}] \\ [\mathbf{K}_{21}] & [\mathbf{K}_{22}] \end{array} \right]^{-1} \left\{ \begin{array}{c} \mathbf{V}_\kappa(0) \\ \mathbf{J}_\kappa(0) \end{array} \right\} \tag{49}$$

where

$$[\mathbf{\Lambda}] \equiv \mathbf{diag}\,[\lambda_1, ..., \lambda_\rho] \tag{50}$$

$$\begin{aligned} Re(\lambda_i) &> 0 \text{ or} && (51) \\ Re(\lambda_i) &= 0, Im(\lambda_i) \geq 0 && (52) \\ &\text{and} \\ J_{\kappa,i} &\equiv Z_{\kappa,i} I_{\kappa,i} && (53) \end{aligned}$$

We remark that (49) is a much more simplified expression and its form is crucial in making reliable numerical calculations. In the following analysis it turns out that only $\mathrm{e}^{-[\mathbf{\Lambda}]l}, l \geq 0$ appears in the calculations. Therefore, since the real parts of the elements of $[\mathbf{\Lambda}]$ are chosen to be nonnegative, no numerical instabilities occur.

Using (49) and following the analysis in [7], the scattering matrix of the array of curved grooves at its interface is derived to be

$$[\mathbf{S}] = ([\mathbf{W}] + [\mathbf{I}])^{-1} ([\mathbf{W}] - [\mathbf{I}]) \tag{54}$$

where

$$[\mathbf{W}] = \sum_{\kappa=1}^{J} [\mathbf{L}_\kappa]^T [\mathbf{F}_\kappa] [\mathbf{G}_\kappa]^{-1} [\mathbf{L}_\kappa] \tag{55}$$

and $[\mathbf{I}]$ is the unit matrix. Also

$$\begin{aligned} [\mathbf{F}_\kappa] &\equiv [\mathbf{K}_{11}] + [\mathbf{K}_{12}] [\mathbf{R}_\kappa] && (56) \\ [\mathbf{G}_\kappa] &\equiv [\mathbf{K}_{21}] + [\mathbf{K}_{22}] [\mathbf{R}_\kappa] && (57) \\ [\mathbf{R}_\kappa] &\equiv \mathrm{e}^{-[\mathbf{\Lambda}]l_2} [\mathbf{K}_{12}]^{-1} [\mathbf{S}_{\kappa,end}] [\mathbf{K}_{11}] \mathrm{e}^{-[\mathbf{\Lambda}]l_2} && (58) \end{aligned}$$

$[\mathbf{S}_{\kappa,end}]$ is the scattering matrix at the back end ($z = -l_2$) of the κ^{th} groove, l_2 is the length of the compressor and $[\mathbf{L}_\kappa]$ is identical to the $[\mathbf{L}_\kappa]$ matrix defined in section 3.

4.2 Numerical Results

Fig. 8 shows RCS patterns for the geometry of Fig. 3. A total of 1000 modes were used in region 1 (i.e. 25 orders of the Bessel functions, by 10 modes per order, by 2 for both TM and TE modes, by 2 for both angular variations), and 60 modes were used in region 2 (6 orders by 5 modes per order, by 2 for both TM and TE modes). Again, the effect of the rim was not taken into account (no equivalent Ufimtsef currents on the rim were taken into consideration). For validation purposes we relied on the examination of the boundary conditions satisfied by the transverse fields. Fig. 9*a* depicts the ρ component of the total field at both sides of the interface, while Fig. 9*b* depicts the ϕ component. The field is plotted at $\rho = 3\lambda$, as a function of ϕ, for an incidence angle of $\theta_i = 0^o$ and ϕ polarization. As in the case of the straight blades, the incident field is also plotted for reference purposes. It is evident that the fields on each side of the interface are almost equal and the tangential fields on all metallic surfaces are very low. Consequently, the boundary conditions are satisfied, implying that the RCS plots in Fig. 9 are correct within the limits of the Kirchhoff approximation employed at the aperture.

5 Comparison to measured data

Two actual models corresponding to the aforementioned geometries were specified by the University of Michigan and were measured at the General Electric Aircraft Engines, Cincinnati OH. The models had the following specifications: Outer radius $b = 15$ cm, inner radius $a = 7.5$ cm, length of region 1 $l_1 = 20$ cm, length of region 2 $l_2 = 10$ cm, 8 blades, 4 degrees wide each. The curved blades' total twist angle was 30 degrees. At the interface between region 1 and region 2 the leading edge of the first blade was aligned with the measurement plane. Measurements were taken for four different frequencies, namely 4, 6, 8, and 10 GHz. Comparisons between calculated and measured data are given in Figures 10-21. The agreement is satisfactory, and the dis-

repancies are mostly due to the Kirchhoff approximation at the aperture of the inlet. This is evident from the figures which show that the agreement improves for larger electrical dimensions of the geometry, where the Kirchhoff approximation is more reliable. Also, the data clearly demonstrate that the field continuity and boundary conditions at the interface between region 1 and region 2 are satisfied, which is an additional evidence that the disagreements are due to the Kirchhoff approximation.

6 Concluding Remarks

The Mode Matching Technique was applied to characterize a cylindrical waveguide terminated by a number of non-trivial engine-like configurations. The motivation of this study was to generate reference data for validating other, more general numerical techniques. Three different termination geometries were analyzed, including a termination consisting of an array of curved grooves. This termination was of most interest because of its closer resemblance to the jet engine face whereas the stub and straight groove terminations served to validate the mode-matching implementation for this application. Scattering results were presented for each configuration and a serious effort was devoted toward their validation either by comparing them to other reference solutions (when available) or by examining the satisfaction of the boundary conditions at the interface of the termination. Finally, comparisons between calculated data and actual measurements were also presented, and the agreement was considered to be sufficiently good, given that the inaccurate Kirchhoff approximation was employed in the calculations.

7 Acknowledgement

The authors are indebted to Dr. R. J. Burkholder of the Ohio State University for the supply of several numerical results based on the Hybrid Moment-Method Modal Technique.

8 Appendix I: Explicit expressions of the modes in the cavity.

The transverse fields corresponding to each mode are given by: (the longitudinal dependence has been suppressed; **e** stands for the electric and **h** stands for the magnetic field)

Region 1.

$$\begin{aligned}
\mathbf{e}_{1,np}^{TM} &= N_{1,np}^{TM}\frac{\beta_{1,np}^{TM}}{\omega\epsilon}\Big[\gamma_{1,np}^{TM}J_n'\left(\gamma_{1,np}^{TM}\rho\right)\left\{\begin{array}{c}\sin n\phi\\ \cos n\phi\end{array}\right\}\mathbf{u}_\rho + \\
&+ \frac{n}{\rho}J_n\left(\gamma_{1,np}^{TM}\rho\right)\left\{\begin{array}{c}\cos n\phi\\ -\sin n\phi\end{array}\right\}\mathbf{u}_\phi\Big] \qquad (59)\\
\mathbf{h}_{1,np}^{TM} &= N_{1,np}^{TM}\Big[\frac{n}{\rho}J_n\left(\gamma_{1,np}^{TM}\rho\right)\left\{\begin{array}{c}\cos n\phi\\ -\sin n\phi\end{array}\right\}\mathbf{u}_\rho - \\
&- \gamma_{1,np}^{TM}J_n'\left(\gamma_{1,np}^{TM}\rho\right)\left\{\begin{array}{c}\sin n\phi\\ \cos n\phi\end{array}\right\}\mathbf{u}_\phi\Big] \qquad (60)\\
\mathbf{e}_{1,np}^{TE} &= N_{1,np}^{TE}\Big[-\frac{n}{\rho}J_n\left(\gamma_{1,np}^{TE}\rho\right)\left\{\begin{array}{c}\cos n\phi\\ -\sin n\phi\end{array}\right\}\mathbf{u}_\rho + \\
&+ \gamma_{1,np}^{TE}J_n'\left(\gamma_{1,np}^{TE}\rho\right)\left\{\begin{array}{c}\sin n\phi\\ \cos n\phi\end{array}\right\}\mathbf{u}_\phi\Big] \qquad (61)\\
\mathbf{h}_{1,np}^{TE} &= N_{1,np}^{TE}\frac{\beta_{1,np}^{TE}}{\omega\mu}\Big[\gamma_{1,np}^{TE}J_n'\left(\gamma_{1,np}^{TE}\rho\right)\left\{\begin{array}{c}\sin n\phi\\ \cos n\phi\end{array}\right\}\mathbf{u}_\rho + \\
&+ \frac{n}{\rho}J_n\left(\gamma_{1,np}^{TE}\rho\right)\left\{\begin{array}{c}\cos n\phi\\ -\sin n\phi\end{array}\right\}\mathbf{u}_\phi\Big] \qquad (62)
\end{aligned}$$

where the $\gamma_{1,np}^{TM}, \gamma_{1,np}^{TE}$ are found from

$$\begin{aligned}
J_n(\gamma_{1,np}^{TM}b) &= 0 \qquad (63)\\
J_n'(\gamma_{1,np}^{TE}b) &= 0 \qquad (64)
\end{aligned}$$

The normalization factors are arbitrary. They are usually defined by [16]

$$N_{1,np}^{TM} \equiv \omega\epsilon\left[\frac{1}{2}J_n'\left(\gamma_{1,np}^{TM}b\right)\gamma_{1,np}^{TM}b\sqrt{\pi kY\beta_{1,np}^{TM}\epsilon_n}\right]^{-1} \tag{65}$$

$$N_{1,np}^{TE} \equiv \left[\frac{1}{2}J_n\left(\gamma_{1,np}^{TE}b\right)\sqrt{\pi kZ\beta_{1,np}^{TE}\epsilon_n\left\{\left(\gamma_{1,np}^{TE}b\right)^2 - n^2\right\}}\right]^{-1} \tag{66}$$

$$\epsilon_n \equiv \begin{cases} 2 & n = 0 \\ 1 & n \neq 0 \end{cases} \tag{67}$$

and on the basis of this normalization

$$\frac{1}{2}\int\int_{S_0} \mathbf{e}_{1,np} \times \mathbf{h}_{1,np} \cdot d^2\mathbf{S} = 1 \tag{68}$$

Region 2 (Cylidrical Hub Termination).

$$\begin{aligned}
\mathbf{e}_{2,mq}^{TM} &= \gamma_{2,mq}^{TM}\left[Y_m\left(\gamma_{2,mq}^{TM}a\right)J_m'\left(\gamma_{2,mq}^{TM}\rho\right) - J_m\left(\gamma_{2,mq}^{TM}a\right)Y_m'\left(\gamma_{2,mq}^{TM}\rho\right)\right]\cdot \\
&\cdot N_{2,mq}^{TM}\frac{\beta_{2,mq}^{TM}}{\omega\epsilon}\left\{\begin{array}{c}\sin m\phi\\ \cos m\phi\end{array}\right\}\mathbf{u}_\rho + \\
&+ \frac{m}{\rho}\left[Y_m\left(\gamma_{2,mq}^{TM}a\right)J_m\left(\gamma_{2,mq}^{TM}\rho\right) - J_m\left(\gamma_{2,mq}^{TM}a\right)Y_m\left(\gamma_{2,mq}^{TM}\rho\right)\right]\cdot \\
&\cdot N_{2,mq}^{TM}\frac{\beta_{2,mq}^{TM}}{\omega\epsilon}\left\{\begin{array}{c}\cos m\phi\\ -\sin m\phi\end{array}\right\}\mathbf{u}_\phi
\end{aligned} \tag{69}$$

$$\begin{aligned}
\mathbf{h}_{2,mq}^{TM} &= \frac{m}{\rho}\left[Y_m\left(\gamma_{2,mq}^{TM}a\right)J_m\left(\gamma_{2,mq}^{TM}\rho\right) - J_m\left(\gamma_{2,mq}^{TM}a\right)Y_m\left(\gamma_{2,mq}^{TM}\rho\right)\right]\cdot \\
&\cdot N_{2,mq}^{TM}\left\{\begin{array}{c}\cos m\phi\\ -\sin m\phi\end{array}\right\}\mathbf{u}_\rho - \\
&- \gamma_{2,mq}^{TM}\left[Y_m\left(\gamma_{2,mq}^{TM}a\right)J_m'\left(\gamma_{2,mq}^{TM}\rho\right) - J_m\left(\gamma_{2,mq}^{TM}a\right)Y_m'\left(\gamma_{2,mq}^{TM}\rho\right)\right]\cdot \\
&\cdot N_{2,mq}^{TM}\left\{\begin{array}{c}\sin m\phi\\ \cos m\phi\end{array}\right\}\mathbf{u}_\phi
\end{aligned} \tag{70}$$

$$\begin{aligned}
\mathbf{e}_{2,mq}^{TE} &= -\frac{m}{\rho}\left[Y_m'\left(\gamma_{2,mq}^{TE}a\right)J_m\left(\gamma_{2,mq}^{TE}\rho\right) - J_m'\left(\gamma_{2,mq}^{TE}a\right)Y_m\left(\gamma_{2,mq}^{TE}\rho\right)\right]\cdot \\
&\cdot N_{2,mq}^{TE}\left\{\begin{array}{c}\cos m\phi\\ -\sin m\phi\end{array}\right\}\mathbf{u}_\rho +
\end{aligned}$$

$$+ \quad \gamma_{2,mq}^{TE}\left[Y_m'\left(\gamma_{2,mq}^{TE}a\right)J_m'\left(\gamma_{2,mq}^{TE}\rho\right) - J_m'\left(\gamma_{2,mq}^{TE}a\right)Y_m'\left(\gamma_{2,mq}^{TE}\rho\right)\right]\cdot$$

$$\cdot \quad N_{2,mq}^{TE}\left\{\begin{array}{c}\sin m\phi\\ \cos m\phi\end{array}\right\}\mathbf{u}_\phi \tag{71}$$

$$\mathbf{h}_{2,mq}^{TE} = \gamma_{2,mq}^{TE}\left[Y_m'\left(\gamma_{2,mq}^{TE}a\right)J_m'\left(\gamma_{2,mq}^{TE}\rho\right) - J_m'\left(\gamma_{2,mq}^{TE}a\right)Y_m'\left(\gamma_{2,mq}^{TE}\rho\right)\right]\cdot$$

$$\cdot \quad N_{2,mq}^{TE}\frac{\beta_{2,mq}^{TE}}{\omega\mu}\left\{\begin{array}{c}\sin m\phi\\ \cos m\phi\end{array}\right\}\mathbf{u}_\rho +$$

$$+ \quad \frac{m}{\rho}\left[Y_m'\left(\gamma_{2,mq}^{TE}a\right)J_m\left(\gamma_{2,mq}^{TE}\rho\right) - J_m'\left(\gamma_{2,mq}^{TE}a\right)Y_m\left(\gamma_{2,mq}^{TE}\rho\right)\right]\cdot$$

$$\cdot \quad N_{2,mq}^{TE}\frac{\beta_{2,mq}^{TE}}{\omega\mu}\left\{\begin{array}{c}\cos m\phi\\ -\sin m\phi\end{array}\right\}\mathbf{u}_\phi \tag{72}$$

$$\mathbf{e}_2^{TEM} = N_2^{TEM}\frac{1}{\rho}\mathbf{u}_\rho \tag{73}$$

$$\mathbf{h}_2^{TEM} = N_2^{TEM}\frac{1}{Z\rho}\mathbf{u}_\phi \tag{74}$$

where the $\gamma_{2,mq}^{TM}, \gamma_{2,mq}^{TE}$ are found from

$$Y_m(\gamma_{2,mq}^{TM}a)J_m(\gamma_{2,mq}^{TM}b) - J_m(\gamma_{2,mq}^{TM}a)Y_m(\gamma_{2,mq}^{TM}b) = 0 \tag{75}$$

$$Y_m'(\gamma_{2,mq}^{TE}a)J_m'(\gamma_{2,mq}^{TE}b) - J_m'(\gamma_{2,mq}^{TE}a)Y_m'(\gamma_{2,mq}^{TE}b) = 0 \tag{76}$$

The normalization factors $N_{2,mq}^{TM}, N_{2,mq}^{TE}, N_2^{TEM}$ are again arbitrary, but are usually defined by [17]

$$N_{2,mq}^{TM} \equiv -\frac{\omega\epsilon}{\beta_{2,np}^{TM}}\frac{1}{2}\sqrt{\pi\left(3-\epsilon_m\right)}\left[\frac{J_m^2\left(\gamma_{2,mq}^{TM}a\right)}{J_m^2\left(\gamma_{2,mq}^{TM}b\right)} - 1\right]^{-\frac{1}{2}} \tag{77}$$

$$N_{2,mq}^{TE} \equiv \frac{1}{2}\sqrt{\pi\left(3-\epsilon_m\right)}\left\{\left[\frac{J_m'\left(\gamma_{2,mq}^{TE}a\right)}{J_m'\left(\gamma_{2,mq}^{TE}b\right)}\right]^2\left[1-\left(\frac{m}{\gamma_{2,mq}^{TE}b}\right)^2\right] - \right.$$

$$\left. - \quad \left[1-\left(\frac{m}{\gamma_{2,mq}^{TE}a}\right)^2\right]\right\}^{-\frac{1}{2}} \tag{78}$$

$$N_2^{TEM} \equiv \frac{1}{\sqrt{2\pi \ln(b/a)}} \tag{79}$$

$$\epsilon_n \equiv \begin{cases} 2 & n = 0 \\ 1 & n \neq 0 \end{cases} \tag{80}$$

Region 2, κ^{th} groove (groove array termination).

$$\begin{aligned}
\mathbf{e}_{2,\kappa,mq}^{TM} &= \gamma_{2,mq}^{TM} \left[Y_\nu\left(\gamma_{2,mq}^{TM} a\right) J_\nu'\left(\gamma_{2,mq}^{TM} \rho\right) - J_\nu\left(\gamma_{2,mq}^{TM} a\right) Y_\nu'\left(\gamma_{2,mq}^{TM} \rho\right) \right] \cdot \\
&\cdot N_{2,mq}^{TM} \frac{\beta_{2,mq}^{TM}}{\omega\epsilon} \sin\left[\nu\left(\phi - \phi_\kappa\right)\right] \mathbf{u}_\rho + \\
&+ \frac{\nu}{\rho} \left[Y_\nu\left(\gamma_{2,mq}^{TM} a\right) J_\nu\left(\gamma_{2,mq}^{TM} \rho\right) - J_\nu\left(\gamma_{2,mq}^{TM} a\right) Y_\nu\left(\gamma_{2,mq}^{TM} \rho\right) \right] \cdot \\
&\cdot N_{2,mq}^{TM} \frac{\beta_{2,mq}^{TM}}{\omega\epsilon} \cos\left[\nu\left(\phi - \phi_\kappa\right)\right] \mathbf{u}_\phi
\end{aligned} \tag{81}$$

$$\begin{aligned}
\mathbf{h}_{2,\kappa,mq}^{TM} &= \frac{\nu}{\rho} \left[Y_\nu\left(\gamma_{2,mq}^{TM} a\right) J_\nu\left(\gamma_{2,mq}^{TM} \rho\right) - J_\nu\left(\gamma_{2,mq}^{TM} a\right) Y_\nu\left(\gamma_{2,mq}^{TM} \rho\right) \right] \cdot \\
&\cdot N_{2,mq}^{TM} \cos\left[\nu\left(\phi - \phi_\kappa\right)\right] \mathbf{u}_\rho - \\
&- \gamma_{2,mq}^{TM} \left[Y_\nu\left(\gamma_{2,mq}^{TM} a\right) J_\nu'\left(\gamma_{2,mq}^{TM} \rho\right) - J_\nu\left(\gamma_{2,mq}^{TM} a\right) Y_\nu'\left(\gamma_{2,mq}^{TM} \rho\right) \right] \cdot \\
&\cdot N_{2,mq}^{TM} \sin\left[\nu\left(\phi - \phi_\kappa\right)\right] \mathbf{u}_\phi
\end{aligned} \tag{82}$$

$$\begin{aligned}
\mathbf{e}_{2,\kappa,mq}^{TE} &= \frac{\nu}{\rho} \left[Y_\nu'\left(\gamma_{2,mq}^{TE} a\right) J_\nu\left(\gamma_{2,mq}^{TE} \rho\right) - J_\nu'\left(\gamma_{2,mq}^{TE} a\right) Y_\nu\left(\gamma_{2,mq}^{TE} \rho\right) \right] \cdot \\
&\cdot N_{2,mq}^{TE} \sin\left[\nu\left(\phi - \phi_\kappa\right)\right] \mathbf{u}_\rho + \\
&+ \gamma_{2,mq}^{TE} \left[Y_\nu'\left(\gamma_{2,mq}^{TE} a\right) J_\nu'\left(\gamma_{2,mq}^{TE} \rho\right) - J_\nu'\left(\gamma_{2,mq}^{TE} a\right) Y_\nu'\left(\gamma_{2,mq}^{TE} \rho\right) \right] \cdot \\
&\cdot N_{2,mq}^{TE} \cos\left[\nu\left(\phi - \phi_\kappa\right)\right] \mathbf{u}_\phi
\end{aligned} \tag{83}$$

$$\begin{aligned}
\mathbf{h}_{2,\kappa,mq}^{TE} &= \gamma_{2,mq}^{TE} \left[Y_\nu'\left(\gamma_{2,mq}^{TE} a\right) J_\nu'\left(\gamma_{2,mq}^{TE} \rho\right) - J_\nu'\left(\gamma_{2,mq}^{TE} a\right) Y_\nu'\left(\gamma_{2,mq}^{TE} \rho\right) \right] \cdot \\
&\cdot N_{2,mq}^{TE} \frac{\beta_{2,mq}^{TE}}{\omega\mu} \cos\left[\nu\left(\phi - \phi_\kappa\right)\right] \mathbf{u}_\rho - \\
&- \frac{\nu}{\rho} \left[Y_\nu'\left(\gamma_{2,mq}^{TE} a\right) J_\nu\left(\gamma_{2,mq}^{TE} \rho\right) - J_\nu'\left(\gamma_{2,mq}^{TE} a\right) Y_\nu\left(\gamma_{2,mq}^{TE} \rho\right) \right] \cdot
\end{aligned}$$

$$\cdot \quad N_{2,mq}^{TE} \frac{\beta_{2,mq}^{TE}}{\omega\mu} \sin\left[\nu\left(\phi - \phi_\kappa\right)\right] \mathbf{u}_\phi \tag{84}$$

where the $\gamma_{2,mq}^{TM}, \gamma_{2,mq}^{TE}$ are found from

$$J_\nu(\gamma_{2,mq}^{TM} a) Y_\nu(\gamma_{2,mq}^{TM} b) - J_\nu(\gamma_{2,mq}^{TM} b) Y_\nu(\gamma_{2,mq}^{TM} a) = 0 \tag{85}$$

$$J'_\nu(\gamma_{2,mq}^{TE} a) Y'_\nu(\gamma_{2,mq}^{TE} b) - J'_\nu(\gamma_{2,mq}^{TE} b) Y'_\nu(\gamma_{2,mq}^{TE} a) = 0 \tag{86}$$

and

$$\nu = \frac{m\pi}{\phi_w}, \qquad m = 0, 1, 2, ... \tag{87}$$

$$N_{2,mq}^{TM} \equiv -\frac{\omega\epsilon}{\beta_{2,mq}^{TM}} \frac{1}{2} \sqrt{\frac{\phi_w\left(3 - \epsilon_m\right)}{2}} \left[\frac{J_\nu^2\left(\gamma_{2,mq}^{TM} a\right)}{J_\nu^2\left(\gamma_{2,mq}^{TM} b\right)} - 1\right]^{-\frac{1}{2}} \tag{88}$$

$$N_{2,mq}^{TE} \equiv \frac{1}{2} \sqrt{\frac{\phi_w\left(3 - \epsilon_m\right)}{2}} \left\{ \left[\frac{J'_\nu\left(\gamma_{2,mq}^{TE} a\right)}{J'_\nu\left(\gamma_{2,mq}^{TE} b\right)}\right]^2 \left[1 - \left(\frac{\nu}{\gamma_{2,mq}^{TE} b}\right)^2\right] - \right.$$

$$\left. - \left[1 - \left(\frac{\nu}{\gamma_{2,mq}^{TE} a}\right)^2\right] \right\}^{-\frac{1}{2}} \tag{89}$$

$$\epsilon_m \equiv \begin{cases} 2 & m = 0 \\ 1 & m \neq 0 \end{cases} \tag{90}$$

ϕ_w is the angular extent of each groove.

9 Appendix II: Explicit Radiation Coefficients for Circular Inlets

In the near zone, there is no simple closed form expression for the radiated field due to an outgoing waveguide mode. However, it is possible to derive closed form expressions for far zone observations. From [16], the far zone field due to each mode is given by

$$\mathbf{E}_{rad} = \left[E_\theta \left\{ \begin{array}{c} \cos n\phi \\ -\sin n\phi \end{array} \right\} \mathbf{u}_\theta + E_\phi \left\{ \begin{array}{c} \sin n\phi \\ \cos n\phi \end{array} \right\} \mathbf{u}_\phi \right] \frac{\mathrm{e}^{-jkr}}{r} \tag{91}$$

$$E_\theta = E_{\theta k} + E_{\theta u} \tag{92}$$

$$E_\phi = E_{\phi k} + E_{\phi u} \tag{93}$$

where $E_{\theta k}, E_{\phi k}$ are associated with the contribution from the Kirchhoff integral and $E_{\theta u}, E_{\phi u}$ correspond to the contribution from the equivalent fringe rim current (Ufimtsef type). Explicit expressions of $E_{\theta k}, E_{\phi k}, E_{\theta u}, E_{\phi u}$ are as follows:

TM_{np} modes:

$$E_{\theta k} = j^n k N_{1,np}^{TM} \gamma_{1,np}^{TM} b \cdot \cdot \frac{\sin\theta}{2\left(\cos\psi_{1,np}^{TM} - \cos\theta\right)} J_n'\left(\gamma_{1,np}^{TM} b\right) J_n\left(kb\sin\theta\right) \tag{94}$$

$$E_{\phi k} = 0 \tag{95}$$

$$E_{\theta u} = j^n N_{1,np}^{TM} J_n'\left(\gamma_{1,np}^{TM} b\right) \frac{\cos\left(\theta/2\right) - \cos\left(\psi_{1,np}^{TM}/2\right)}{\cos\psi_{1,np}^{TM} - \cos\theta} \cdot \cdot \left[n^2 \beta_{1,np}^{TM} \sin\frac{\psi_{1,np}^{TM}}{2} \frac{\cot\theta}{kb} J_n\left(kb\sin\theta\right) + + k\gamma_{1,np}^{TM} b \sin\frac{\theta}{2} J_n''\left(kb\sin\theta\right)\right] \tag{96}$$

$$E_{\phi u} = -j^n N_{1,np}^{TM} n J_n'\left(\gamma_{1,np}^{TM} b\right) \frac{\cos\left(\theta/2\right) - \cos\left(\psi_{1,np}^{TM}/2\right)}{\cos\psi_{1,np}^{TM} - \cos\theta} \cdot \cdot \left\{\beta_{1,np}^{TM} \sin\frac{\psi_{1,np}^{TM}}{2} J_n'\left(kb\sin\theta\right) + + k\gamma_{1,np}^{TM} b \sin\frac{\theta}{2} \frac{\cot\theta}{kb} \left[J_n'\left(kb\sin\theta\right) - \frac{J_n\left(kb\sin\theta\right)}{kb\sin\theta}\right]\right\} \tag{97}$$

TE_{np} modes:

$$
\begin{aligned}
E_{\theta k} &= j^n k Z N_{1,np}^{TE} n \cdot \\
&\cdot \frac{1+\cos\theta\cos\psi_{1,np}^{TE}}{2\sin\theta} J_n\left(\gamma_{1,np}^{TE} b\right) J_n\left(kb\sin\theta\right) \qquad (98)\\
E_{\phi k} &= j^n k Z N_{1,np}^{TE} \gamma_{1,np}^{TE} b \cdot \\
&\cdot \frac{\sin\psi_{1,np}^{TE}}{2\left(\cos\psi_{1,np}^{TE}-\cos\theta\right)} J_n\left(\gamma_{1,np}^{TE} b\right) J_n'\left(kb\sin\theta\right) \qquad (99)\\
E_{\theta u} &= j^n Z N_{1,np}^{TE} n J_n\left(\gamma_{1,np}^{TE} b\right) \frac{\cos\left(\theta/2\right)-\cos\left(\psi_{1,np}^{TE}/2\right)}{\cos\psi_{1,np}^{TE}-\cos\theta} \cdot \\
&\cdot \left\{ \beta_{1,np}^{TE} \sin\frac{\theta}{2} J_n''\left(kb\sin\theta\right) - \right. \\
&- \left. k\gamma_{1,np}^{TE} b \sin\frac{\psi_{1,np}^{TE}}{2} \frac{\cot\theta}{kb} J_n\left(kb\sin\theta\right) \right\} \qquad (100)\\
E_{\phi u} &= j^n Z N_{1,np}^{TE} J_n\left(\gamma_{1,np}^{TE} b\right) \frac{\cos\left(\theta/2\right)-\cos\left(\psi_{1,np}^{TE}/2\right)}{\cos\psi_{1,np}^{TE}-\cos\theta} \cdot \\
&\cdot \left\{ k\gamma_{1,np}^{TE} b \sin\frac{\psi_{1,np}^{TE}}{2} J_n'\left(kb\sin\theta\right) - \right. \\
&- \left. n^2 \beta_{1,np}^{TE} \sin\frac{\theta}{2} \frac{\cot\theta}{kb} \left[J_n'\left(kb\sin\theta\right) - \frac{J_n\left(kb\sin\theta\right)}{kb\sin\theta} \right] \right\} \qquad (101)
\end{aligned}
$$

where, by definition

$$
\cos\psi_{1,np}^{TM,TE} \equiv \frac{\beta_{1,np}^{TM,TE}}{k} \qquad (102)
$$

10 List of Figures

cm, for an incidence angle of $\theta_i = 0^o$. a) ρ component b) ϕ component

Figure 12. Calculated (solid line) and measured (dotted line) data for the straight blades model at 6 GHz (the model is described in Section 5).

Figure 13. Tangential fields at both sides of the interface for the geometry corresponding to Fig. 12 (ϕ polarization). The fields are plotted at $\rho = 10$ cm, for an incidence angle of $\theta_i = 0^o$. a) ρ component b) ϕ component

Figure 14. Calculated (solid line) and measured (dotted line) data for the straight blades model at 8 GHz (the model is described in Section 5).

Figure 15. Tangential fields at both sides of the interface for the geometry corresponding to Fig. 14 (θ polarization). The fields are plotted at $\rho = 11.25$ cm, for an incidence angle of $\theta_i = 0^o$. a) ρ component b) ϕ component

Figure 16. Tangential fields at both sides of the interface for the geometry corresponding to Fig. 14 (θ polarization). The fields are plotted at $\rho = 11.25$ cm, for an incidence angle of $\theta_i = 40^o$. a) ρ component b) ϕ component

Figure 17. Calculated (solid line) and measured (dotted line) data for the straight blades model at 10 GHz (the model is described in Section 5).

Figure 18. Calculated (solid line) and measured (dotted line) data for the curved blades model at 4 GHz (the model is described in Section 5).

Figure 19. Tangential fields at both sides of the interface for the geometry corresponding to Fig. 18 (ϕ polarization). The fields are plotted at $\rho = 11.25$ cm, for an incidence angle of $\theta_i = 0^o$. a) ρ component b) ϕ component

Figure 20. Tangential fields at both sides of the interface for the geometry corresponding to Fig. 18 (ϕ polarization). The fields are plotted at $\rho = 11.25$ cm, for an incidence angle of $\theta_i = 40^o$. a) ρ component b) ϕ component

Figure 21. Calculated (solid line) and measured (dotted line) data for the curved blades model at 6 GHz (the model is described in Section 5).

References

[1] T.W Johnson and D. L. Moffat, "Electromagnetic scattering by open circular waveguides", Technical Report 710816-9, The Ohio State University, ElectroScience Laboratory, Columbus OH, December 1980.

[2] Ching-Chao Huang, "Ray analysis of EM backscatter from a cavity configuration", Ph.D. Dissertation, The Ohio State University, ElectroScience Laboratory, Columbus OH, 1982.

[3] H. Ling, R.C. Chou and S.W. Lee, "Shooting and Bouncing Rays: Calculating the RCS of an arbitrarily shaped cavity," *IEEE Trans. Antennas and Propagation*, vol. 37, no 2, pp. 194-205, February 1989.

[4] D. J. Andersh, M. Hazlett, S. W. Lee, D. D. Reeves, D. P. Sullivan and Y. Chu, "XPATCH: A high-frequency electromagnetic scattering prediction code and environment for complex three-dimensional objects", *IEEE Antennas and Propagation Magazine*, vol. 36, no. 1, pp. 65-69, February 1994

[5] R. J. Burkholder and P. H. Pathak, "High frequency asymptotic methods for analyzing the EM scattering by open-ended waveguide cavities", Technical Report 719630-3, The Ohio State University, ElectroScience Laboratory, Columbus OH, September 1989.

[6] R. F. Harrington, *Time-harmonic electromagnetic fields*, Mc Graw-Hill, 1961.

[7] H. T. Anastassiu, D. C. Ross and J. L. Volakis, "Progress report on the analysis of jet engine inlets", Technical Report 030395-5-T, The University of Michigan, EECS Radiation Laboratory, Ann Arbor MI, July 1994.

[8] H. T. Anastassiu and J. L. Volakis, "The Mode Matching technique for electromagnetic scattering by inlets with complex terminations", Technical Report 030395-3-T, The University of Michigan, EECS Radiation Laboratory, Ann Arbor MI, October 1993.

[9] D. C. Ross, J. L. Volakis and H. T. Anastassiu, "Hybrid Finite Element - Modal analysis of jet engine inlet scattering", accepted for publication in *IEEE Trans. Antennas and Propagation*

[10] R. Mittra and S.W. Lee, *Analytical Techniques in the Theory of Guided Waves*, Mac Millan, 1971.

[11] M. Leroy, "On the convergence of numerical results in mode analysis", *I.E.E.E. Trans. Antennas Propagation*, vol. AP-31, pp. 655-659, July 1983.

[12] R. J. Burkholder, The Ohio State University, ElectroScience Laboratory (personal communication).

[13] P. P. Silvester and R. L. Ferrari, *Finite Elements for electrical engineers*, Cambridge, 1986.

[14] G. Reiter, "Generalized Telegraphist's Equation for waveguides of varying cross-section", *Proc. I.E.E.* vol. 106B, suppl. 13, pp. 54-57, 1959.

[15] Gilbert Strang, *Linear algebra and its applications*, HBJ, Third Edition, 1988.

[16] P. H. Pathak, C. W. Chuang, M. C. Liang, "Inlet modeling studies", Technical Report 717674-1, The Ohio State University, ElectroScience Laboratory, Columbus OH, October 1980.

[17] N. Marcuvitz, *Waveguide Handbook*, Krieger, IEE Press, P. Peregrinus Ltd., 1986, pp. 72-77.

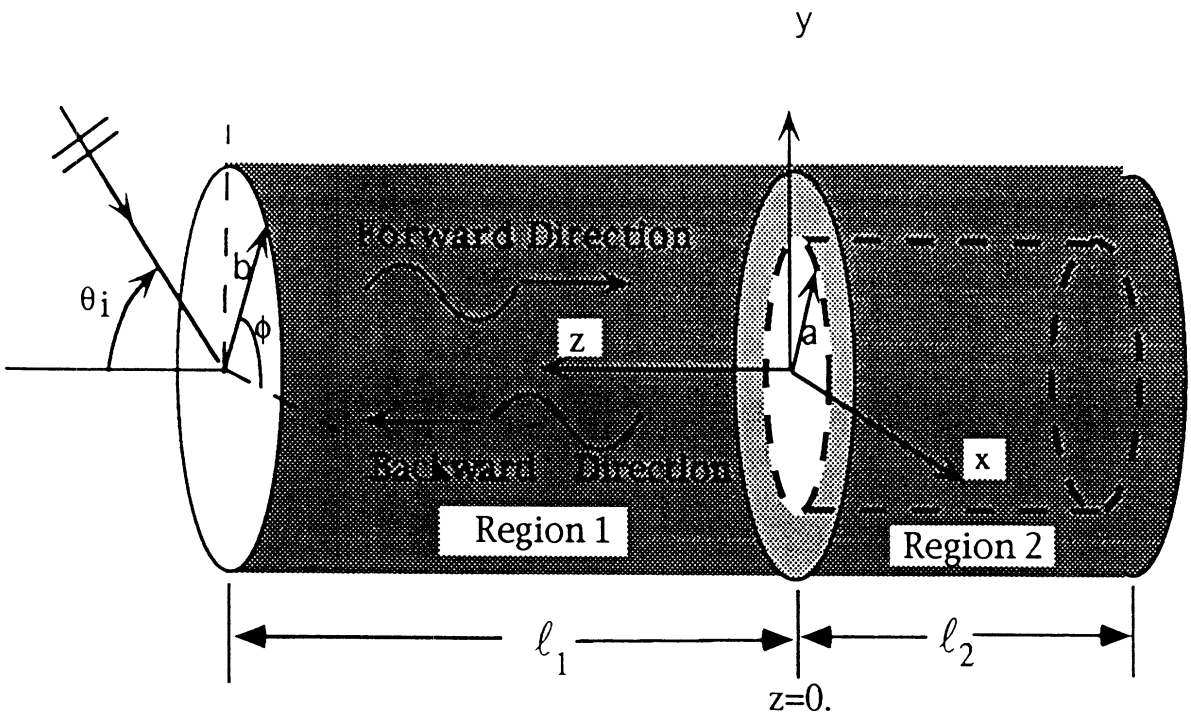

Figure 1. Cylindrical inlet terminated by a cylindrical hub.

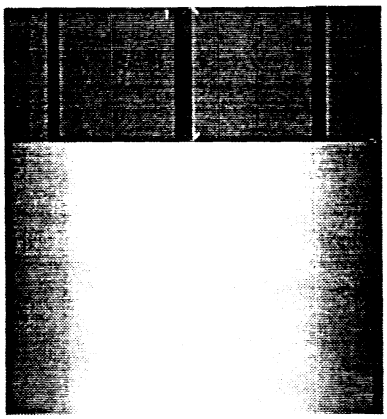

Side view

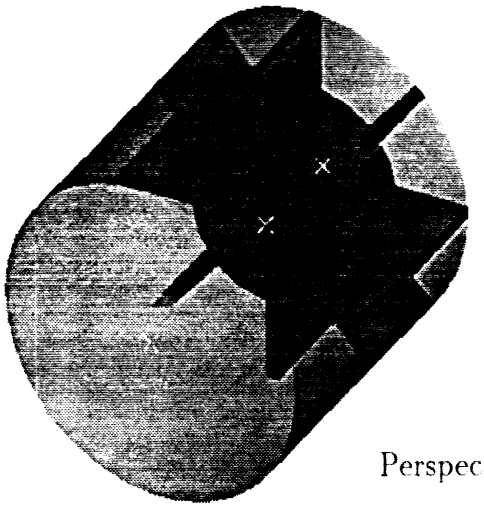

Perspective view

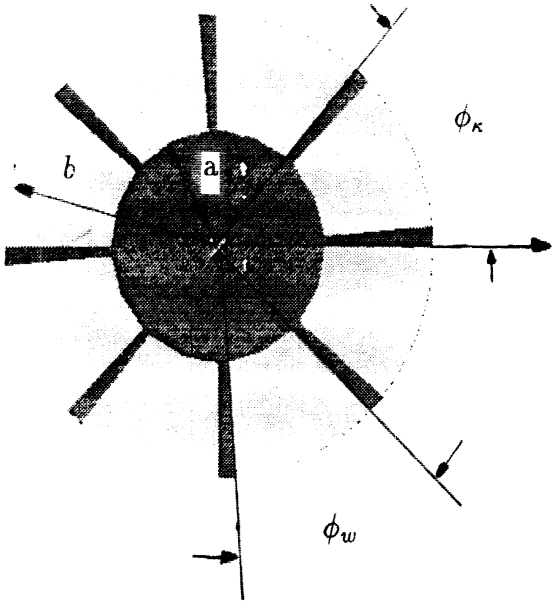

Front view

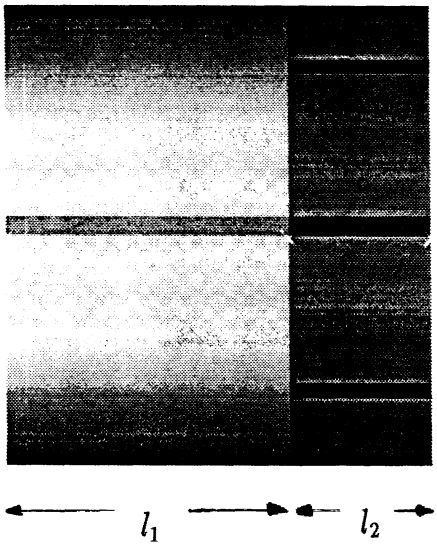

Side view

Figure 2. Cylindrical inlet terminated by an array of straight blades.

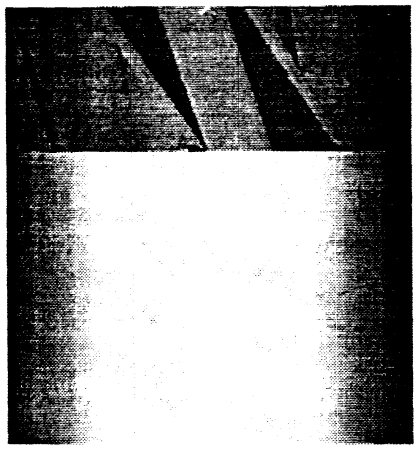

Side view

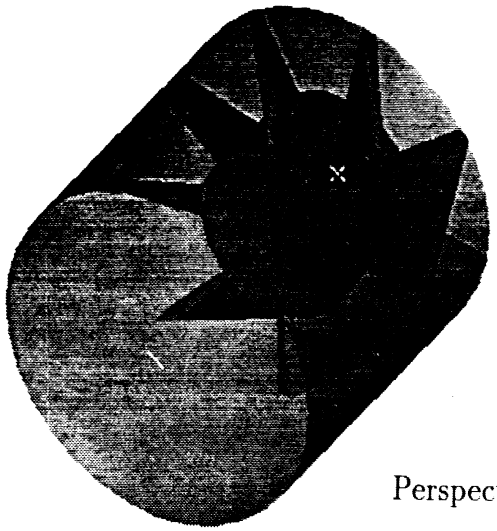

Perspective view

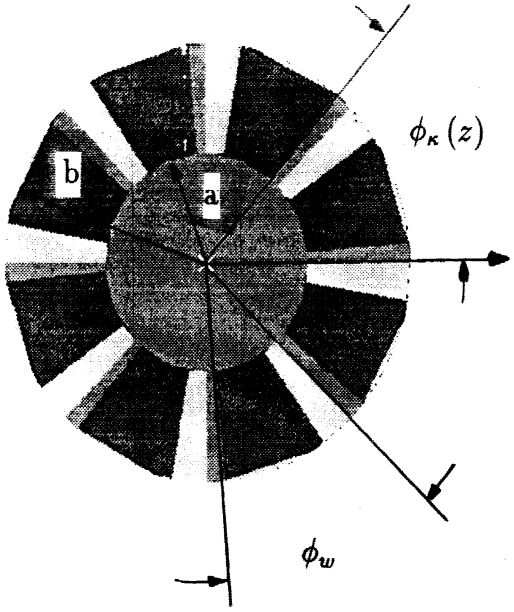

Front view

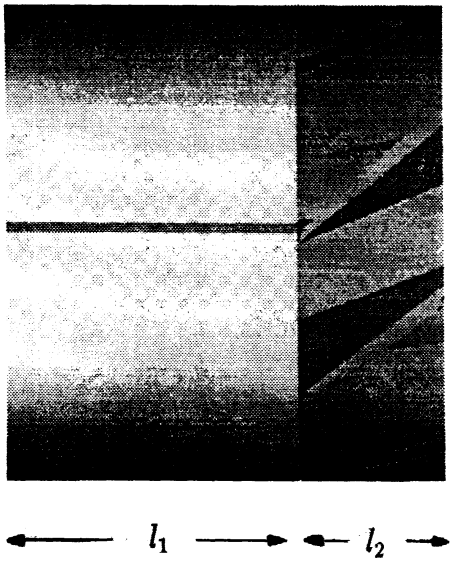

Side view

Figure 3. Cylindrical inlet terminated by an array of curved blades.

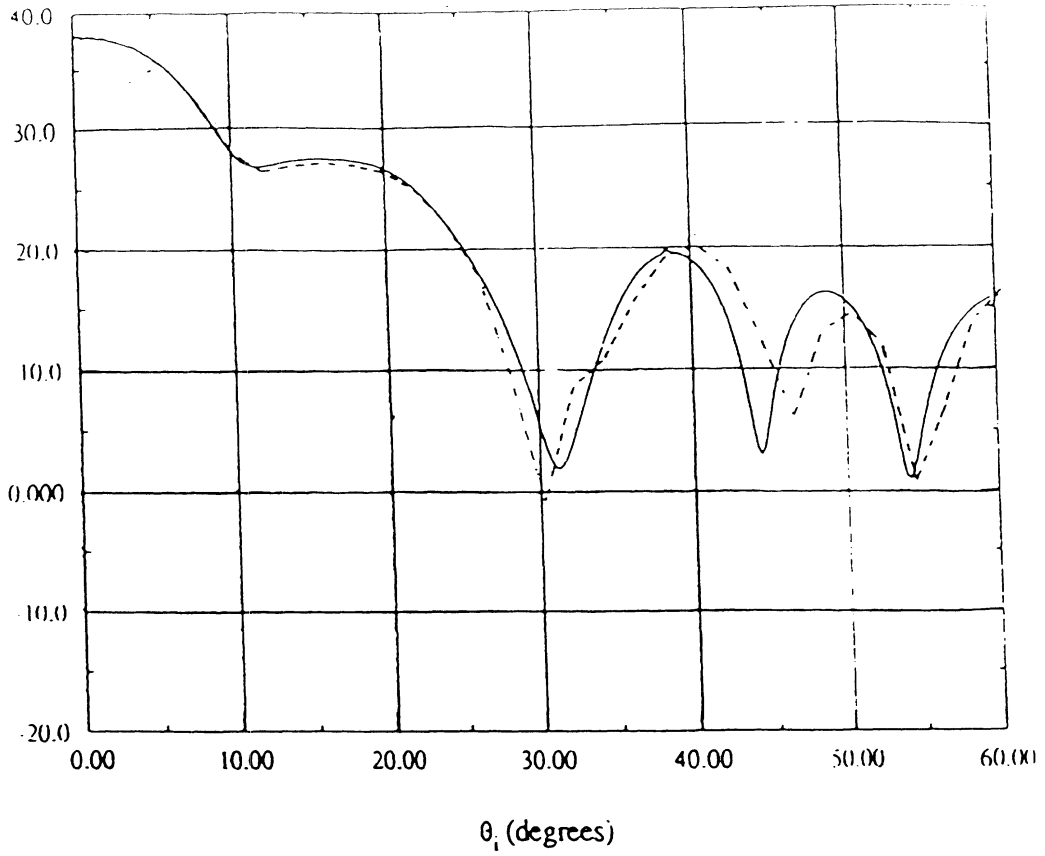

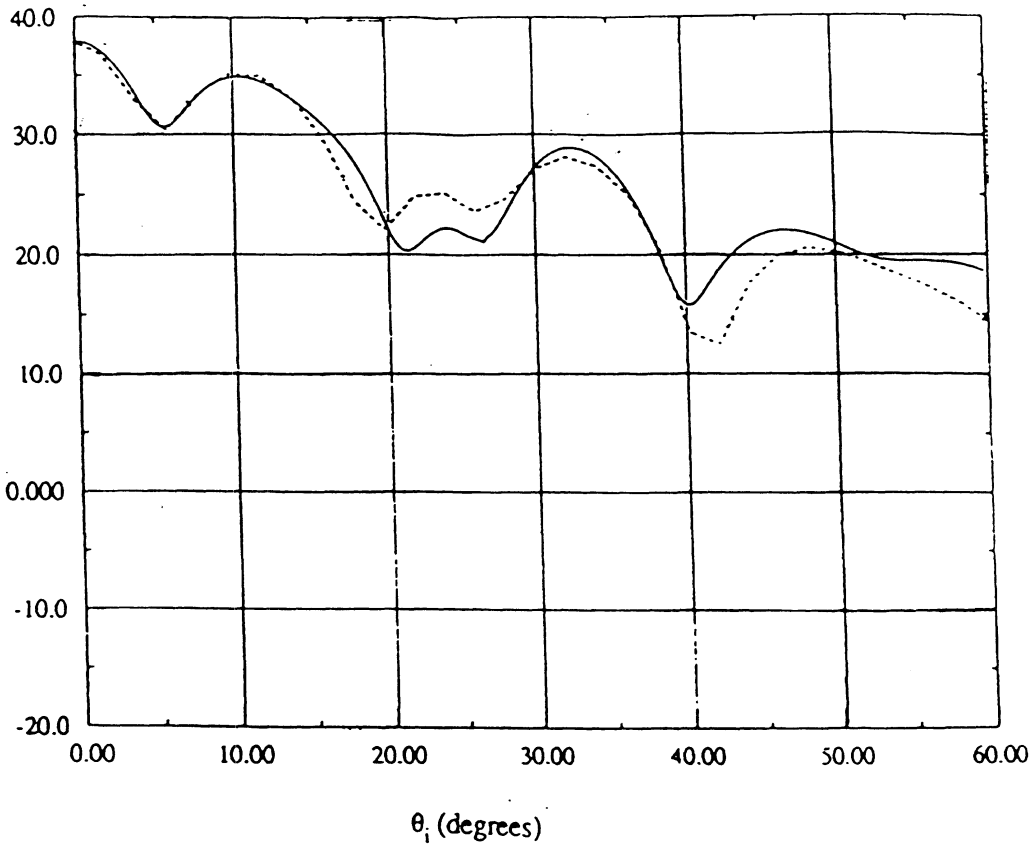

Figure 4. RCS (dB/λ^2) pattern calculated by the Mode Matching Technique (solid line) and the Hybrid Modal Technique (dashed line) for the geometry shown in Fig. 1. The specific dimensions for this calculation are: $a = 1.5\lambda, b = 3\lambda, l_1 = 16.595\lambda, l_2 = \lambda$ a) ϕ polarization, b) θ polarization.

Modes 1-10: $TM_{0,1}$ to $TM_{0,10}$ ($\propto \cos n\phi$)
Modes 11-20: $TM_{1,1}$ to $TM_{1,10}$ ($\propto \cos n\phi$)
Modes 21-30: $TM_{2,1}$ to $TM_{2,10}$ ($\propto \cos n\phi$)
Modes 31-40: $TE_{0,1}$ to $TE_{0,10}$ ($\propto \sin n\phi$)
Modes 41-50: $TE_{1,1}$ to $TE_{1,10}$ ($\propto \sin n\phi$)
Modes 51-60: $TE_{2,1}$ to $TE_{2,10}$ ($\propto \sin n\phi$)

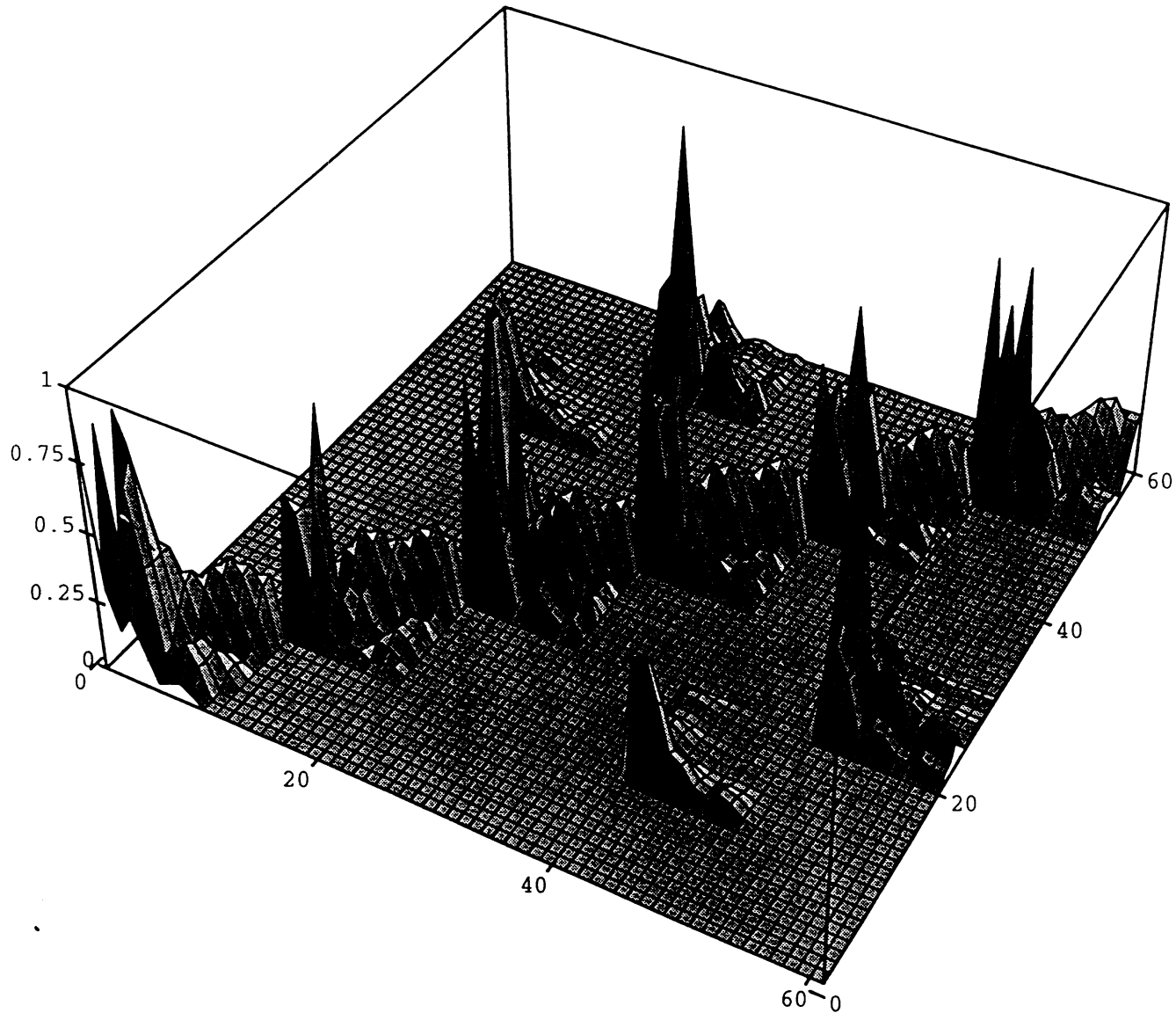

Figure 5: Amplitudes of the elements of the generalized scattering matrix calculated by Mode Matching for a hub termination with $a = 0.503\lambda, b = 1.66\lambda, l_1 = 16.595\lambda, l_2 = 0.335\lambda$

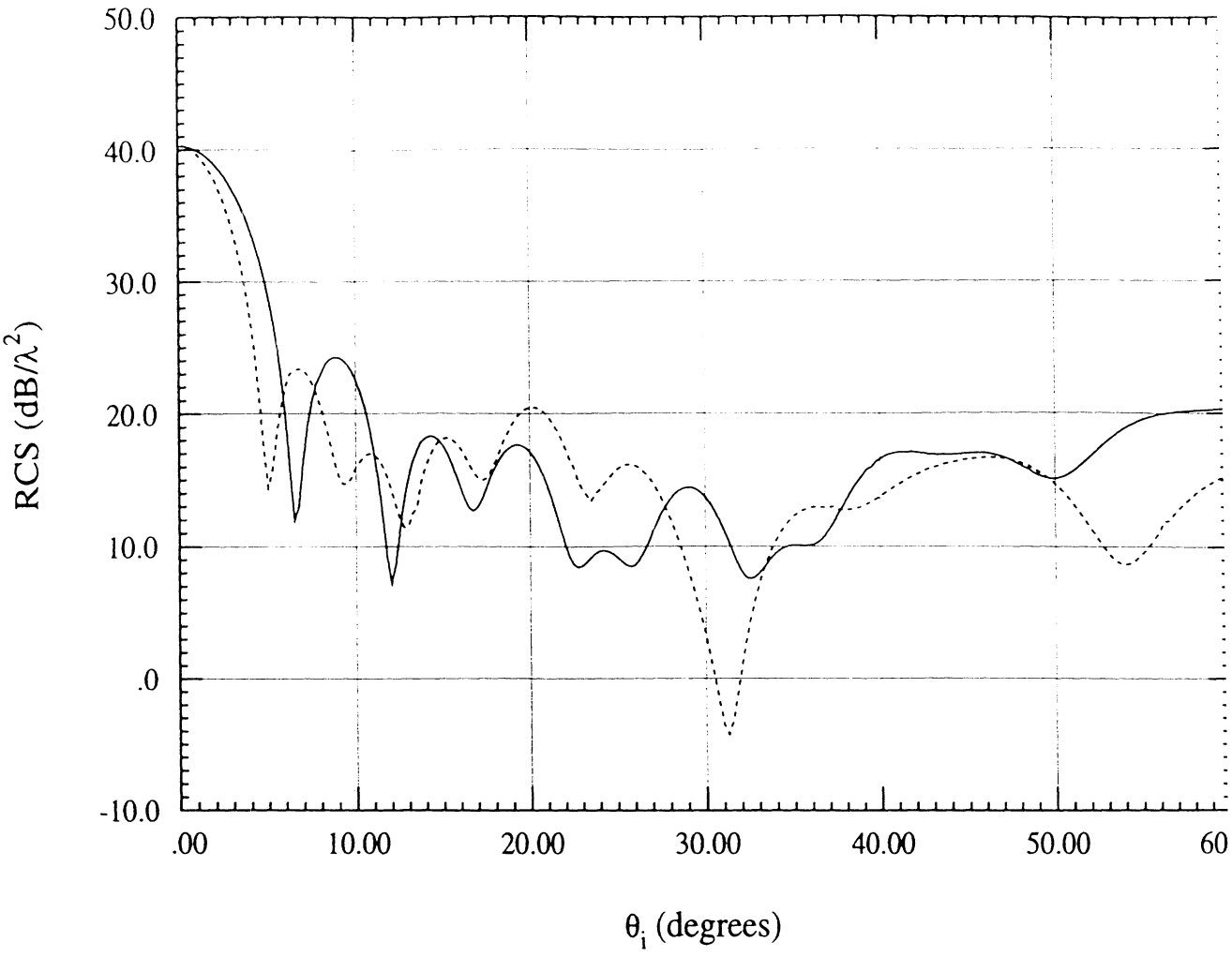

Figure 6. RCS (dB/λ^2) pattern calculated by the Mode Matching Technique for the geometry shown in Fig. 2. The dimensions for this calculation are: $a = 2.5\lambda, b = 3.5\lambda, l_1 = \lambda, l_2 = \lambda, 4$ blades, $\phi_w = 45°, \phi_1 = 0°$ (Solid line: ϕ polarization. Dashed line: θ polarization).

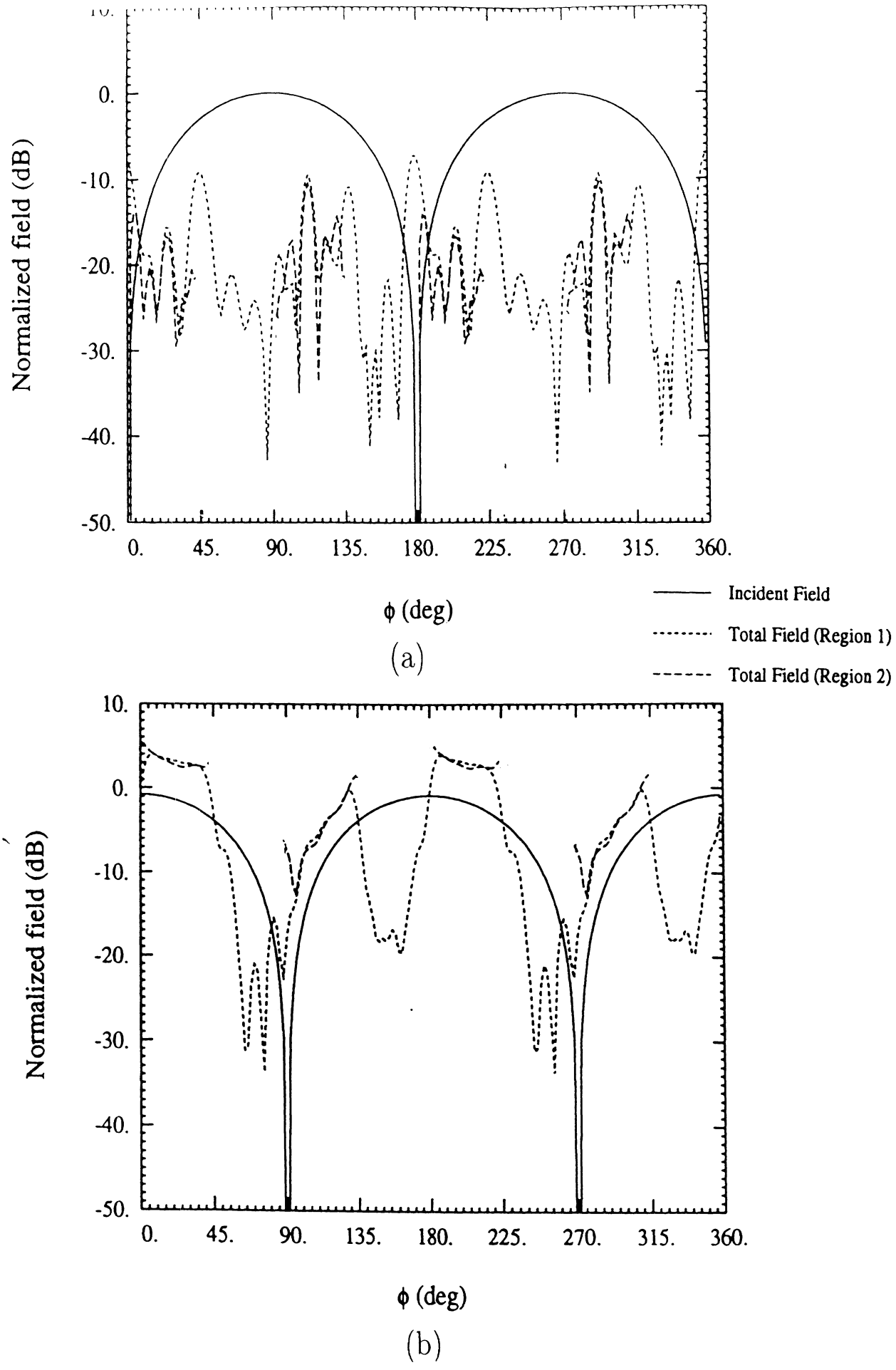

Figure 7. Tangential fields at both sides of the interface for the geometry corresponding to Fig. 6 (ϕ polarization). The fields are plotted at $\rho = 3\lambda$, for an incidence angle of $\theta_i = 0°$. a) ρ component b) ϕ component

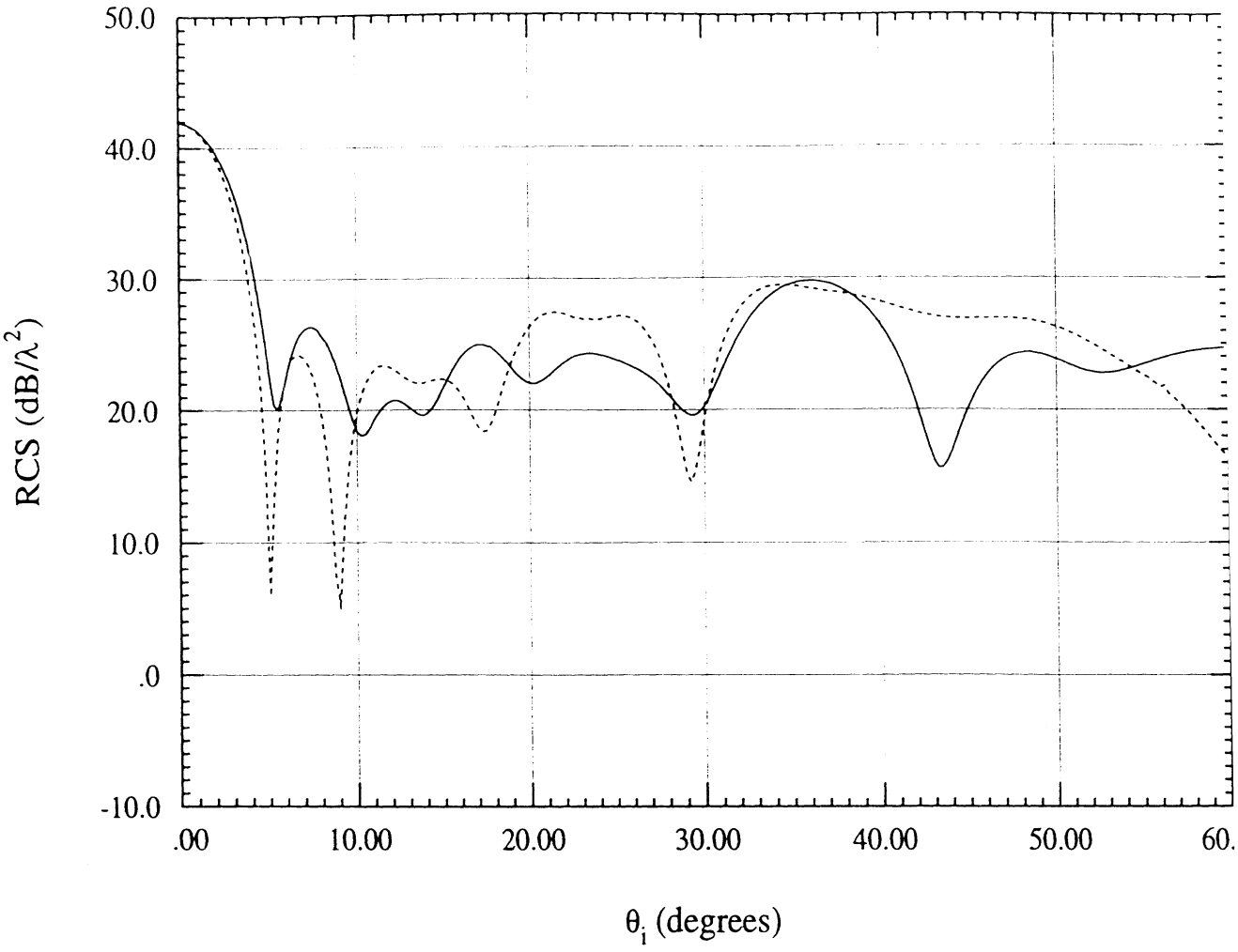

Figure 8. RCS (dB/λ^2) pattern calculated by the Mode Matching Technique for the geometry shown in Fig. 3. The dimensions for this calculation are: $a = 2.5\lambda, b = 3.5\lambda, l_1 = \lambda, l_2 = \lambda, 4$ blades, $\phi_w = 45^o, \phi_1(0) = 0^o, F'(z) = 30^o/\lambda$ (Solid line: ϕ polarization. Dashed line: θ polarization).

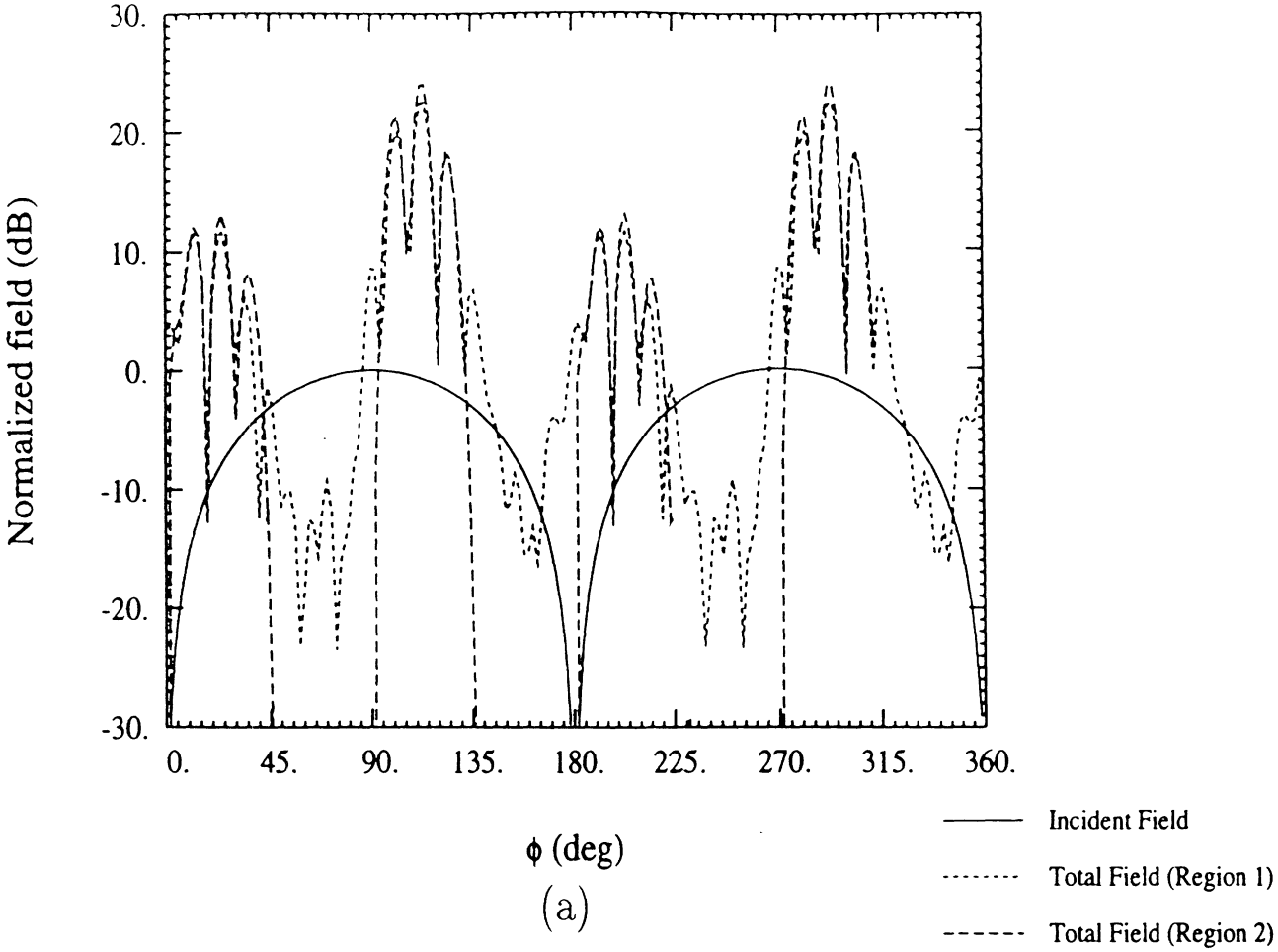

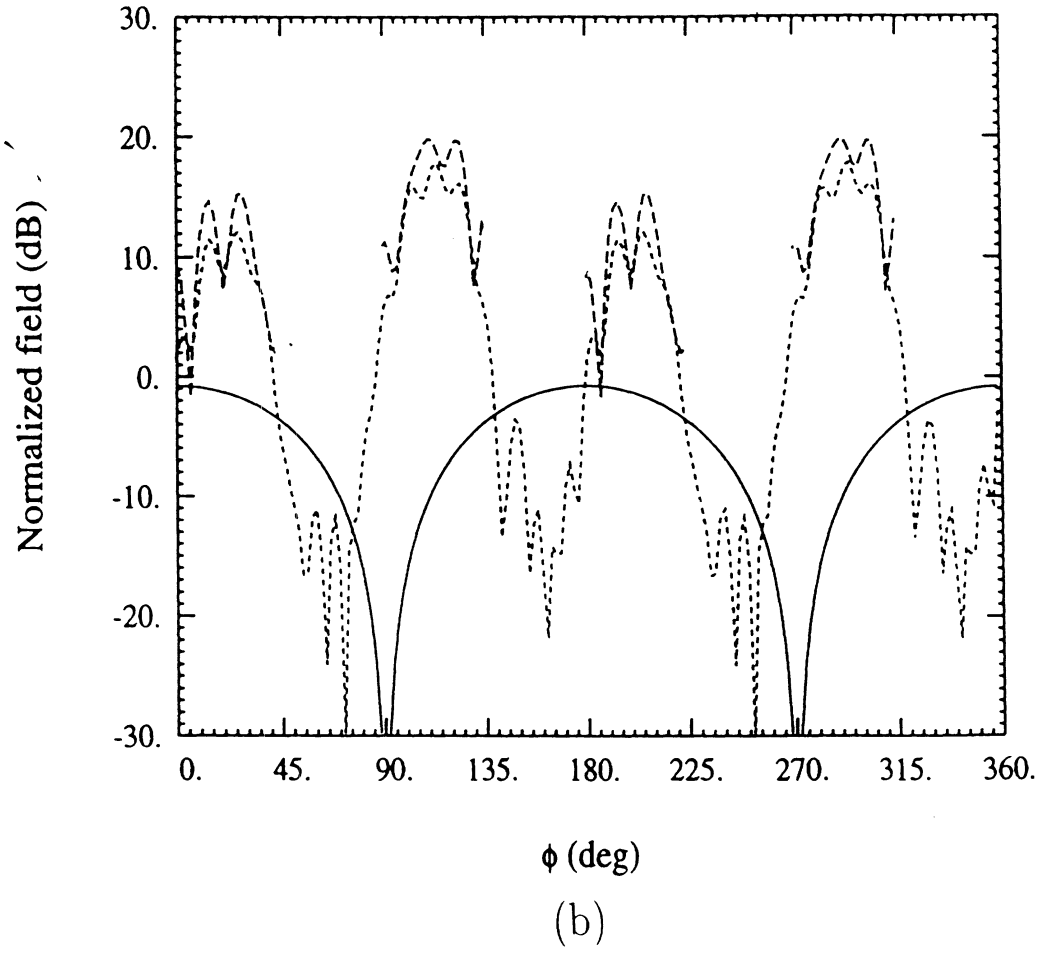

Figure 9. Tangential fields at both sides of the interface for the geometry corresponding to Fig. 8 (ϕ polarization). The fields are plotted at $\rho = 3\lambda$, for an incidence angle of $\theta_i = 0°$. a) ρ component b) ϕ component

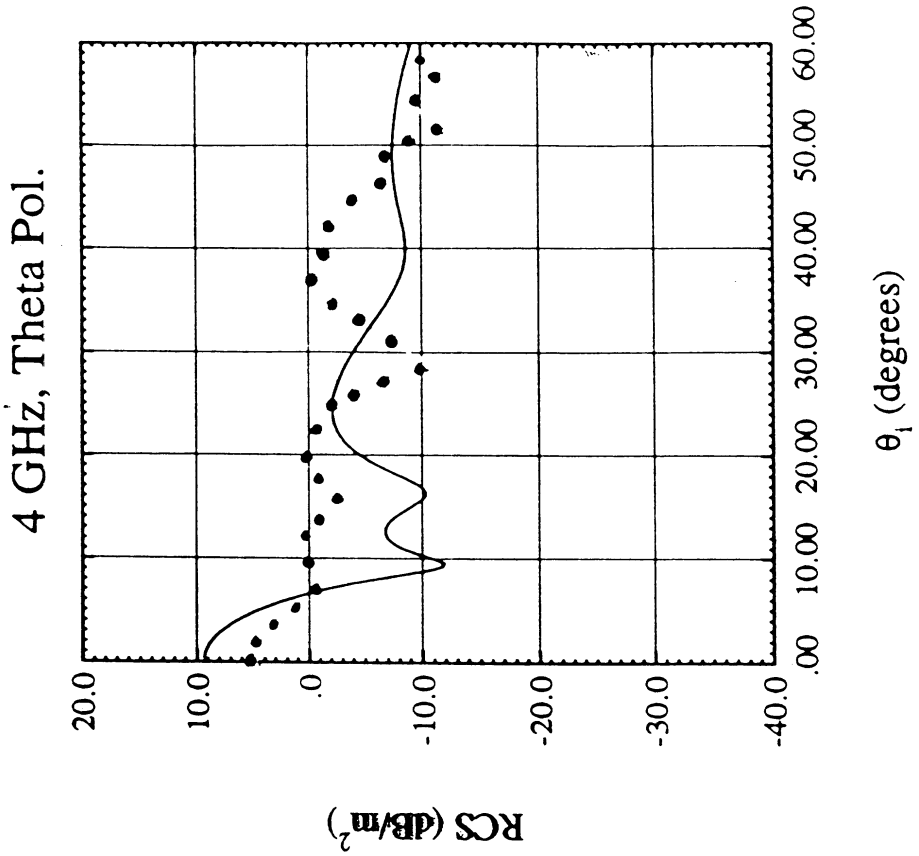

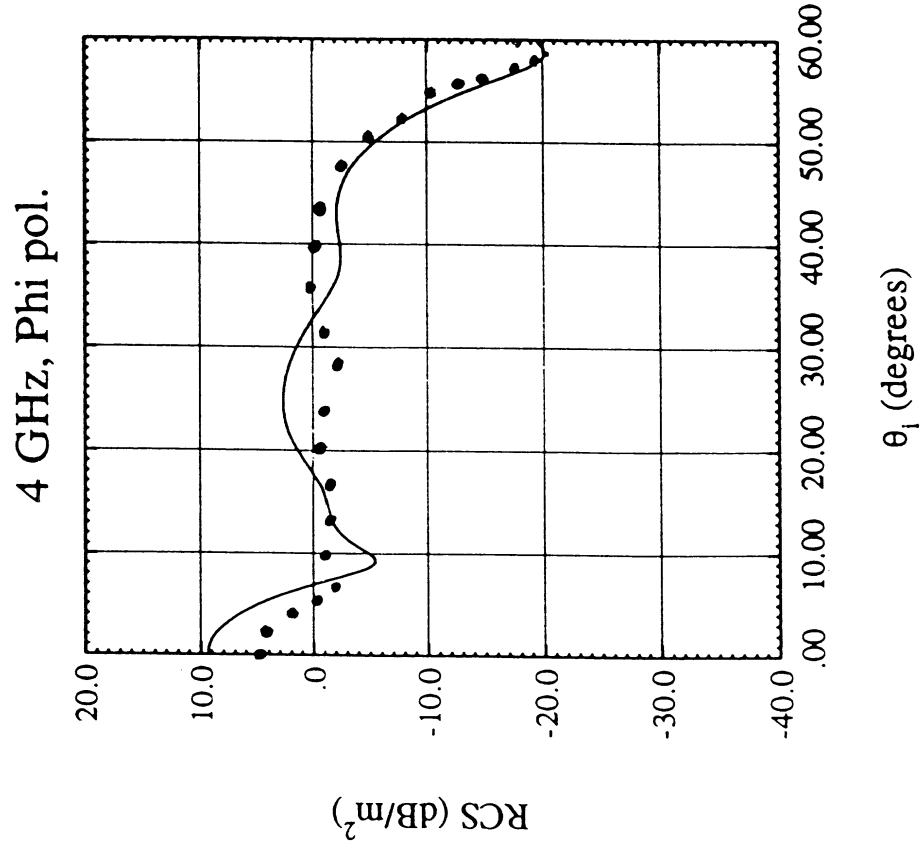

Figure 10. Calculated (solid line) and measured (dotted line) data for the straight blades model at 4 GHz (the model is described in Section 5).

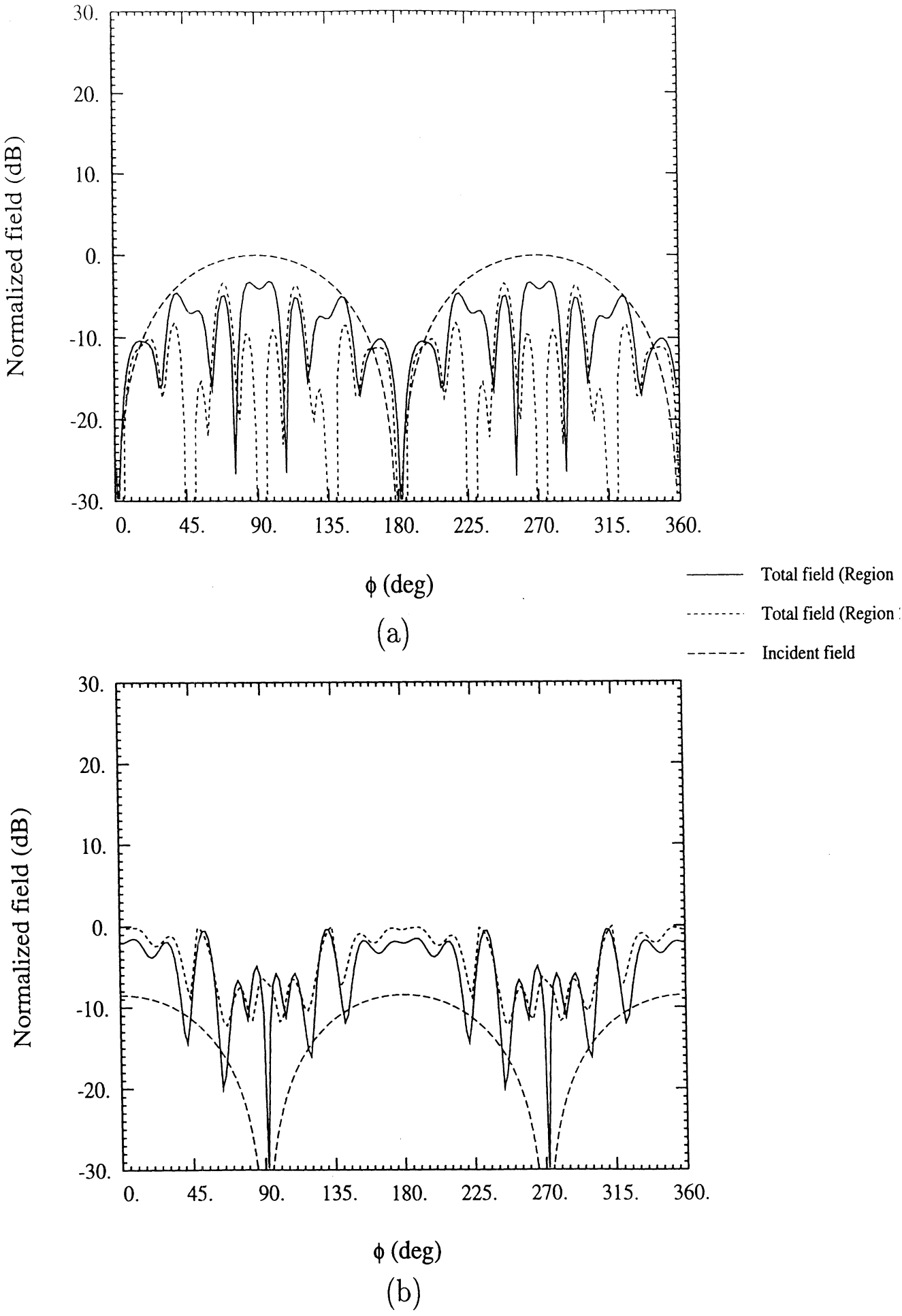

Figure 11. Tangential fields at both sides of the interface for the geometry corresponding to Fig. 10 (ϕ polarization). The fields are plotted at $\rho = 11.25$ cm, for an incidence angle of $\theta_i = 0^o$. a) ρ component b) ϕ component

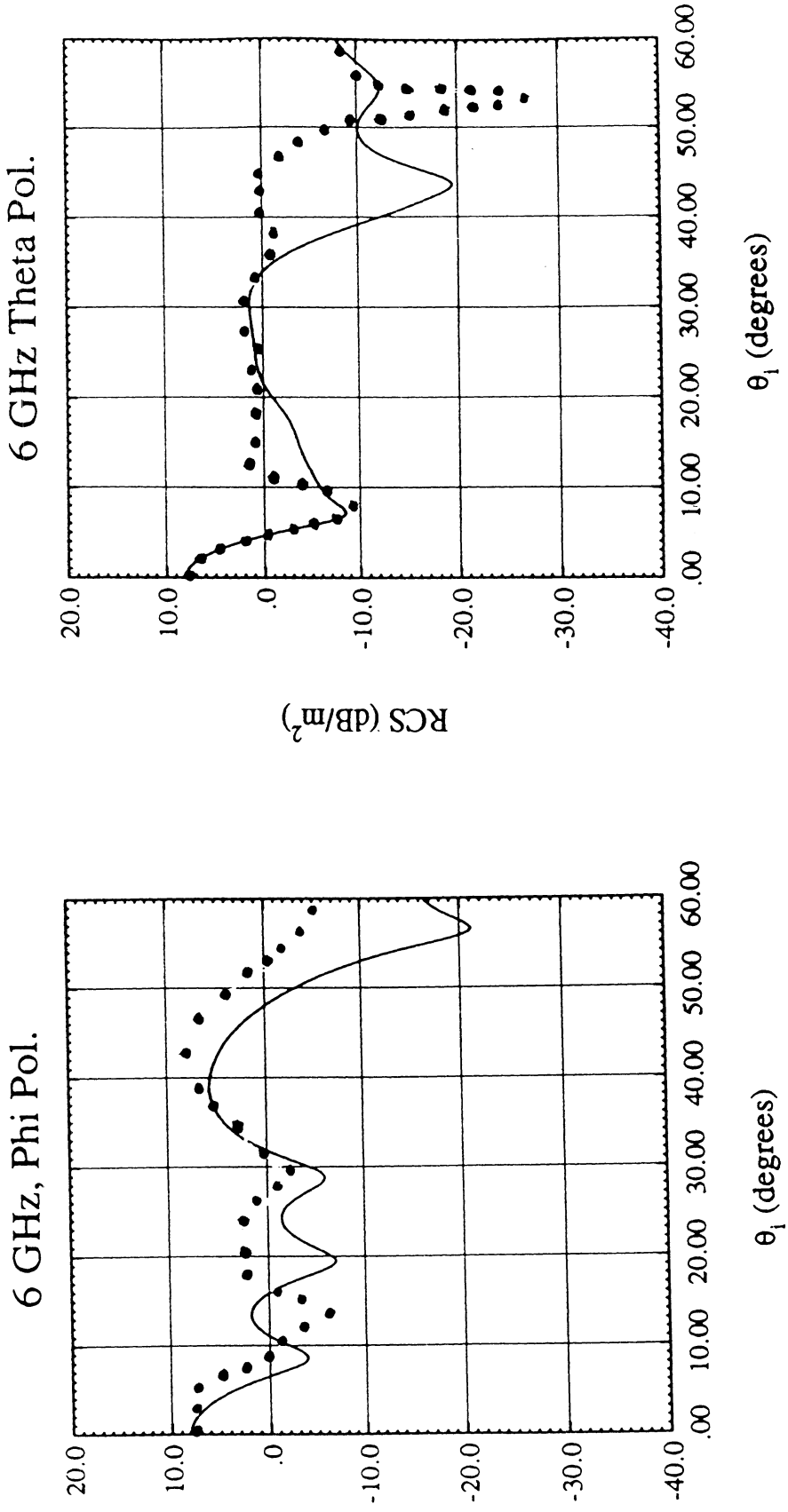

Figure 12. Calculated (solid line) and measured (dotted line) data for the straight blades model at 6 GHz (the model is described in Section 5).

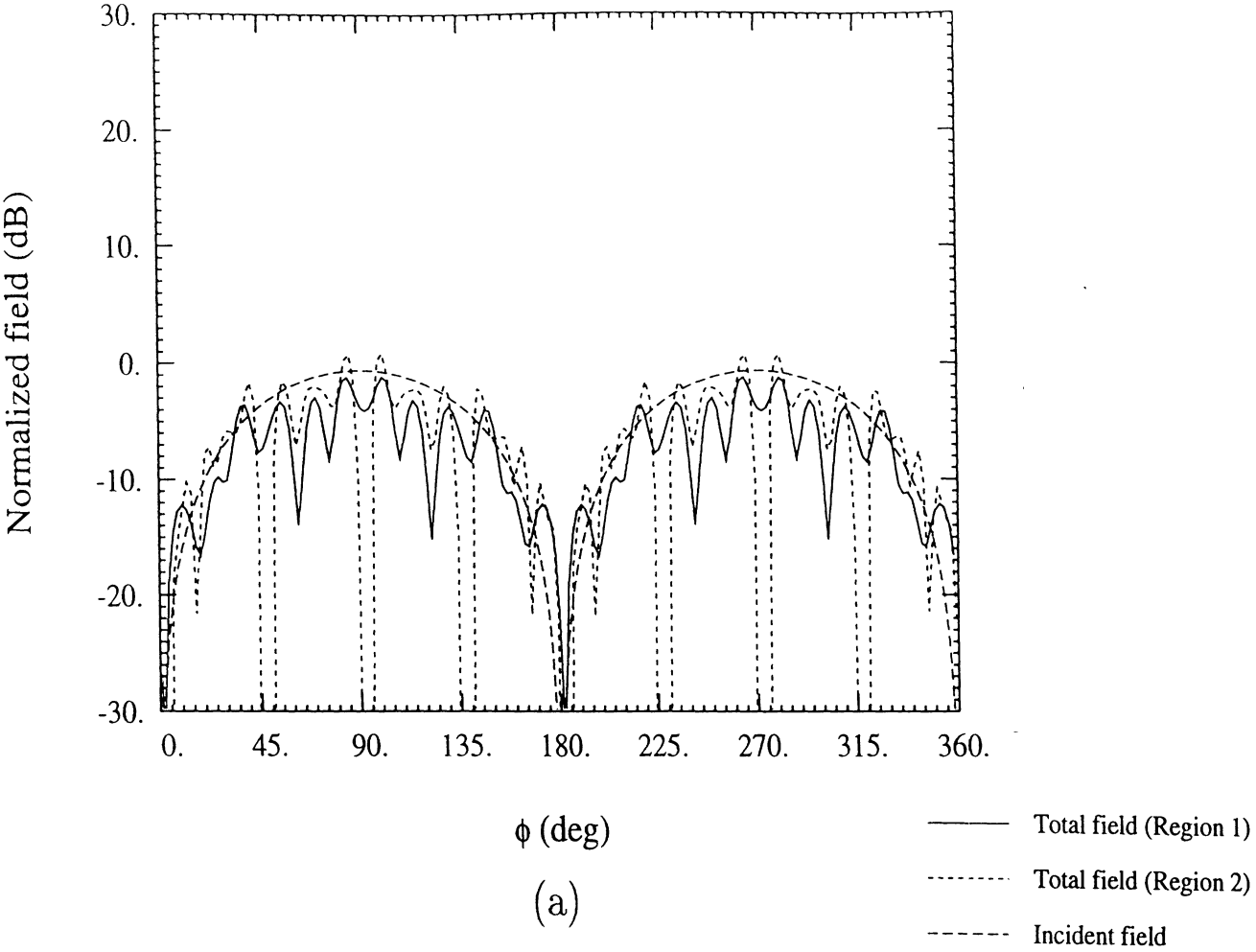

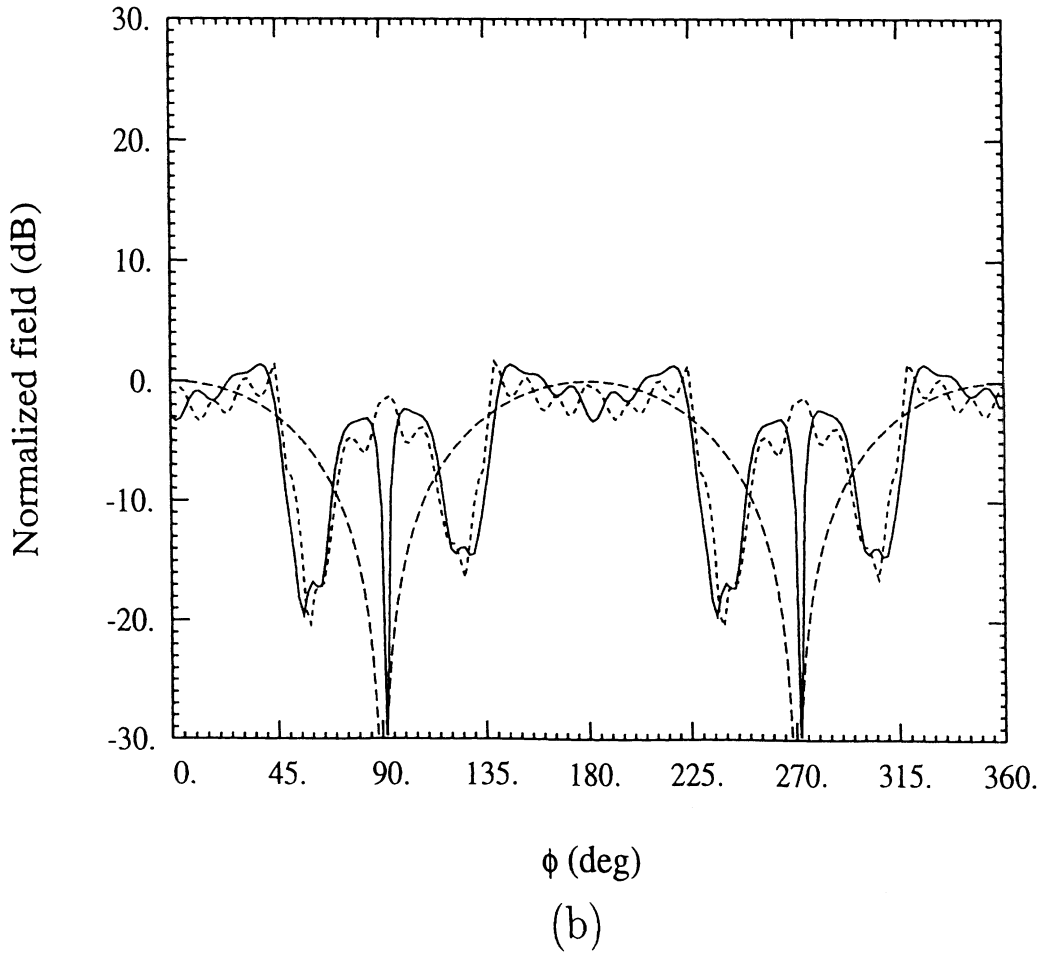

Figure 13. Tangential fields at both sides of the interface for the geometry corresponding to Fig. 12 (ϕ polarization). The fields are plotted at $\rho = 10$ cm for an incidence angle of $\theta_i = 0°$. a) ρ component b) ϕ component

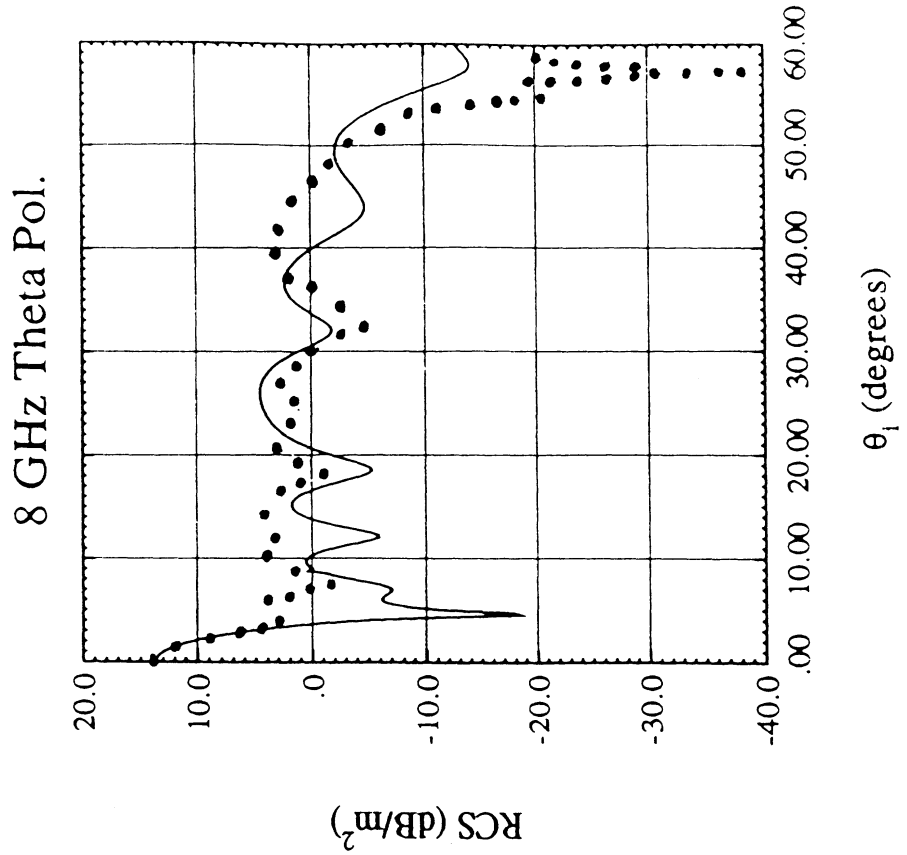

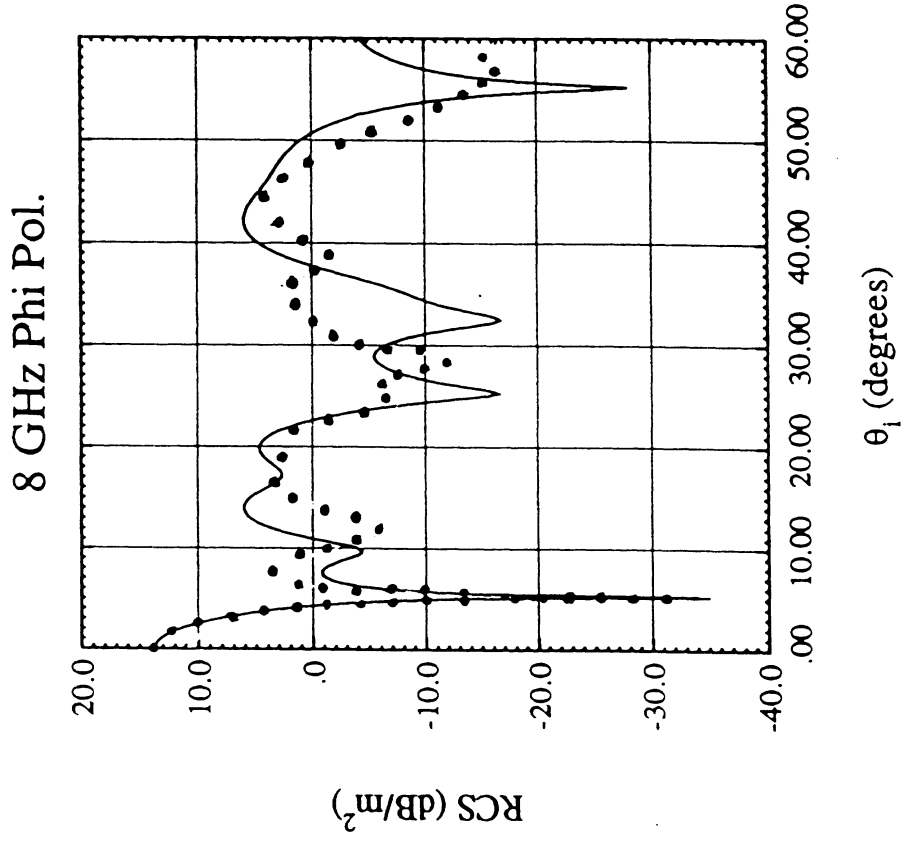

Figure 14. Calculated (solid line) and measured (dotted line) data for the straight blades model at 8 GHz (the model is described in Section 5).

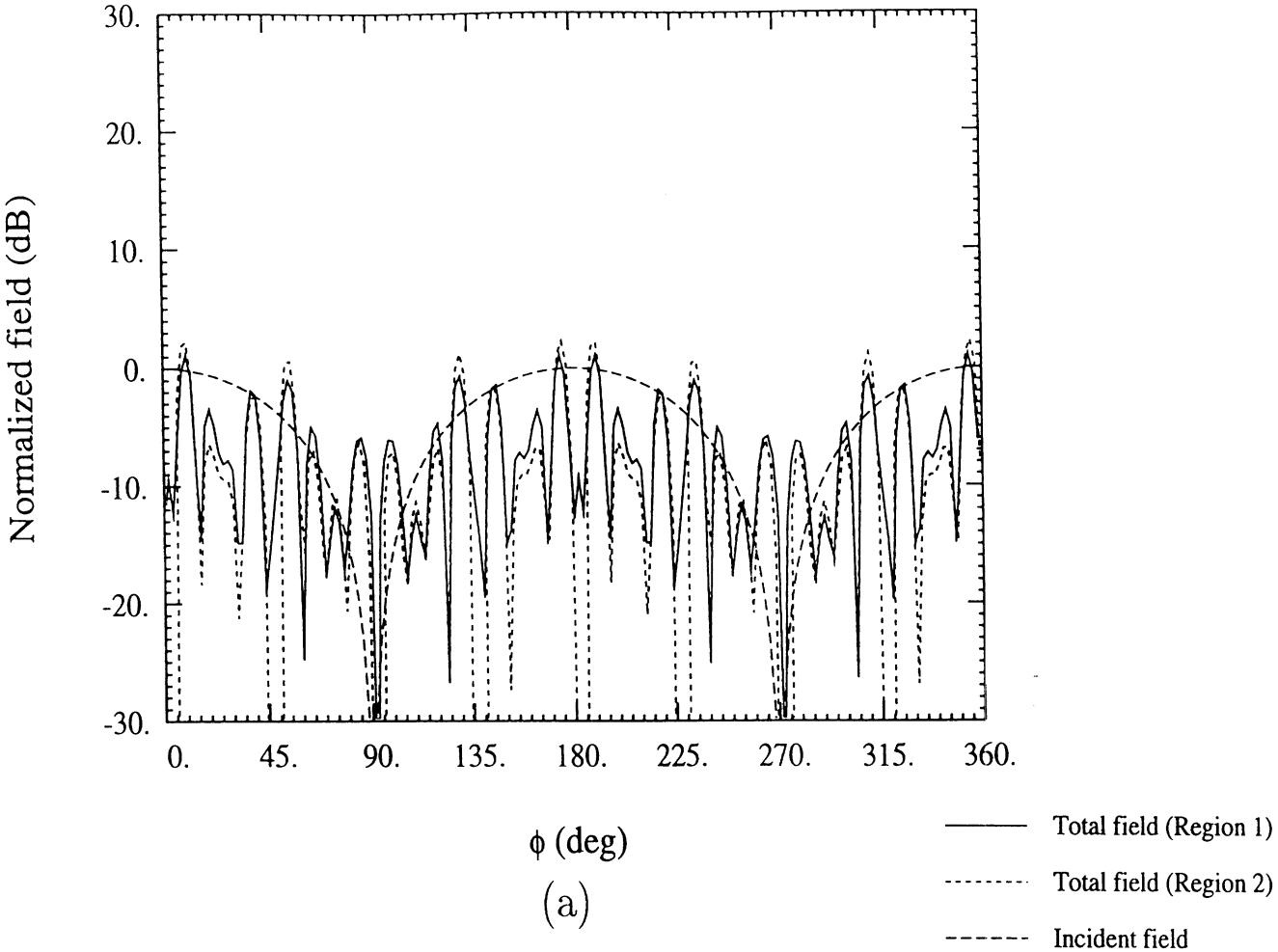

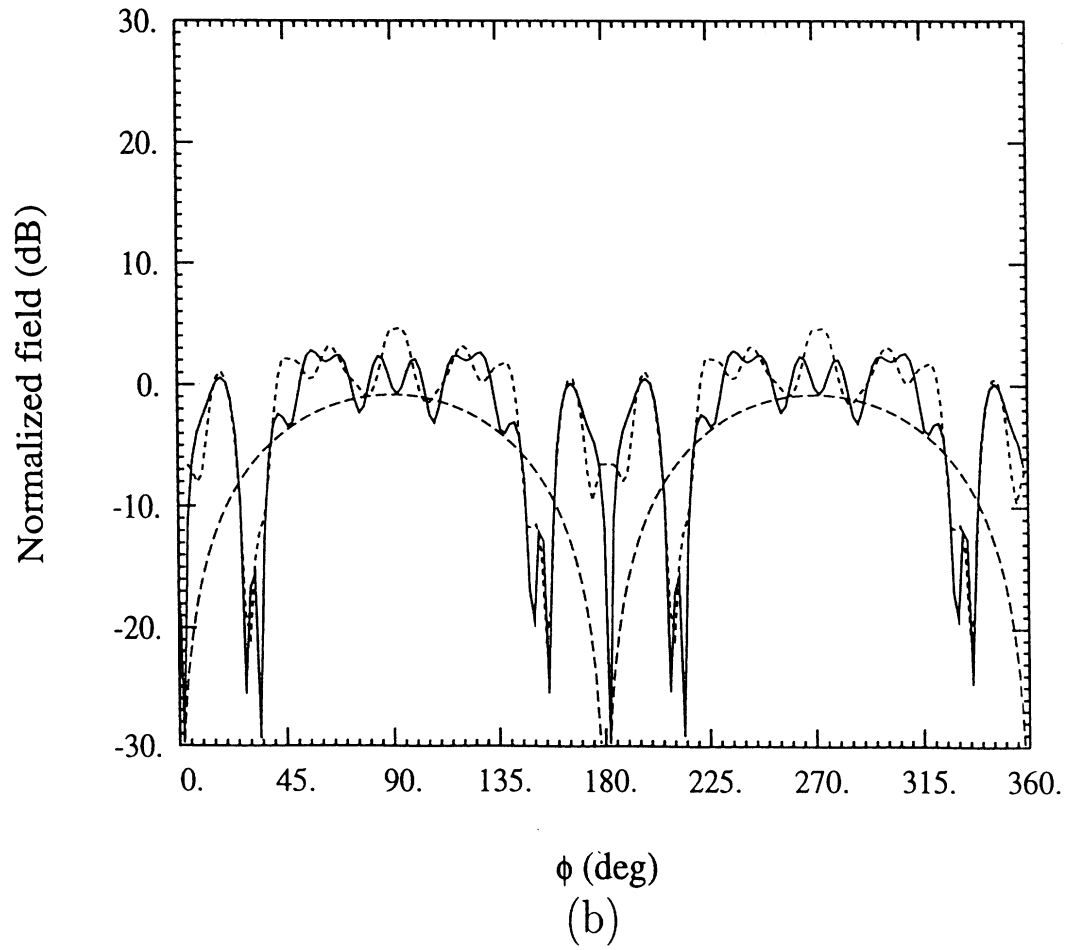

Figure 15. Tangential fields at both sides of the interface for the geometry corresponding to Fig. 14 (θ polarization). The fields are plotted at $\rho = 11.25$ cm. for an incidence angle of $\theta_i = 0°$. a) ρ component b) ϕ component

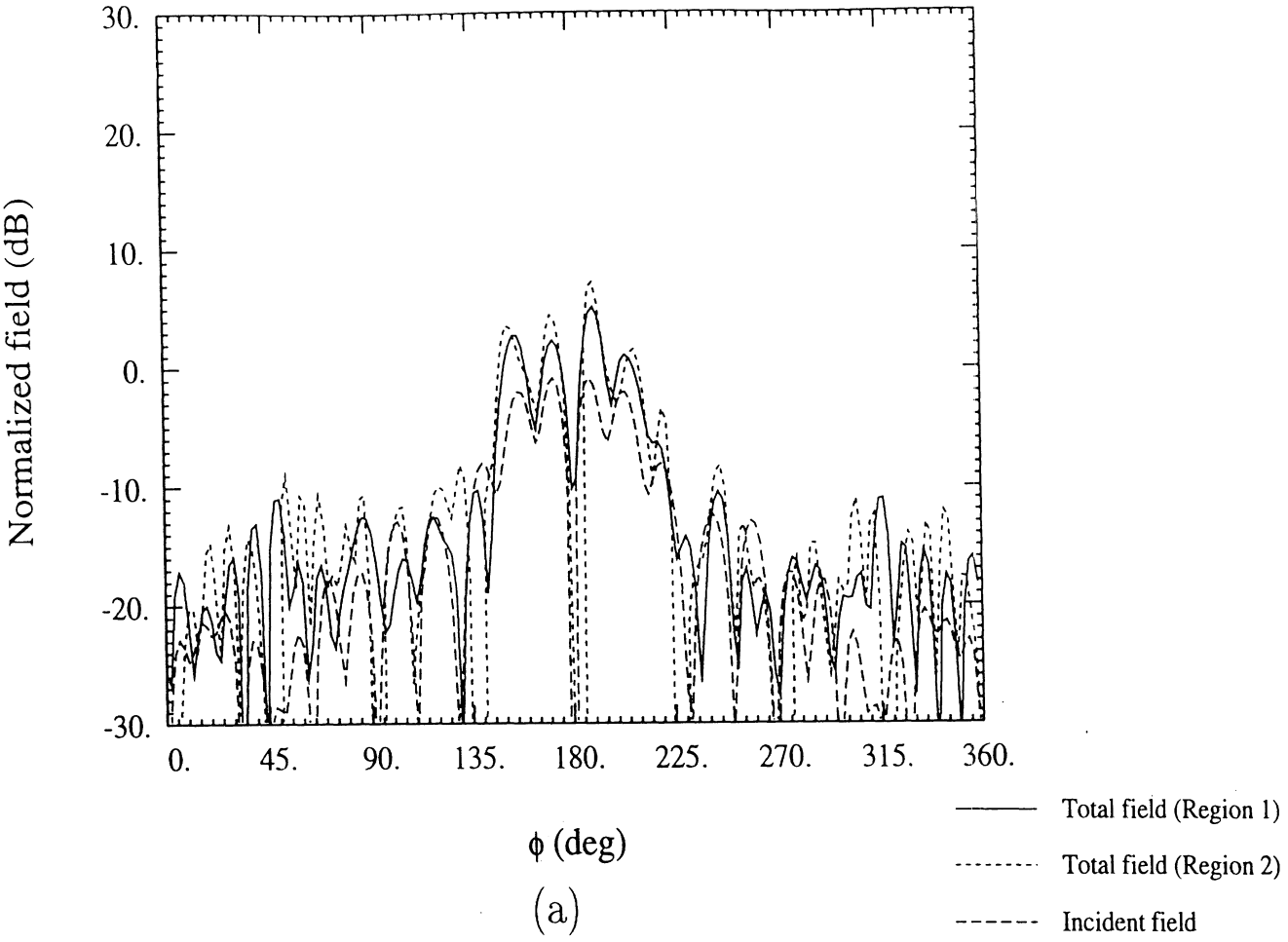

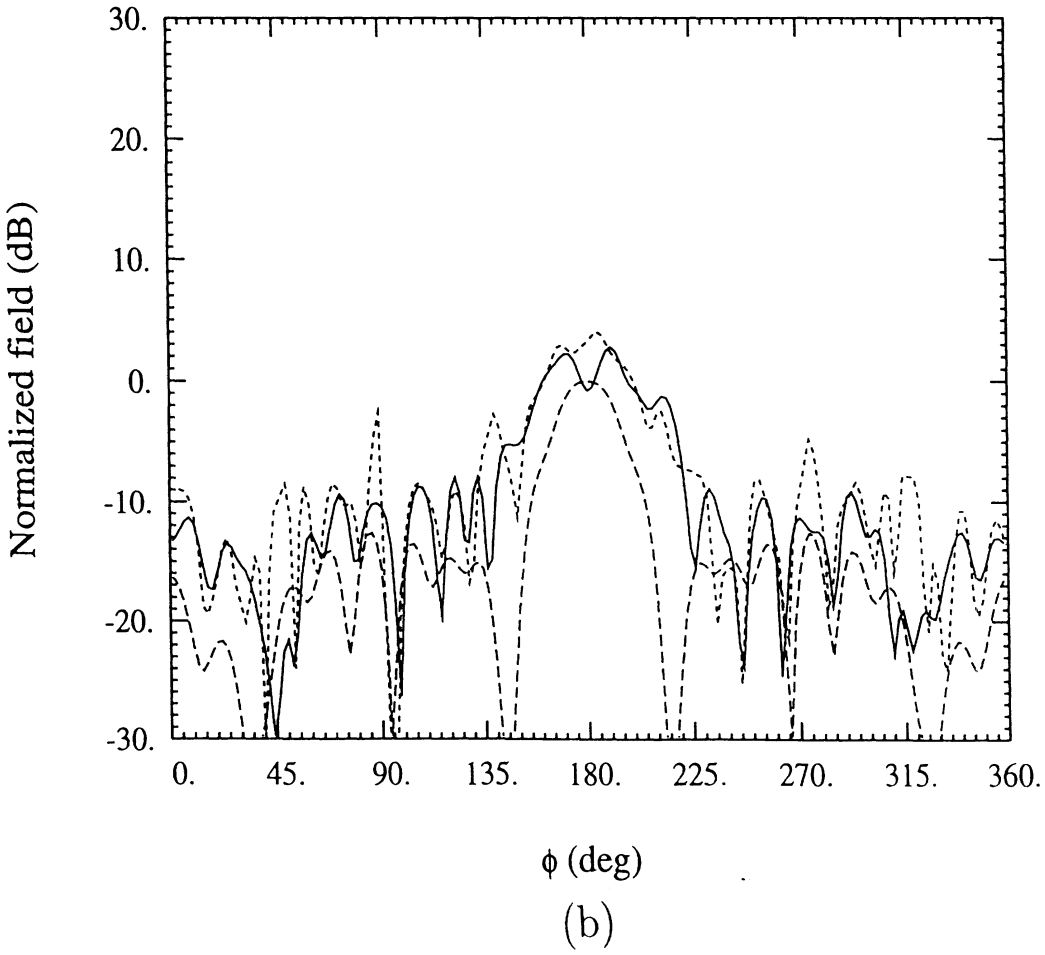

Figure 16. Tangential fields at both sides of the interface for the geometry corresponding to Fig. 14 (θ polarization). The fields are plotted at $\rho = 11.25$ cm. for an incidence angle of $\theta_i = 40^o$. a) ρ component b) ϕ component

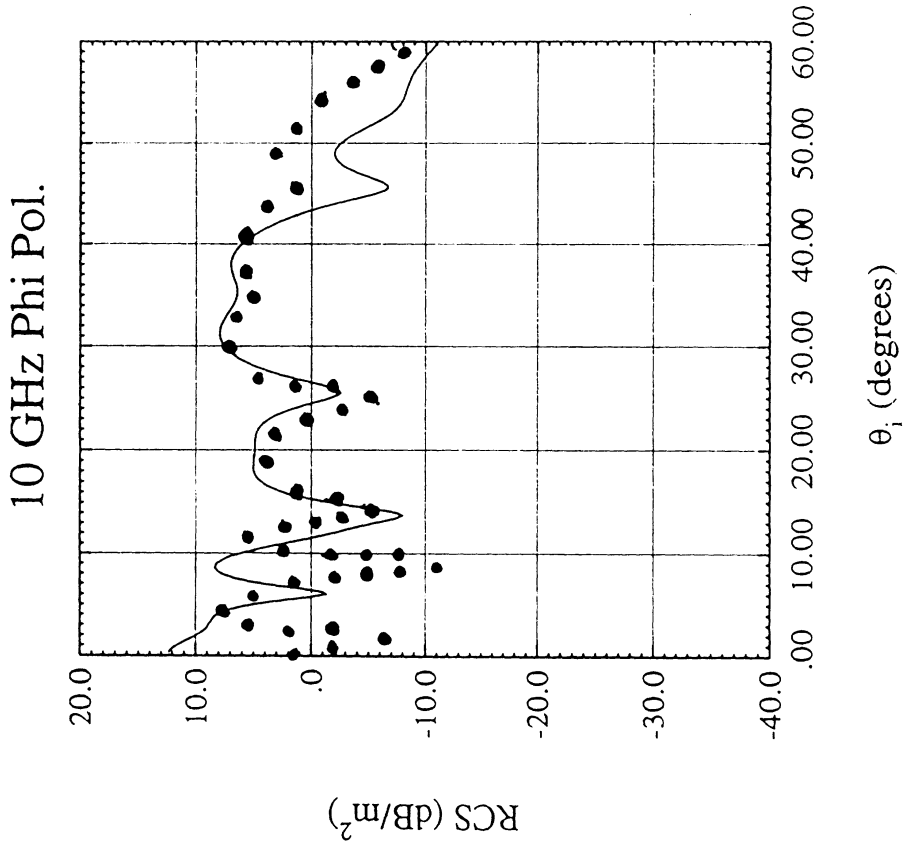

Figure 17. Calculated (solid line) and measured (dotted line) data for the straight blades model at 10 GHz (the model is described in Section 5).

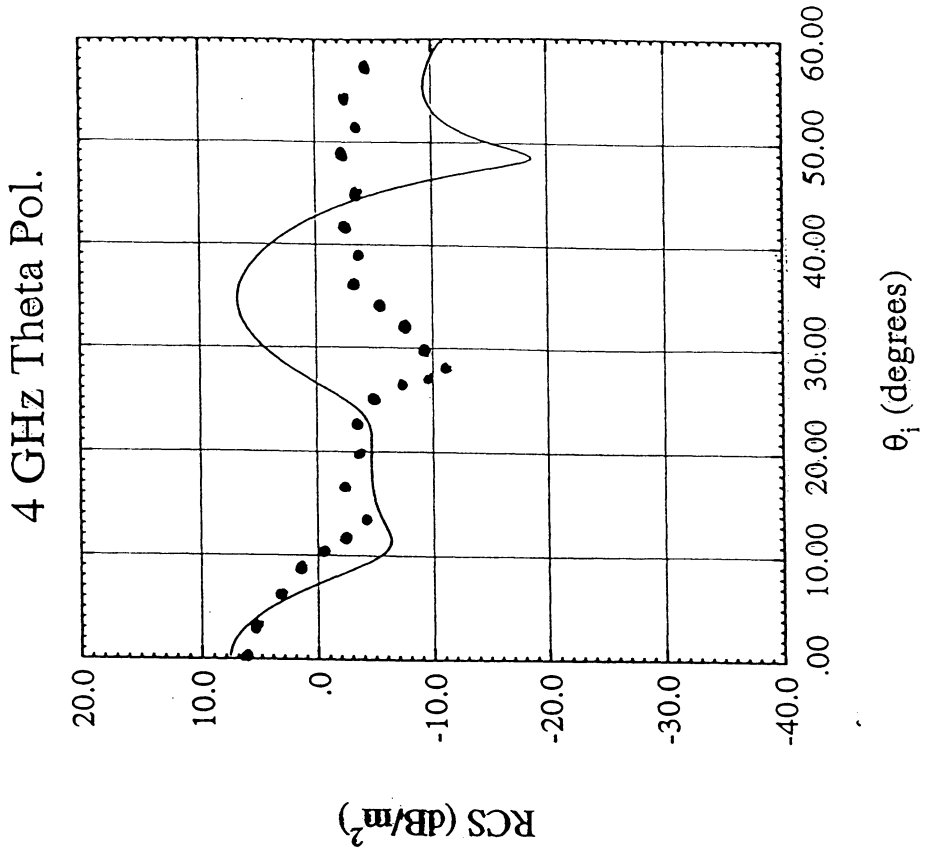

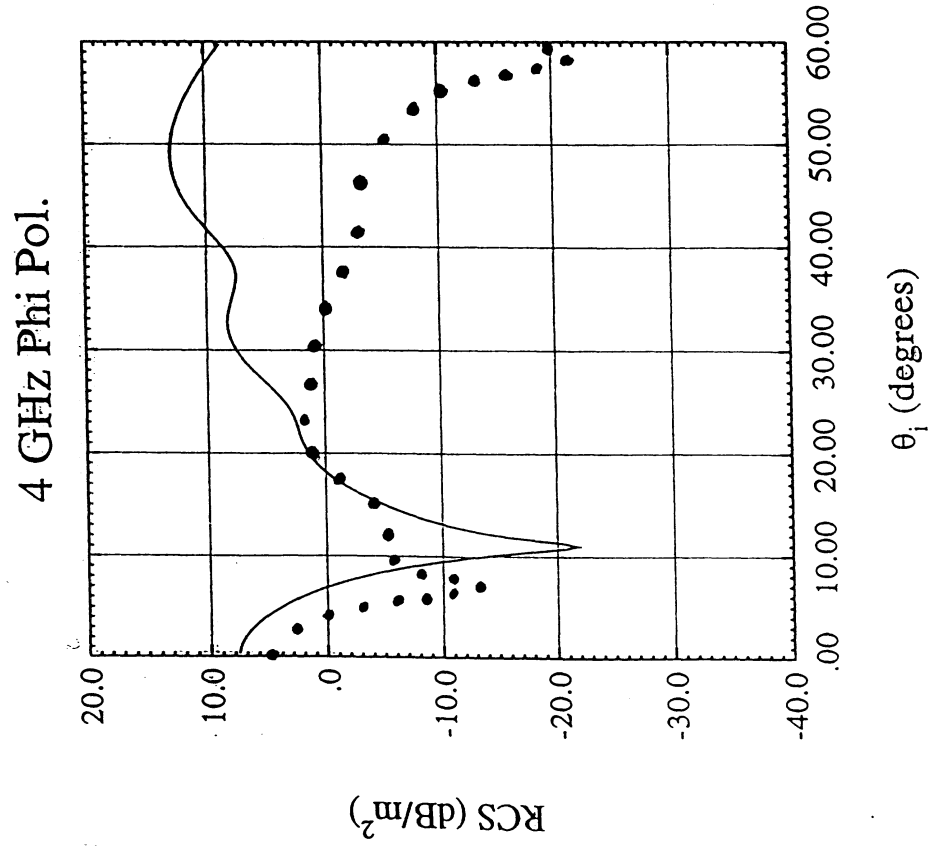

Figure 18. Calculated (solid line) and measured (dotted line) data for the curved blades model at 4 GHz (the model is described in Section 5).

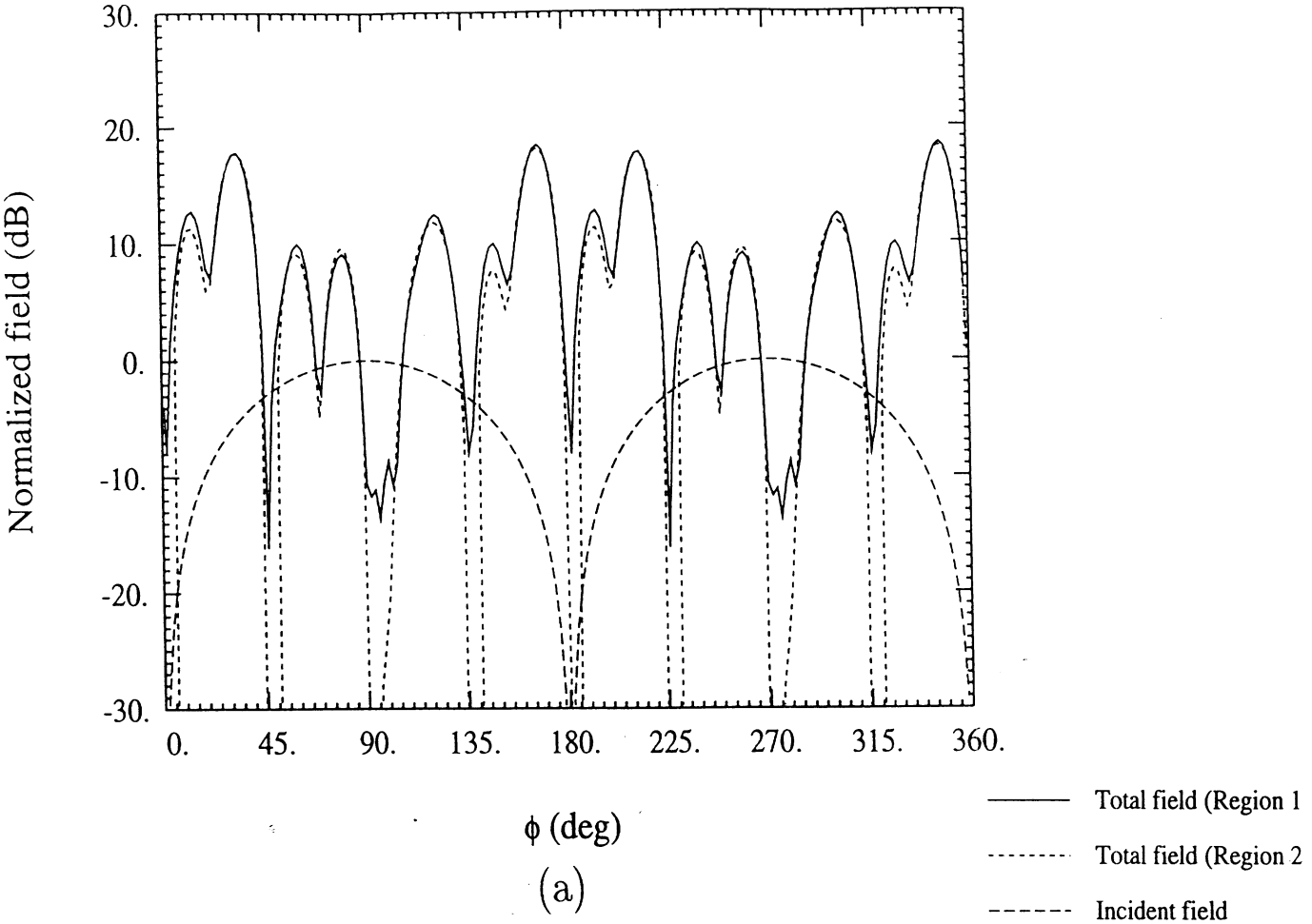

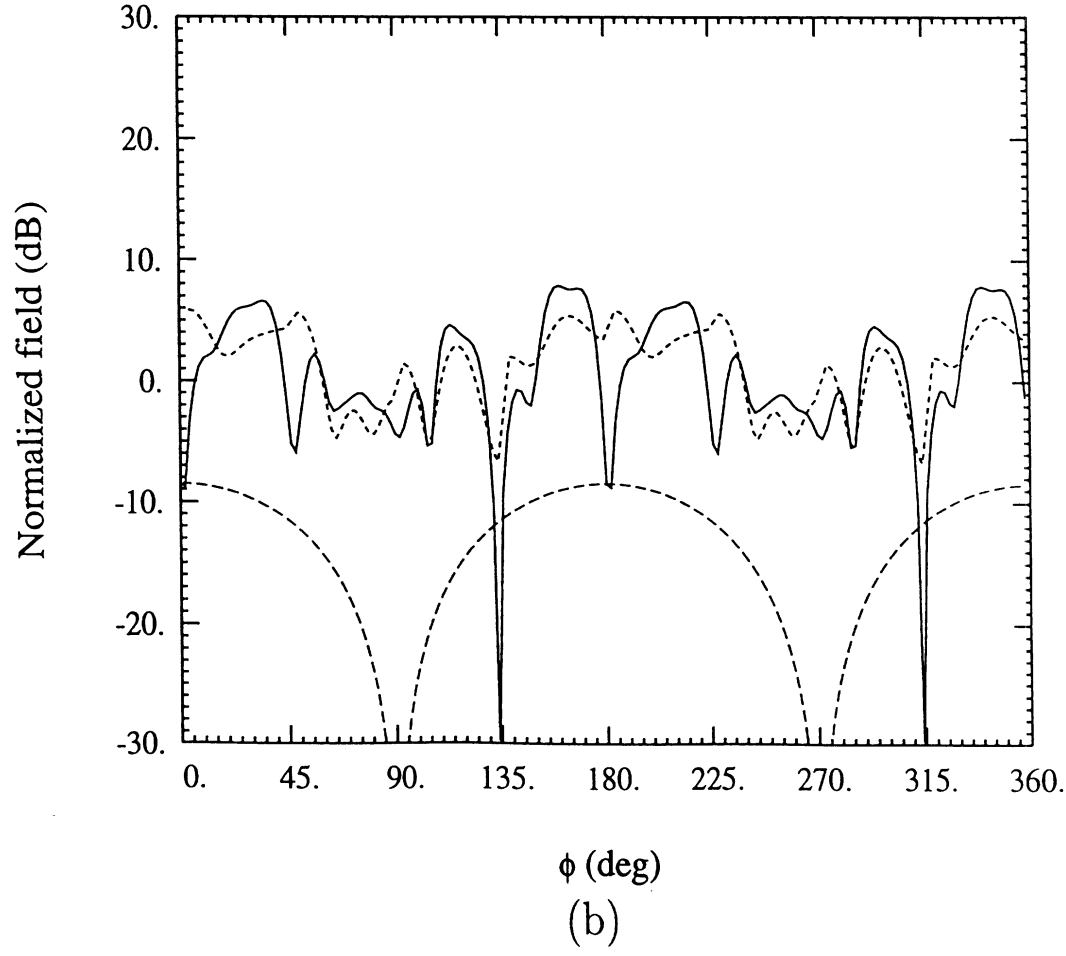

Figure 19. Tangential fields at both sides of the interface for the geometry corresponding to Fig. 18 (ϕ polarization). The fields are plotted at $\rho = 11.25$ cm, for an incidence angle of $\theta_i = 0°$. a) ρ component b) ϕ component

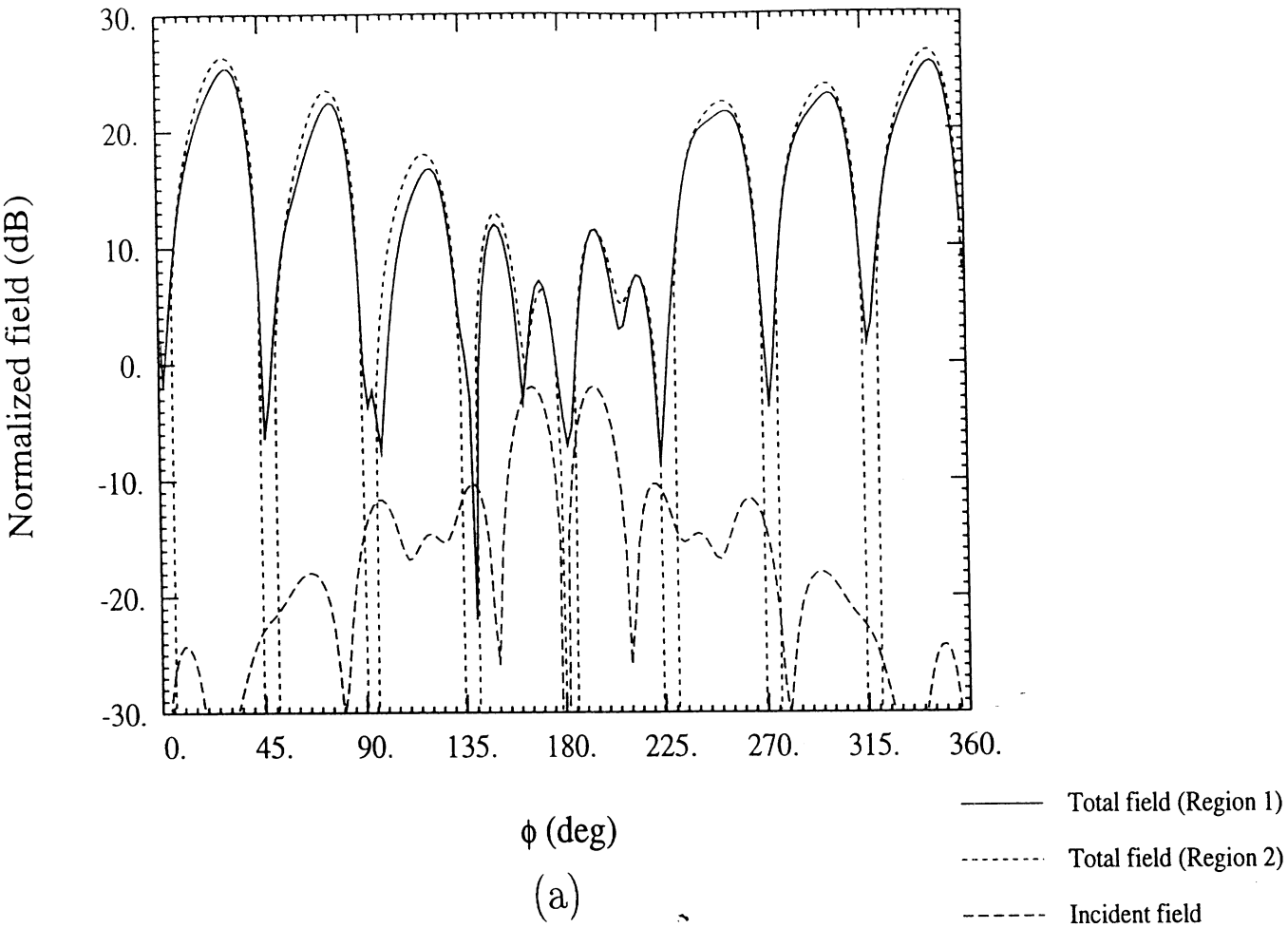

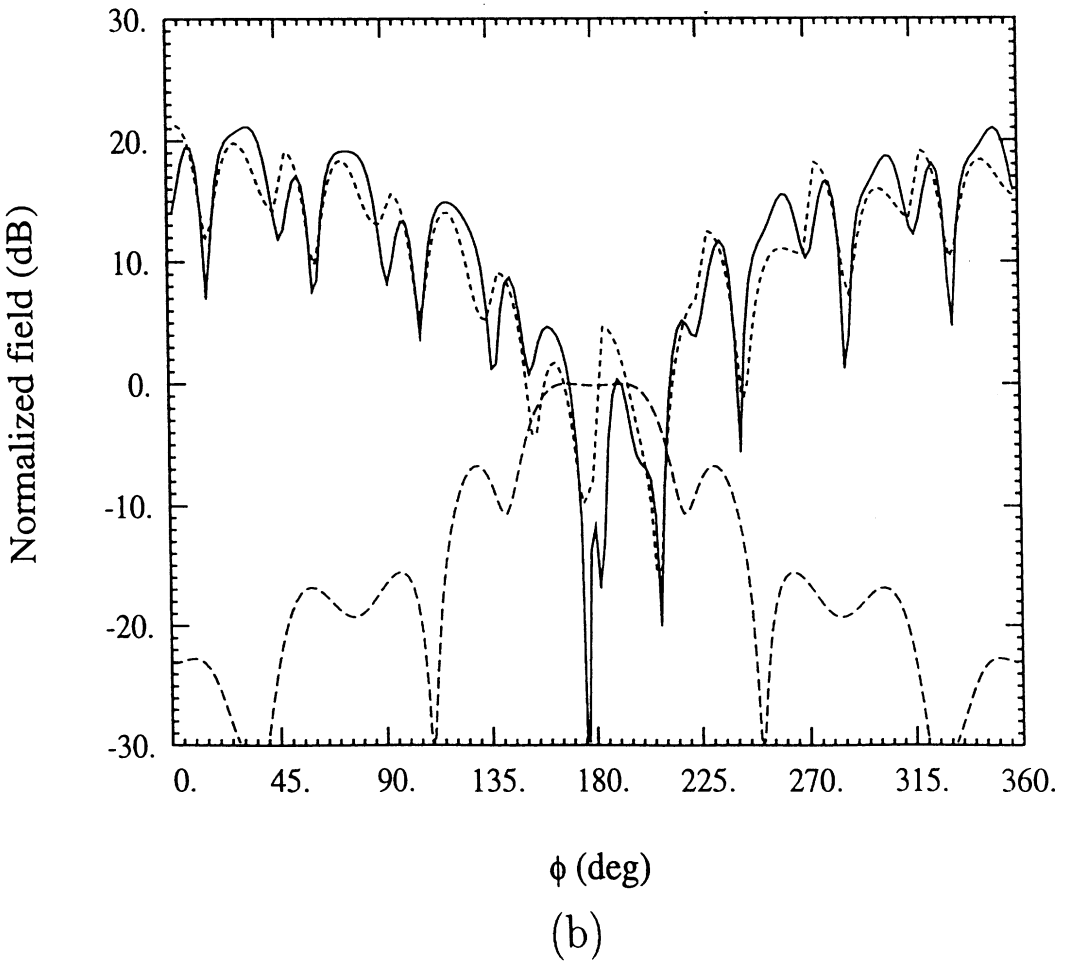

Figure 20. Tangential fields at both sides of the interface for the geometry corresponding to Fig. 18 (ϕ polarization). The fields are plotted at $\rho = 11.25$ cm, for an incidence angle of $\theta_i = 40°$. a) ρ component b) ϕ component

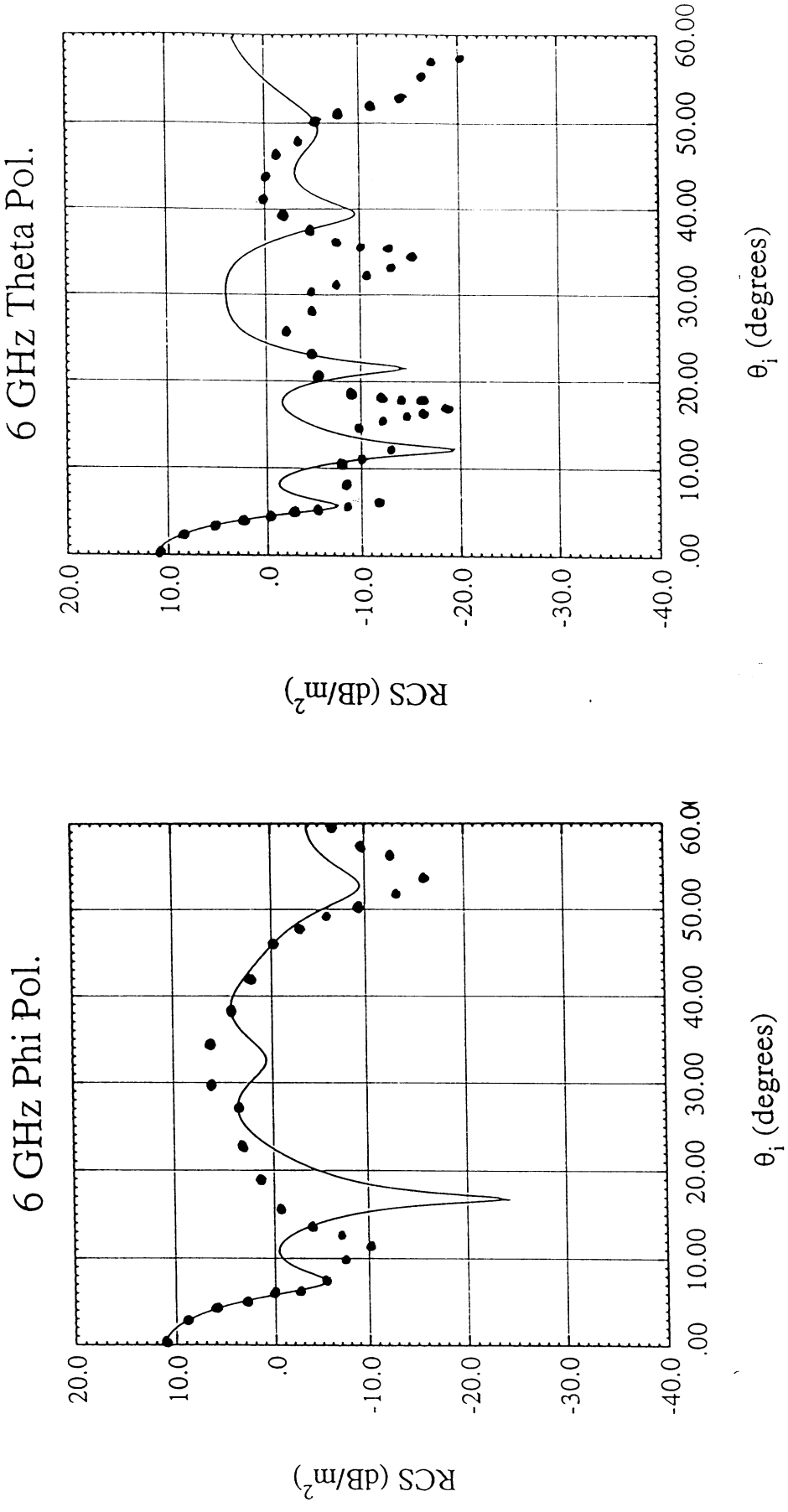

Figure 21. Calculated (solid line) and measured (dotted line) data for the curved blades model at 6 GHz (the model is described in Section 5).

Overlapping Modal and Geometric Symmetries for Computing Jet Engine Inlet Scattering

Daniel C. Ross, John L. Volakis and Hristos T. Anastassiu

Radiation Laboratory

University of Michigan

Ann Arbor MI 48109-2122

abstract -- **By examining the scattering from a cylindrical inlet terminated by a fan-like structure, possessing discrete angular symmetry, it is found that only very limited inter-modal coupling is possible. This fact is exploited in a hybrid finite element/modal scheme to develop a very efficient solution, where only one slice of the geometry need be modeled. It is shown that a phase boundary condition at the interior walls of the mesh is sufficient for the complete solution of the problem. The implementation of the phase boundary condition is detailed for the full three-dimensional case, including special considerations for enforcing the boundary conditions along the axis. A simple example is shown for the sliced, hybrid finite element/modal scheme to validate the method.**

1.0 Introduction

The use of a hybrid finite element/modal technique to model the radar scattering from jet engine inlets is depicted in Figure 1 [1] [2]. Briefly, the finite element method (FEM) is employed to generate a modal scattering matrix for the engine face while some high frequency or modal technique is used to trace the fields in and out of the inlet. It is necessary to perform the FEM analysis once for each traveling mode in the circular inlet to generate the scattering matrix. That is, the incoming field is decomposed into waveguide modes prior to the application of the FEM and the FEM is used only to generate the modal scattering matrix.

While the hybrid finite element/modal technique was validated in [1] for an engine-like termination consisting of straight blades, the electrical sizes considered were small (approximately 1λ radius) where typically the inlet can have a radius of 10λ and greater. Because the number of degrees of freedom grows as the square of the radius, to apply the method directly to large structures would invoke computational costs that are indeed staggering. Also, the number of traveling modes (note that the analysis must be repeated for each mode) and the size of the scattering matrix, grow as the radius squared. For the inlet configurations considered in [1] approximately 50,000 elements were needed with about 20,000 degrees of freedom and the analysis was repeated approximately 10 times, once for each mode. Given this, an inlet which is 10λ in radius would require 100 times the computational resources (5,000,000 elements) and the analysis must be repeated 100 times over (2,000,000 degrees of freedom, 1,000 times) thus increasing the total computational cost by about 10,000. In effect, the computational cost increases as the radius to the fourth power.

Obviously, some physically derived simplification is needed to scale the problem to a workable size. By exploiting the cyclic, geometric symmetry which exists in an engine face, it is shown that the entire problem can be reduced down to a single unique slice of the geometry. For example, if the engine face has 40 blades, it is sufficient to only model, and carry out the analysis for a single angular period of the geometry which encompasses (1/40)'th of the total computational volume. To achieve this computational scaling, it is necessary to work with modal field excitations and not plane wave excitations. The modal field excitations can be found by decomposing the incident plane wave, as is typically done for generating the scattering matrix of the termination. By exploiting the modal

(excitation) and geometric symmetries, it can further be shown that a very limited set of scattered modes are possible. This leads to a very sparse scattering matrix (i.e. very few observables are needed for characterizing the angularly periodic engine face) as has been observed in the past [1] and is mathematically proved in this paper. This physical sifting of the modes by the engine face is similar to the fact that only a discrete spectrum of frequencies are present in the Fourier Transform of a periodic signal. It is also demonstrated that all of the scattered modes have a constant phase shift from one geometry slice to another. From a computational point of view, since all scattered modes have equal phase shift across the slice, a phase boundary condition can be imposed at the two interior faces of the FEM mesh to bound the problem. This technique has been used successfully in [3] and [4] and is extended to 3-dimensions in this paper.

Section 2.0 of this paper justifies that the problem can be scaled down to only one slice by showing that the overlapping modal and geometric symmetries give rise to a limited set of scattered/reflected modes. It is shown that these modes can be modeled with a phase boundary condition on the interior walls of the mesh separating the periodic sectors of the engine face. Thus, only a single slice of the termination geometry need be modeled to yield the scattered fields of the entire geometry. Section 3.0 describes the implementation of the phase boundary conditions for the full three-dimensional problem including some important numerical considerations that if overlooked can lead to ill-conditioned systems. Also, enforcement of the boundary conditions along the axis are discussed in light of the fact that the phase boundary conditions cannot be defined there and thus a different, physically derived set of boundary conditions must be used. Section 4.0 shows results for the hybrid finite element/modal analysis making full use of the overlapping modal and geometric symmetries.

2.0 Overlapping Modal and Geometric Symmetries

Within a cylindrical waveguide, electromagnetic radiation propagates as modes. These modes are classified as being either TE (transverse electric) or TM (transverse magnetic). Each of these two mode classes are associated with four parameters: the positive integers n, p and σ_ϕ, σ_z which take on the values ± 1. The index n is associated with the angular dependence of the modes while the index p is associated with the radial dependance of the modes. Although it is often convenient to use cylindrical waveguide modes whose angular

dependence is either $\cos(n\phi)$ or $\sin(n\phi)$, to exploit the symmetry of the engine face, the modes must be defined as having $e^{\sigma_\phi jn\phi}$ dependence. It is the simple angular phase shift of the modes across a sector that makes possible the exploitation of the geometric symmetry [3]. The index σ_ϕ determines the sense of rotation as the mode propagates down the guide while the index σ_z determines the direction of propagation. All modes have a z dependance of $e^{\sigma_z j\beta z}$ where the propagation constant β is a function of the mode indices n and p and the radius of the guide. A mode having $\sigma_z = +1$ corresponds to an incoming (incident) mode while a mode having $\sigma_z = -1$ corresponds to an outgoing (scattered) mode. The modal electric field will be denoted by $\overline{\Psi}^i_{n,p}$ for incident modes and $\overline{\Psi}^s_{n,p}$ for scattered modes, each actually corresponding to a TE/TM pair. Whenever the second index p is dropped in an expression, it is understood that the expression must be summed over all values of p. For example, when we express the scattered field as a sum of scattered modes using $\overline{E}_s(x, y, z_0) = \sum b_{n_{out}} \overline{\Psi}^s_{n_{out}}(x, y, z_0)$ it is understood that the RHS of this expression is summed over $p = 0, 1, 2, 3, 4\ldots$

Consider a unique slice of an engine-like termination as shown in Figure 2. Let ϕ_s be the angular extent of the unique slice of the geometry. For any fan-like structure $\phi_s = \frac{2\pi}{N_s}$ where N_s is the symmetry number (number of blades). Since the incident field will be a cylindrical mode with an angular dependance of the form $e^{\pm jn_{in}\phi}$, the FEM system resulting from a solution of the entire problem would take the form

$$\begin{bmatrix} K^1 & & & & \\ & K^2 & & & \\ & & K^3 & & \\ & & & \cdots & \\ & & & & K^{N_s} \end{bmatrix} \begin{pmatrix} E_s^1 \\ E_s^2 \\ E_s^3 \\ \cdots \\ E_s^{N_s} \end{pmatrix} = \begin{pmatrix} f \\ fe^{\pm jn_{in}\phi_s} \\ fe^{\pm 2jn_{in}\phi_s} \\ \cdots \\ fe^{\pm (N_s-1)jn_{in}\phi_s} \end{pmatrix} \quad (1)$$

where E_s^k is the unknown scattered electric field in slice k. Because the geometry is the same in each slice, $K^1 = K^2 = K^3 \ldots = K^{N_s}$ and by linearity, the unknown scattered fields must all be equal to within a phase factor. That is

$$
\begin{aligned}
E_s^2 &= E_s^1 e^{\pm jn_{in}\phi_s} \\
E_s^3 &= E_s^1 e^{\pm j2n_{in}\phi_s} \\
&\cdots \\
E_s^{N_s} &= E_s^1 e^{\pm j(N_s-1)n_{in}\phi_s}
\end{aligned}
\tag{2}
$$

and consequently, the scattered field is a periodic function in ϕ with period ϕ_s and a progressive phase advance of $e^{\pm jn_{in}\phi_s}$ in each period (slice). This restricts the possible scattered field modes, and to find which scattered modes can make up such a field, we consider the modal decomposition of the scattered field. Specifically, on a cross section Γ of the guide located somewhere within the termination region (say at $z = z_0$)

$$
\bar{E}_s(x, y, z_0) = \sum_{n_{out}=0}^{\infty} b_{n_{out}} \bar{\Psi}^s_{n_{out}}(x, y, z_0) \tag{3}
$$

where the coefficients $b_{n_{out}}$ are found by taking the inner product of the transverse scattered field ($\bar{e}^s$) with each of the outgoing (scattered) modes $\bar{\Psi}^s_{n_{out}}$.

$$
b_{n_{out}} = \frac{\int_\Gamma \bar{e}^s(x, y, z_0) \cdot \bar{\Psi}^{s*}_{n_{out}}(x, y, z_0)\, ds}{\int_\Gamma \bar{\Psi}^s_{n_{out}}(x, y, z_0) \cdot \bar{\Psi}^{s*}_{n_{out}}(x, y, z_0)\, ds} \tag{4}
$$

Considering the angular dependance only, the above expansion is seen to reduce to a Fourier Transform with respect to ϕ since the scattered modes have an $e^{\pm jn_{out}\phi_s}$ dependance. That is, the variables ϕ and n_{out} are a Fourier Transform pair. It is thus important to investigate the spectral content of a signal which is periodic in ϕ, but has a progressive phase advance $e^{\pm jn_{in}\phi_s}$ from one period to the next.. In so doing, the set of possible scattered modes will be found.

Consider a signal $S(\phi)$ which is periodic in ϕ but has a progressive phase advance $e^{\pm jn_{in}\phi_s}$ as illustrated below:

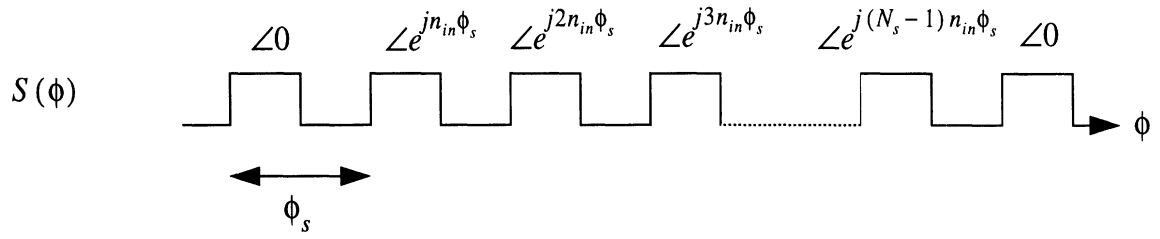

This signal can be thought of as a sum of N_s signals, each with an angular offset and a phase shift from a reference signal $S_0(\phi)$ where

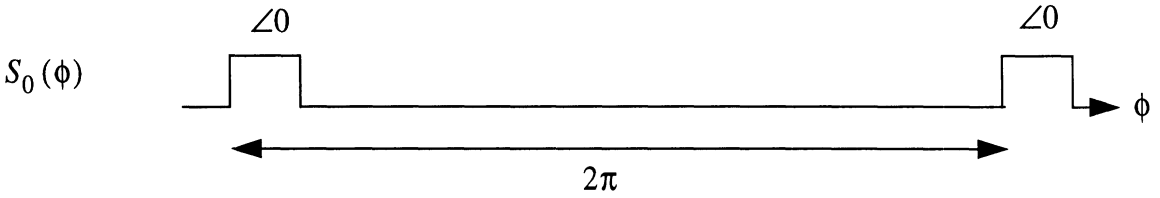

Mathematically,

$$S(\phi) = \sum_{k=0}^{N_s-1} S_0(\phi - k\phi_s)\, e^{jkn_{in}\phi_s} \tag{5}$$

and the Fourier Transform ($\phi \leftrightarrow n_{out}$) of such a signal can be readily found using the properties of shifting and linearity to give

$$\tilde{S}(n_{out}) = \tilde{S}_0(n_{out}) \sum_{k=0}^{N_s-1} e^{jk(n_{in}-n_{out})\phi_s} = \begin{cases} \dfrac{e^{jN_s(n_{in}-n_{out})\phi_s}}{e^{j(n_{in}-n_{out})\phi_s}}\tilde{S}_0 = 0 & n_{out} \neq n_{in} \pm mN_s \\ N_s\tilde{S}_0 & n_{out} = n_{in} \pm mN_s \end{cases} \tag{6}$$

where m is any integer.

That is, only if

$$n_{out} = n_{in} \pm mN_s \qquad m\text{: any integer} \tag{7}$$

is $\tilde{S}(n_{out})$ nonzero. Thus the spectrum of $S(\phi)$ is made up of a limited set of modes, whose index is given by (7).

The implication of (7) is that for a given N_s (symmetry number or number of blades), only certain scattered modes can exist for a given incident mode, and this of course implies a very sparse scattering matrix. For example, if there are 17 blades and the incident mode is associated with $n_{in} = 1$, then only scattered modes which have $n_{out} = 1, 18, -16, 35, -33 \ldots$ can exist. For $n_{in} = 2$ only scattered modes with $n_{out} = 2, 19, -15, 36, -32 \ldots$ will be present in the scattered field. With this property in mind, it is worthwhile to consider if any additional physical insights can be gained with the goal of simplifying the characteristics of this complex scattering problem.

For an inlet termination with axial symmetry (a body of revolution, such as a circular stub, a cone, a bulb etc.) the symmetry number N_s goes to infinity. Consequently, on the basis of the above discussion coupling can only occur to modes which carry the same angular dependence (i.e. $n_{out} = n_{in}$). This is consistent with what is known from classical body of revolution theory [5]. An important practical implication of (7) is that as the number of blades increases, the higher order scattered modes will be pushed up farther, and coupling to these higher order modes will become vanishingly small if the modes are highly evanescent. However, even if these higher order modes do propagate, they will often be of such a radically different nature so that coupling must again be very weak. Thus, structures with many blades will have dominant scattered modes carrying the index $n_{out} = n_{in}$.

An interesting observation from the above analysis is that coupling does not occur to modes having $n_{out} = n_{in} \pm 1$ since a symmetry number of 1 ($N_s = 1$) is not a possibility. This fact will turn out to be of great importance for establishing boundary conditions on the axis of the FEM solution. To consider more of the impact of the limited mode property on the FEM solution, note that all of the possible scattered modes share a common phase shift from symmetry face 1 to symmetry face 2, (see Figure 2). Thus, all scattered modes are related, on a cut of constant z, from face 2 to face 1 by

$$E_\rho^2 = E_\rho^1 e^{\pm jn_{in}\phi_s}$$
$$E_\phi^2 = E_\phi^1 e^{\pm jn_{in}\phi_s} \tag{8}$$
$$E_z^2 = E_z^1 e^{\pm jn_{in}\phi_s}$$

where E^2 is the scattered field on face 2 and E^1 is the scattered field on face 1. This fact was first exploited in [4] to efficiently compute eigenmodes within a cyclotron using FEM. For the jet engine scattering problem at hand, a phase boundary condition can be used to restrict the FEM computational region to a single slice of the original problem. The implementation of the phase boundary condition for three-dimensional FEM analysis of the engine face is discussed next.

3.0 Phase Boundary Conditions for 3-D FEM

In the previous section it was shown that the only condition needed to relate the fields on the two symmetry faces is a phase boundary condition (8). However, the implementation of this condition is complicated because it must be enforced over a surface which includes the cylinder axis at which the phase conditions cannot be defined and must therefore be replaced.

For the initial implementation of the FEM, the mesh which is generated to model the slice must have coincident nodes and elements on the two symmetry faces. In this manner, for each degree of freedom on face 2 (E_x^2,E_y^2, E_z^2), there is a corresponding degree of freedom on face 1 (E_x^1,E_y^1, E_z^1). (Alternatively, interpolation may be employed to remove the restriction of coincident nodes on the faces.) During assembly of the FEM system, degrees of freedom on face 2 can be discarded in favor of degrees of freedom on face 1 by enforcing the phase boundary condition as

$$\begin{aligned}
\hat{\rho}^2 \cdot (\hat{x}E_x^2 + \hat{y}E_y^2) &= \hat{\rho}^1 \cdot (\hat{x}E_x^1 + \hat{y}E_y^1)\, e^{\pm jn_{in}\phi_s} \\
\hat{\phi}^2 \cdot (\hat{x}E_x^2 + \hat{y}E_y^2) &= \hat{\phi}^1 \cdot (\hat{x}E_x^1 + \hat{y}E_y^1)\, e^{\pm jn_{in}\phi_s} \\
E_z^2 &= E_z^1 e^{\pm jn_{in}\phi_s}
\end{aligned} \tag{9}$$

After some algebra (9) becomes

$$\begin{aligned}
E_x^2 &= \frac{\left[\rho_x^1 - \rho_y^2\left(\frac{\phi_x^1}{\phi_y^2}\right)\right] e^{\pm jn_{in}\phi_s} E_x^1 + \left[\rho_y^1 - \rho_y^2\left(\frac{\phi_y^1}{\phi_y^2}\right)\right] e^{\pm jn_{in}\phi_s} E_y^1}{\rho_x^2 - \rho_y^2\left(\frac{\phi_x^2}{\phi_y^2}\right)} \\
E_y^2 &= \frac{\left[\phi_x^1 - \phi_x^2\left(\frac{\rho_x^1}{\rho_x^2}\right)\right] e^{\pm jn_{in}\phi_s} E_x^1 + \left[\phi_y^1 - \phi_x^2\left(\frac{\rho_y^1}{\rho_x^2}\right)\right] e^{\pm jn_{in}\phi_s} E_y^1}{\phi_y^2 - \phi_x^2\left(\frac{\rho_y^2}{\rho_x^2}\right)} \\
E_z^2 &= e^{\pm jn_{in}\phi_s} E_z^1
\end{aligned} \tag{10}$$

where $\rho^1_{(x,y)}, \phi^1_{(x,y)}$ and $\rho^2_{(x,y)}, \phi^2_{(x,y)}$ are the components of the polar unit vectors at face 1 and 2, respectively. Expression (10) can be used directly to assemble degrees of freedom on face 1 in favor of degrees of freedom on face 2.

Since the hybrid FEM-Modal formulation as shown in Figure 1 makes use of an absorbing layer to truncate the mesh, the space between the engine face and the absorber must include the axis of the guide. Consequently, some degrees of freedom are located on the axis (since part of the axis is non-metallic) and this introduces a complication in applying the slicing scheme not been previously encountered in the literature. While the transverse, polar field components cannot be defined on the axis, the transverse cartesian have specific values. This fact is a motivation in formulating the finite element solution in terms of cartesian rather than polar components.

In practice, boundary conditions on the axis must be imposed differently for each modal excitation. By considering the field behavior along the axis, and the limited mode coupling effect, a consistent set of boundary conditions can be applied along the axis. First, con-

sider the behavior of the modes on the axis as shown in Table 1. Since it was previously noted that mode coupling does not occur to modes having $n_{out} = n_{in} \pm 1$, there will never be a mode from column 1 and column 2 which exist concurrently. If a mode included in column 1 is present, i.e. n_{in} *modulo* $N_s = 0$, then the boundary conditions to be enforced on the axis are $E_x = E_y = 0$ which is consistent with all possible scattered modes. If a mode from column 2 is present, i.e. $(n_{in} \pm 1)$ *modulo* $N_s = 0$ then the boundary condition $E_z = 0$ is enforced. If all scattered modes are such that $n_{out} > 1$, then the conditions $E_x = E_y = E_z = 0$ are imposed.

TABLE 1. Behavior of modes on axis

MODE	n=0	n=1	n>1
TE E_x, E_y	$= 0$	$\neq 0$	$= 0$
TE E_z	$= 0$	$= 0$	$= 0$
TM E_x, E_y	$= 0$	$\neq 0$	$= 0$
TM E_z	$\neq 0$	$= 0$	$= 0$

Careful implementation of the boundary conditions on conductors was also necessary to preserve the condition of the system. Of most importance is the implementation of boundary conditions on conductors that cross the symmetry face. In this case, conditions must be enforced so that during assembly, both the phase and the metal boundary conditions are enforced without causing deterioration of the system's condition. This can be accomplished using the following procedure which is performed at the element level.

For a degree of freedom located on a conductor surface with normal $\hat{n}$ at symmetry face 1:

- if $|\hat{\phi} \times \hat{n}| > 0.15$, then set $\hat{t}_1 = \dfrac{\hat{\phi} \times \hat{n}}{|\hat{\phi} \times \hat{n}|}$ else set $\hat{t}_1 = \dfrac{\hat{\rho} \times \hat{n}}{|\hat{\rho} \times \hat{n}|}$
- $\hat{t}_2 = \dfrac{\hat{z} \times \hat{t}_1}{|\hat{z} \times \hat{t}_1|}$

•Given the three local equations for E_x^s, E_y^s and E_z^s

- find the largest component of $\hat{t}_1$ (x, y or z) and replace the corresponding equation in the element system with $\hat{t}_1 \cdot \bar{E}^s = -\hat{t}_1 \cdot \bar{E}^{inc}$

- find the largest component of $\hat{t}_2$ (x, y or z) and replace the corresponding equation in the element system with $\hat{t}_2 \cdot \bar{E}^s = -\hat{t}_2 \cdot \bar{E}^{inc}$

For a degree of freedom that is located on a conductor at symmetry face 2, the procedure is the same except that the largest component of the tangent vectors ($\hat{t}_1$ and $\hat{t}_2$) must be found for the corresponding degree of freedom on face 1 (not face 2) and the local equations are replaced accordingly. In this manner, when (10) is used for assembly, both boundary conditions (on face 1 and face 2) will be enforced correctly and the condition of the system will be preserved. It is however noted, that if the slice angle ϕ_s approaches 90 degrees, the formulation breaks down as the boundary conditions on face 1 and face 2 become orthogonal and cannot be enforced simultaneously. This can be seen by inspection of (10) but is not of importance since real jet engine faces always have many more than four blades.

4.0 Example

As an example, an inlet terminated in a short with radius of 0.66λ is analyzed by using only a 4 degree slice of the original problem. While this geometry is in fact a body of revolution, it is nevertheless an important benchmark for validating the correct implementation of the phase boundary conditions. The absorber is placed 0.5λ from the short and the connectivity boundary (where the scattering matrix is calculated) is located 0.25λ from the short. In this case, any size slice is sufficient, but a balance was achieved by considering that if the slice is too thin, more elements will be needed as the element size must shrink to fill the narrow slice. The calculated scattered fields on the slice boundary for two modal excitations are depicted in Figure 3 and Figure 4 and are seen to have the correct behavior everywhere including the axis. When calculating the scattering matrix, this termination should simply generate a diagonal matrix with each mode having a reflection coefficient of -1. The errors in our calculations using a 4 degree slice are given in Table 2 for the first five modes. These errors are within acceptable ranges for finite element imple-

mentations and are mainly attributable to the finite reflections from the absorber used to terminate the mesh

TABLE 2. Error in the calculated reflection coefficients for an inlet terminated in a short, using a 4 degree slice.

Mode	TM_{01}	TM_{11}	TE_{01}	TE_{11}	TE_{21}
% error	-0.99%	-5.77%	+.12%	+2.35%	-.06

5.0 Conclusions

In this paper we introduced the concept of limited mode coupling for simplifying and scaling the hybrid finite element-modal solution of jet engine inlet scattering applications. It was shown that angularly periodic inlet/waveguide terminations lead to very sparse scattering matrices and mode-to-mode coupling can be predicted a priori to reduce storage and computing requirements. Most importantly, it was shown that periodic phase boundary conditions can be used to restrict the computational volume to a single periodic cell, as is typically done with ordinary, periodic antenna arrays. Since the analysis of jet engine inlet scattering by 3-dimensional FEM requires that degrees of freedom be defined along the axis, a consistent set of physically derived boundary conditions for the fields along the axis was given. The phase boundary condition alone is not sufficient to solve the problem, as the conditions for the fields along the axis must be included. Also, the extension of the periodic phase boundary conditions to a full 3-dimensional FEM solution required the development of practical procedures for enforcing the boundary conditions without destroying the system condition. It was shown that the above analysis could accurately predict the modal fields scattered from a shorted inlet using only a 4 degree slice of the actual cylindrical region.

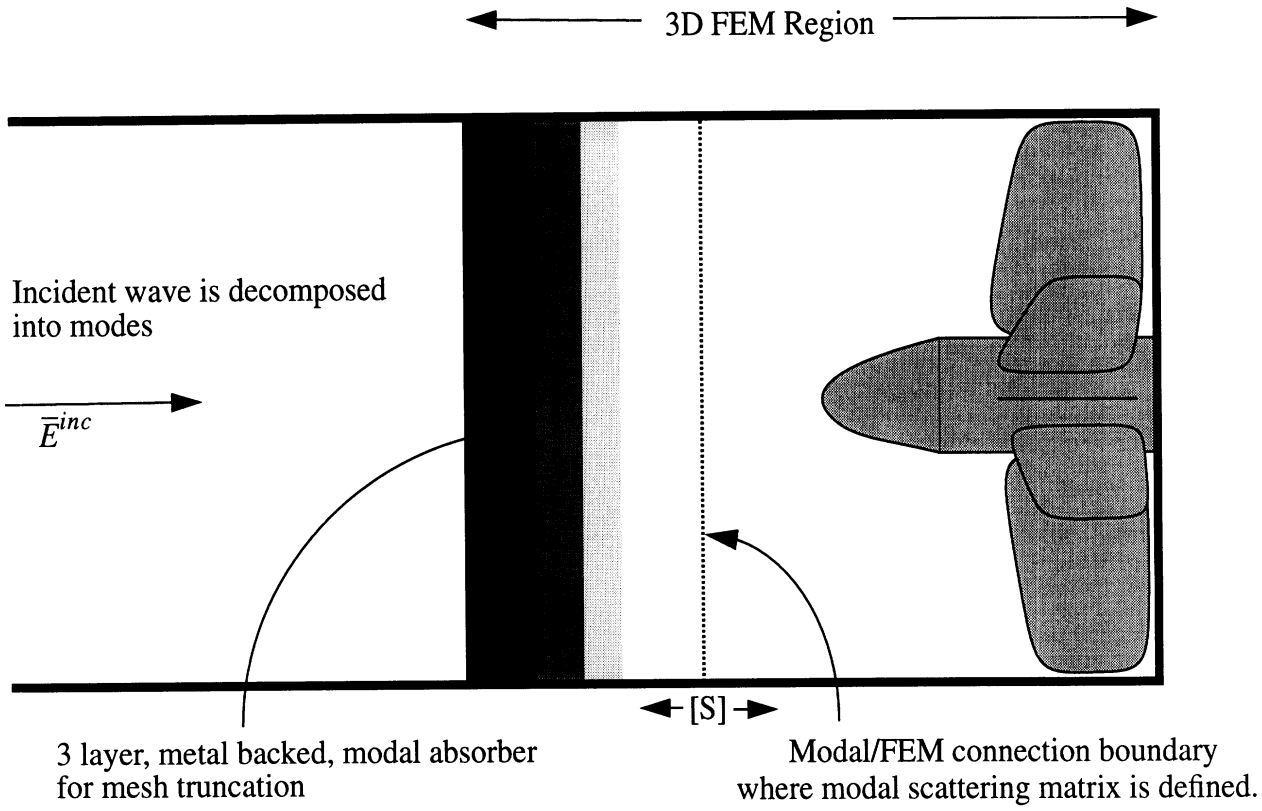

FIGURE 1. Illustration of the hybrid finite element-modal analysis of jet engine inlet scattering

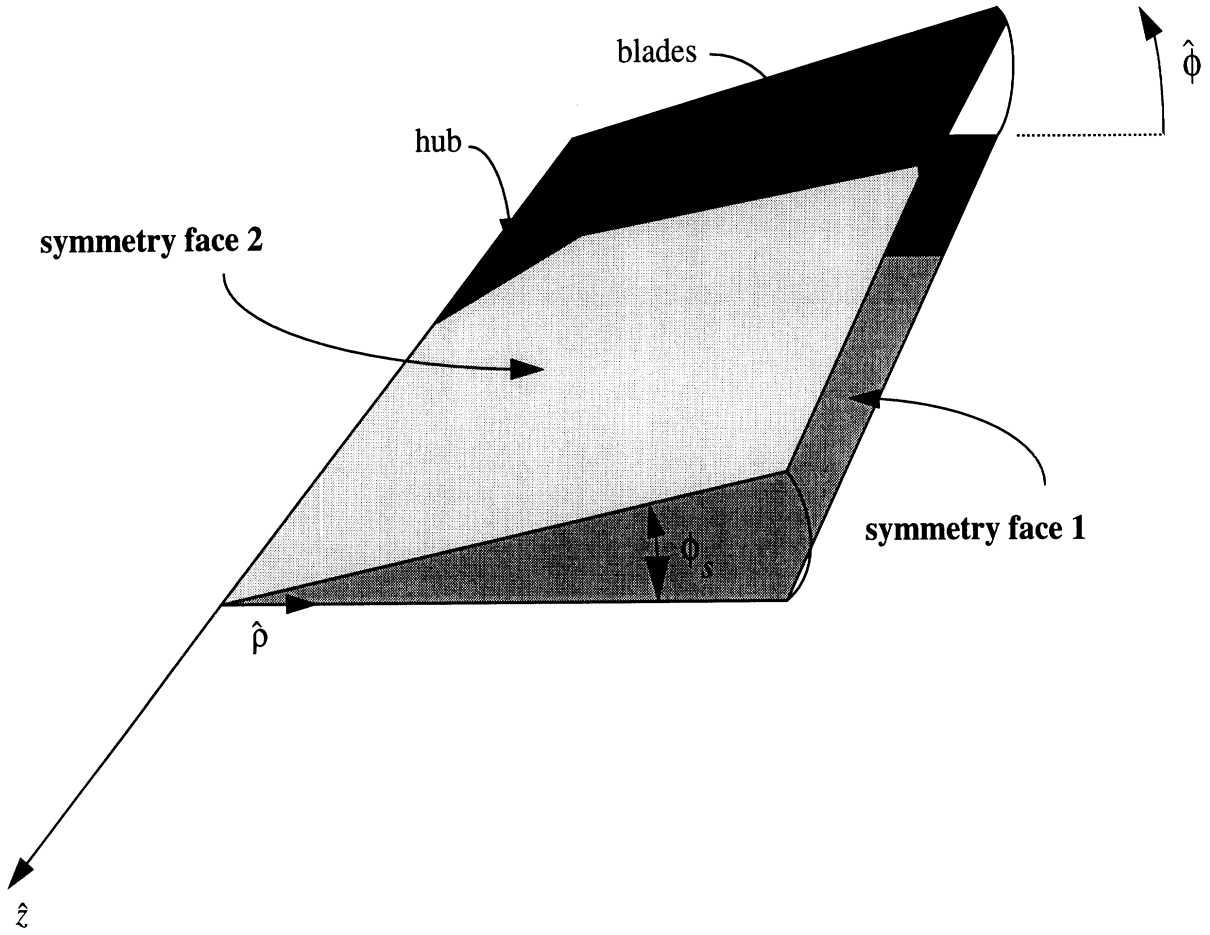

FIGURE 2. A unique slice of an engine-like termination.

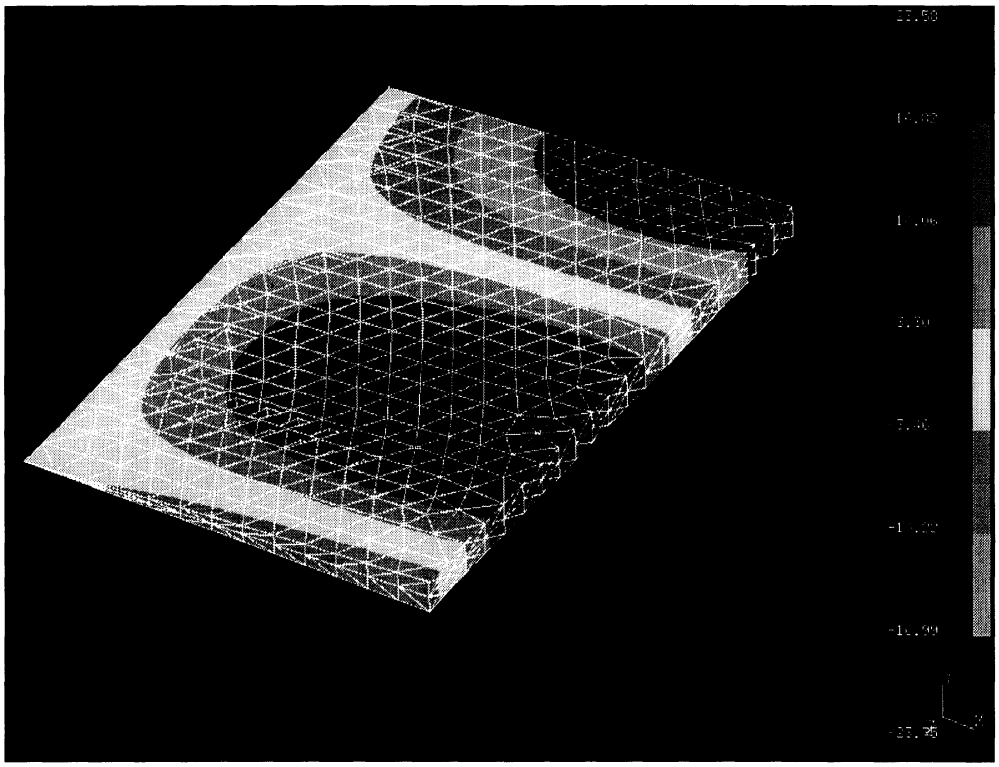

FIGURE 3. Calculated scattered field $Re\,(E_\rho)$ for TM_{01} excitation of a shorted inlet using a four degree slice.

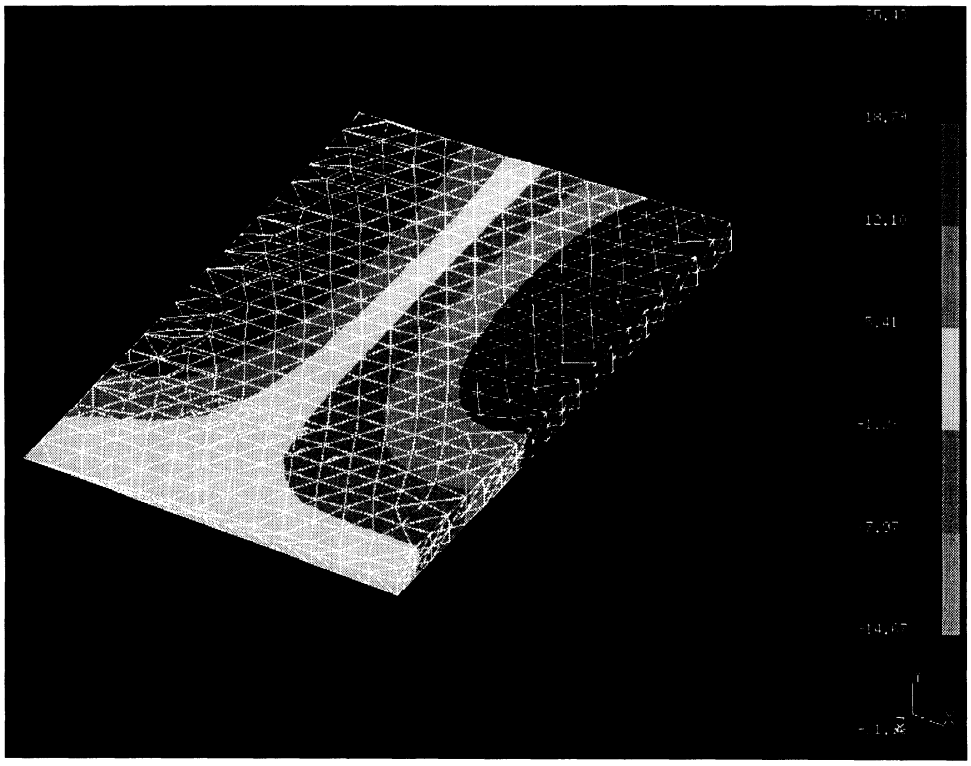

FIGURE 4. Calculated scattered field ($Re\,(E_\rho)$)for TE_{11} excitation of a shorted inlet using a four degree slice

REFERENCES

[1] D.C. Ross, J.L. Volakis and H.T. Anastassiu, "Hybrid Finite Element-Modal Analysis of Jet Engine Inlet Scattering", Submitted to I*EEE Trans. Antennas and Propagation.*

[2] Robert Lee and Tse-Tong Chia, "Analysis of Electromagnetic Scattering from a Cavity with a Complex Termination by Means of a Hybrid ray-FDTD Method", *IEEE trans. Antennas and Propagation*, Vol. 41, No. 11, pp. 1560-1569, Nov. 1993

[3] E.M. Nelson, "High Accuracy Electromagnetic Field Solvers for Cylindrical Waveguides and Axisymmetric Structures Using the Finite Element Method", Ph.D. dissertation, Stanford University, Stanford, CA, 1993; also SLAC-431

[4] A. Frenkel, J.R. Brauer and M.A. Gockel, "Complex Periodic Boundary Conditions for AC Finite Element Models", *Proceedings of the 10th Annual ACES Conference*, 1994, pp. 195-202.

[5] J.R. Mautz and R.F. Harrington, "Radiation and Scattering from Bodies of Revolution," Appl. Sci. Res., vol. 20, pp. 405-435, June 1969.

A Limited Mode Model for Engine Face Analysis

Daniel C. Ross, John L. Volakis and Hristos T. Anastassiu

Radiation Laboratory

University of Michigan

Ann Arbor MI 48109-2122

abstract -- The phenomenon of limited mode coupling, due to the overlapping geometric and modal symmetries in the simulation of jet engine scattering, is fully exploited to create a new method (the limited mode method) for the analysis of jet engine faces. Since an engine face is electrically large, and is made up of multiple sections, each having a different angular symmetry number, materials, changes in inlet radius, and complex curved blades, the analysis technique must be very efficient yet flexible enough to handle complex, realistic structures. The limited mode model meets these requirements by simulating the engine face as a cascade of discrete angularly symmetric obstacles under single mode excitation which allows for the reduction of the dyadic Green's function to a singly infinite series. Also, under single mode excitation, only a slice of the surface mesh of the obstacles are needed and the angular dependance of the induced currents can be transferred to the basis functions, greatly reducing the number of degrees of freedom in the model. Preliminary results are shown and the computational costs are compared with other existing, less efficient techniques.

1.0 Introduction

Having found that direct application of the finite element method (FEM) to the problem of engine scattering analysis was practical only at low frequencies ($f < 1$ GHz.), drastic improvements in efficiency were sought. By taking advantage of the overlapping modal and geometric symmetries, it was found that only a slice of the engine face need be modeled. The notion of limited mode coupling, which makes this simplification possible then sparked the development of an entirely new method that is at once simple, based on sound principles (moment method, dyadic Green's functions) and most importantly, computationally efficient.

While the FEM with a slicing scheme has not been abandoned, the attractive aspects of the new limited mode model (LMM) justify an aggressive effort, aimed at creating a practical tool for analysis of realistic engine faces. Surprising simplifications fall out naturally from the method once the inherent symmetries of the engine face are incorporated directly into the core of the model. At the heart of this method is a limited eigenfunction expansion of the dyadic Green's function for the interior of a cylindrical waveguide. Under single mode excitation, the dyadic Green's function becomes a singly (not doubly) infinite series, making its computation highly efficient. Also, the angular variation of the current is transferred to the basis functions since there are only a limited number of possible angular variations (limited modes), thus greatly reducing the number of degrees of freedom in the model.

In this report, we describe in detail the limited mode model, including the limited mode dyadic Green's function and the expansion of the current into limited modes We also discuss implementation issues relating to basis functions, surface mesh requirements, and the various ways of handling the sheet singularity of the dyadic Green's function. By comparing the relatively low cost of the preliminary results given by this method as compared to their FEM counterparts, it is hoped that the power and flexibility of this new technique is conveyed.

2.0 Development of the Limited Mode Model

The phenomenon of limited mode coupling was uncovered while developing a slicing scheme for the FEM analysis of the engine face. It was found that under single mode excitation, inter-modal coupling can occur only over a very limited set of mode indices

$$n_{out} = n_{in} \pm kN_s \tag{1}$$

where k is any integer and N_s is the symmetry number of the termination (number of blades), n_{in} is the first index (angular dependance) of the incident mode, and n_{out} is the first index of the scattered modes.

In practice, the model must account for multiple sections, each with a different symmetry number, a change in radius of the inlet, and the presence of non-metallic materials. Consider the engine face configuration shown in Figure 1. This configuration indicates all of the crucial features that are present in a realistic engine face and each of these features will be addressed as the limited mode model is formulated in the following.

To begin, consider the general case of a metal/material obstacle within a cylindrical waveguide (see Figure 2.) This scattering problem can be formulated using variational methods outlined in [1] and has been implemented for the rectangular guide in [2]. If the obstacle is metallic, only electric currents on the surface Ω need be considered. The electric field from a distribution of electric surface current within the cylindrical guide is given by

$$\bar{E}(\bar{r}) = \oint_{\Omega} \bar{\bar{G}}(\bar{r}/\bar{r}') \cdot \bar{J}(\bar{r}')\, ds' \tag{2}$$

where $\bar{\bar{G}}(\bar{r}/\bar{r}')$ is the electric dyadic Green's function for the interior of the cylindrical waveguide and is a solution of

$$\nabla \times \nabla \times \bar{\bar{G}}(\bar{r}/\bar{r}') - k_0^2 \bar{\bar{G}}(\bar{r}/\bar{r}') = \bar{\bar{I}}\delta(\bar{r} - \bar{r}') \tag{3}$$

subject to the boundary conditions at the walls of the guide and the radiation condition.

The dyadic Green's function for the cylindrical waveguide can be represented as an eigenfunction (modal) expansion [3] which includes all waveguide modes traveling in either direction away from the source, viz.

$$\bar{\bar{G}}(\bar{r}/\bar{r}') = -\frac{1}{2}\sum_{n=-\infty}^{\infty}\sum_{p=0}^{\infty}\{\bar{E}^{+/-}_{TE_{n,p}}(\bar{r})\,\bar{E}^{-/+}_{TE_{-n,p}}(\bar{r}') + \bar{E}^{+/-}_{TM_{n,p}}(\bar{r})\,\bar{E}^{-/+}_{TM_{-n,p}}(\bar{r}')\} - \frac{\hat{z}\hat{z}}{j\omega\varepsilon_0}\delta(\bar{r}-\bar{r}') \tag{4}$$

The superscript + indicates that a mode is traveling in the +z direction($\bar{E}^{+} \propto e^{-j\beta(z-z')}$), and the superscript - corresponds to a mode traveling in the -z direction ($\bar{E}^{+} \propto e^{+j\beta(z-z')}$). The upper signs are for the case $z > z'$ and the lower signs are for the case $z < z'$.

If $\bar{J}(\bar{r}')$ represents an unknown induced current distribution on the metallic obstacle due to some incident field $\bar{E}^{inc}$, enforcement of the boundary condition $\hat{n} \times (\bar{E}^{inc} + \bar{E}^{s}) = 0$ on the surface of the obstacle gives

$$\hat{n} \times \bar{E}^{inc}(\bar{r}) = -\oint_{\Omega} \hat{n} \times \bar{\bar{G}}(\bar{r}/\bar{r}') \cdot \bar{J}(\bar{r}')\,ds' \tag{5}$$

To construct a discrete system from (5), the current is first expanded as

$$\bar{J}(\bar{r}') = \sum_{i=1}^{N_i} I_i \bar{J}_i(\bar{r}') \tag{6}$$

and inserted into (5). Both sides are then multiplied by the testing functions $\bar{J}_j(\bar{r})$ and integrated over the surface of the obstacle, resulting in the following integral equation (electric field integral equation)

$$\oint_{\Omega} \bar{J}_j(\bar{r}) \cdot \bar{E}^{inc}(\bar{r})\,ds = -\sum_{i=1}^{N_i} \oint_{\Omega}\oint_{\Omega} \bar{J}_j(\bar{r}) \cdot \bar{\bar{G}}(\bar{r}/\bar{r}') \cdot \bar{J}_i(\bar{r}')\,ds'ds \qquad j = 1, 2, 3 \ldots N_i \tag{7}$$

Solution of the linear system given by (7) yields the induced electric current on the obstacle which can be used to find the coefficients of the scattered modes.

This method is known to have poor performance because of the slow convergence of the doubly infinite series involved in the computation of $\overline{\overline{G}}$ [2].

We will now specialize the formulation to a cylindrical guide with an obstacle having discrete angular symmetry. Using the limited mode phenomenon, the doubly infinite series will become a singly infinite series. Also, the angular variation of the current will be transferred to the basis functions since we know *a-priori*, that a limited set of possible angular variations are present in the solution. Thus, the problem will be effectively reduced from full three dimensions to that of a discrete body of revolution.

In order to exploit the limited mode phenomenon, it is necessary to use cylindrical waveguide modes having exponential angular dependance. These modes will be called corkscrew modes since their polarization vector rotates as they travel down the guide. When the dyadic Green's function is expressed using corkscrew modes it is important to keep the sense of rotation consistent with the requirements of reciprocity. The reciprocity relation

$$[\overline{\overline{G}}(\bar{r}/\bar{r}')]^{T} = [\overline{\overline{G}}(\bar{r}'/\bar{r})] \tag{8}$$

must be maintained and therefore the sense of the modes (RH or LH) must be the same for incoming and outgoing modes (see Figure 3.) This is the reason for the change of sign in the first mode index (n) for incoming and outgoing modes in (4).

Under single mode excitation, the scattered field generated by the termination will be a sum of inward and out-going limited modes whose index is given by (1). It then follows that the dyadic Green's function expression (2) is limited in the same way and consequently we can decimate the first series in (4) to include only the physically possible modes. The order of the discrete body of revolution model is adjustable with the single parameter k. For a zeroth order model, $k = 0$ and only one term of the series in (4) is used, namely the $n = n_{in}$ term where n_{in} is the mode index of the incident mode. The termination must be excited by both RH and LH incoming modes separately. However, scattered modes generated by the termination must be of the opposite sense when scattered back (in the +z) direction and must have the same sense when scattered in the forward direction (-z). In this way the series includes only either +n or -n terms but not both. Also,

any limited mode given by (1) that includes a sign change is not a physically possible mode and is not included.

Corkscrew modes make the computation of the frequency modulation from the engine a post-processing step. This is accomplished by simulating the rotating engine with a series of discrete steps. Rather than resolving the problem for the new blade positions, a simple phase shift is introduced into each modal excitation, thus rotating the mode with respect to the engine face. In this way, once the scattering matrix is computed, the far field scattering patterns for different blade positions can be found directly. The modulation of the radar return can then be found, and transformed to compute the doppler frequencies if desired.

An additional simplification to the computation is introduced by expanding the current as

$$\bar{J}_{i,n}(\bar{r}') = \sum_{i=1}^{N_i} I_{i,n} \bar{J}_i(\bar{r}')\, e^{jn\phi} \tag{9}$$

and using testing functions of the form

$$\bar{J}_{j,m}(\bar{r}) = \overline{\bar{J}^*}_{i,n}(\bar{r}') = \bar{J}_j(\bar{r}')\, e^{-jm\phi} \tag{10}$$

where m and n each take on every limited mode index independently. Note that for a 0'th order model, the excitation vector becomes purely real.

Since the angular variation of the problem is built into the solution, the computational domain of the problem need only be a single slice of the termination. More explicitly, there is no need to enforce a phase boundary condition as was done for the FEM solution since the Green's function incorporates the expected periodic angular behavior. This is of considerable practical value since the implementation of the phase boundary condition for curved blades is restricted to cases where a coincident mesh boundary can be achieved.

The next feature of a realistic engine configuration that will be considered is the multiple stages. We will consider that three separate sections must be included in a practical model, the first with body of revolution symmetry (the cone) followed by a front frame and then a compressor section. Behind the first compressor section we will allow for either a short or an open (infinite guide.) The interactions of the multiple sections can be addressed in two ways (see Figure 4.) In the first method, the limited mode coupling is extended to the mul-

tiple sections directly by considering that any traveling mode generated in one section must also meet the limited mode requirements of the adjacent section. For example, the scattered modes are further limited by

$$n_{out} = n_{in} \pm k \cdot LCM(N_{s2}, N_{s1}) \tag{11}$$

for left-going traveling modes generated in section 2, where $LCM(x, y)$ indicates the least common multiple of x and y. For example, the least common multiple of 2 and 4 is 4, and the least common multiple of 10 and 15 is 30. Evanescent modes in one section are not restricted by the symmetry of adjacent sections.

Using this approach, the limited mode coupling is used to further reduce the terms in the Green's function and to further limit the number of current modes required. The entire problem for the coupled sections is then solved as a single system. The size of this system may become awkwardly large however and a more efficient scheme is necessary for large problems. the second method addresses this problem.

In the second method for handling multiple sections, the scattering matrix for each section is generated and partitioned as

$$S = \begin{bmatrix} S_{11} & S_{12} \\ S_{21} & S_{22} \end{bmatrix} \tag{12}$$

Each partition in (12) is a generalized scattering matrix and must contain evanescent as well as traveling modes. The scattering matrices of the three sections can be cascaded to find the net scattering matrix of the entire termination. This method requires the storage of the intermediate scattering matrices but requires the numerical solution of single sections at a time making the method more efficient for large problems.

The last two features of the realistic engine face that are to be addressed are the change in inlet radius and the introduction of materials. A first order approximation to the effects due to the change in radius is introduced by assuming that the change in radius is a small fraction of the radius itself

$$\Delta r << \mathrm{r} \tag{13}$$

With this, we can assume that the same set of traveling modes exist in each cross section and the change in radius simply alters the propagation constant and mode pattern of a mode as it travels through the change in radius. This effect is introduced into the formulation by simply changing the radius in the calculation of the modes within the Green's function for different positions in the guide. Note that all of the computations involved in the modal fields are a function of radius. When a constant radius is assumed, all of the the expensive mode computations can be performed once and stored. The introduction of a change in radius adds considerable expense to the calculation, increasing matrix fill time or requiring substantially more storage.

Materials can be introduced into the formulation using standard moment method techniques. The most efficient technique being the inclusion of surface currents at material interfaces between coatings or the inclusion of equivalent volume currents for inhomogeneous regions. See, for example, [1] pp. 597-598.

3.0 Implementation Considerations

The limited mode model has been implemented for a one, two or three section engine face with or without a short termination at the back. The coupling of the sections has been modeled using method 1 (of Figure 4.) The same code can be used to model the cascaded sections using method 2. It is anticipated that for realistic problems, method 2 will be the only practical means of solution since the system sizes will be too large using method 1.

Two important implementation concerns that are unique to this method are: the handling of the sheet singularity of the dyadic Green's function for the cylindrical guide, and the requirements of the mesh and basis functions in order to achieve a well conditioned, stable system capable of giving robust solutions.

3.1 Sheet Singularity of the Dyadic Green's Function

The singularity of the dyadic Green's function is different from the singularity of the scalar Green's function in two ways. First, the eigenfunction representation of the dyadic Green's function inherently replaces an infinitesimal current at a point with a sheet current [4] (see Figure 5), where the dyadic Green's function is singular at all points on $z = z'$. In the conventional language of moment methods, all pairs of elements on $z = z'$ are self

cells. The second difference from the scalar Green's function is that the singularity is expressed as a divergent infinite series rather than an analytic function. In fact, as $z \rightarrow z'$ the number of terms required for convergence of the series increases dramatically. Physically, this is due to the evanescent modes which become increasingly important as one approaches the source.

There are three techniques for handling the singularity of the dyadic Green's function:

1) Move the observation contour slightly (some distance ε_z) away from the integration contour and simply compute enough terms in the series to achieve convergence.

2) Use a partial summation technique to reduce the infinite series (in p) into closed form.

3) Find an analytic function expressible as cylindrical waveguide modes that can be subtracted from the divergent series, numerically integrated and the added back in and analytically integrated.

The first technique is practical from an engineering point of view but requires some justification. By studying the behavior of the solution of the shorted cylindrical guide problem, it is found that the number of terms required for convergence of the dyadic Green's function is given by

$$\text{number of terms} \approx \frac{1}{\varepsilon_z} \tag{14}$$

where ε_z is expressed in wavelengths (see Figure 6.)

It is important now to consider what error is introduced into the solution as the observation contour is moved farther away from the source. The phase error introduced into the solution is seen to be rather insensitive to a small change in ε_z and in fact shows that for a separation of as much as $\lambda/10$ the phase error is not appreciable.

The second technique of handling the singularity is to partially sum the series in p. This technique is briefly outlined in [1] (pp. 366-367) and it is demonstrated that partial summation can be used only at the expense of a numerical, infinite integration in the spectral domain. This technique is not practical for this problem.

The third technique is perhaps the most elegant and potentially powerful method for handling the singularity, however not yet complete. Currently, only method 1 has been successfully implemented.

3.2 Basis Functions and Mesh Considerations

The choice of basis functions, shape of the discrete elements and restrictions on the mesh all have profound impacts on the condition of the resulting system and the robustness of the overall scheme. For a practical interface with external CAD models, it is desired that a faceted representation of the surface be analyzed. Specifically, triangular facets have been used for the implementation of the technique as triangularly faceted engine face models currently exist. Given this restriction, piecewise constant currents or linear, overlapping edge currents [5] can be used as a basis.

Piecewise constant current elements have been implemented using orthogonal pairs of currents on each facet. The orientation (rotation with respect to the element normal) is adjustable in each element as a parameter. In this manner, the current directions can be chosen in an optimal direction, giving rise to a well conditioned system. If an arbitrary orientation is used for the orthogonal current density pairs, poorly conditioned systems may result since the limited mode Green's function may be nearly orthogonal to some of the currents.

A good choice for the current orientations is to use the incident field as a guide. Two orthogonal directions are chosen that optimally overlap with the direction of the incident field at the center of each element (see Figure 7.) In the event that the incident field is normal to a face (as is the case for elements along a straight blade under TE_{01} incidence), the current directions are chosen to be bisected instead by the projection of the incident magnetic field at the element centroid. These are by no means optimum choices but are sufficient to guarantee that the system is not nearly singular.

The use of overlapping edge-based elements [5] fixes the current directions as specified by the edges of the mesh. That is, the current is expanded by a piecewise linear function, overlapping at element boundaries, in a direction orthogonal to the edge. In the event of a poorly conditioned system, that may be due to one or a few poorly positioned elements, there is no recourse but to generate a new mesh. Unfortunately, potential CAD descrip-

tions of engine faces may not allow this luxury. Given this, piecewise expansions have been implemented in the software, along with the scheme outlined for determining optimum current directions.

As discussed, we do not wish to put excessive constraints on the mesh in order to achieve a well conditioned system since it is desired to make use of a faceted model of the structure. Since the angular dependance of the current has been transferred to the basis functions, it is necessary to group together some elements that lie approximately on the same arc together. In this way, redundant current elements can be eliminated from the solution which would otherwise degrade the condition of the system. These redundant current elements are any elements that lie approximately on the same z and ρ. Ideally, this formulation calls for elements that are stretched out in the ϕ direction as much as possible. For example the mesh for a short would ideally be made of elements shaped as thin arcs. But practically, we must make use of a triangular faceted model, of which, many elements are redundant (see Figure 8.)

For a given current mode (n), only one element along an arc is necessary, even though there are many elements whose centroids are within some $\Delta\phi$ of each other. Therefore, when testing with the conjugate current mode ($n = m$), only one pair of elements from the group forming a constant ρ slice is needed. All other pairs of elements are approximately equivalent. When, the testing and integration modes are different ($n \neq m$) there are no redundant elements and thus all pairs of elements are required.

4.0 Preliminary Results/Computational Cost Comparisons

Consider the three configurations shown in Figure 9 for comparing the computational costs associated with the limited mode model as compared to FEM. Accurate scattered field results were obtained for the short only as the simplistic method for extracting the Green's function singularity proved inadequate for the other geometries. Of most importance is the drastic difference in the number of degrees of freedom (DOFs) required for the two models. While the FEM analysis requires a full 3-dimensional mesh, the LMM analysis requires only a slice of the surface mesh.

5.0 Future Work Schedule

Without analytical extraction of the sheet singularity in the Green's function, the limited mode method will have no practical value. It is imperative then that all near future efforts be directed towards this aim. Extraction of the singularity will represent an important contribution to the general body of literature as well as to the success of this project. Two months of work will be dedicated to this problem and since this is the only element of the code that has not been implemented to date, it is anticipated that once an efficient singularity extraction technique is found, the code will be ready for validation with measured data. The future work is scheduled as:

- Dec. 94 -> Jan. 95: Analysis/extraction of sheet singularity

- Feb. 95: Implementation of singularity extraction/validation with measurements.

- Mar. 95 - Apr. 95: Implementation of LMM extensions (small change in inlet radius, materials, doppler frequency calculations)

- May. 95 -> Aug. 95.: Interface with XPATCH

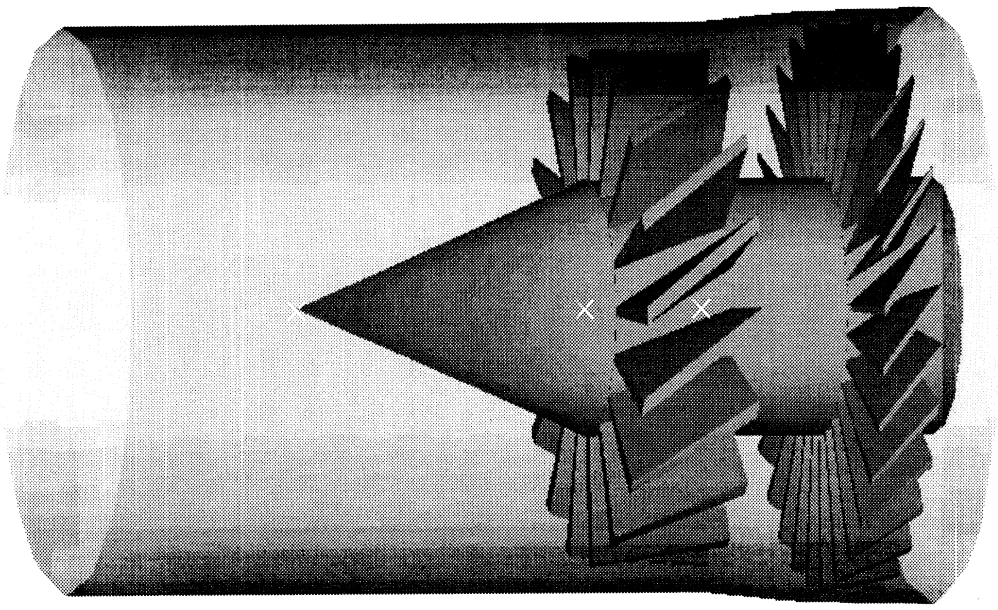

IMPORTANT FEATURES

- Separate sections with different angular symmetry
- Change in inlet radius
- Material coatings

FIGURE 1. Configuration of a realistic engine face showing important features that must be modeled.

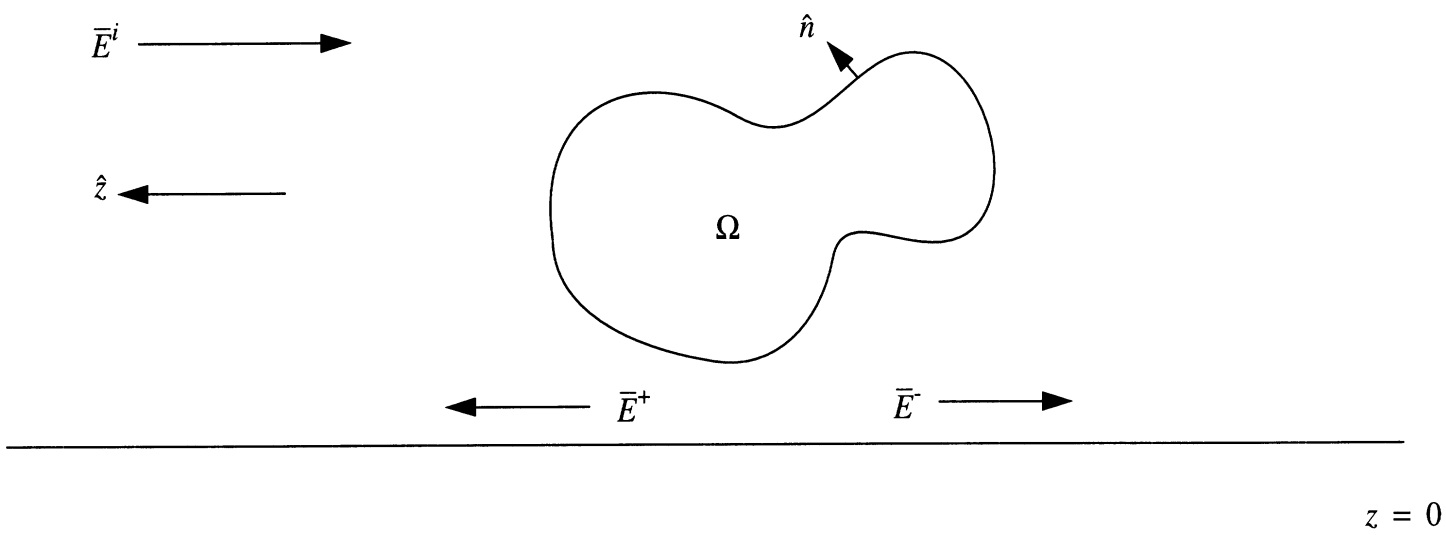

FIGURE 2. General formulation for computing the scattering from an obstacle in a waveguide.

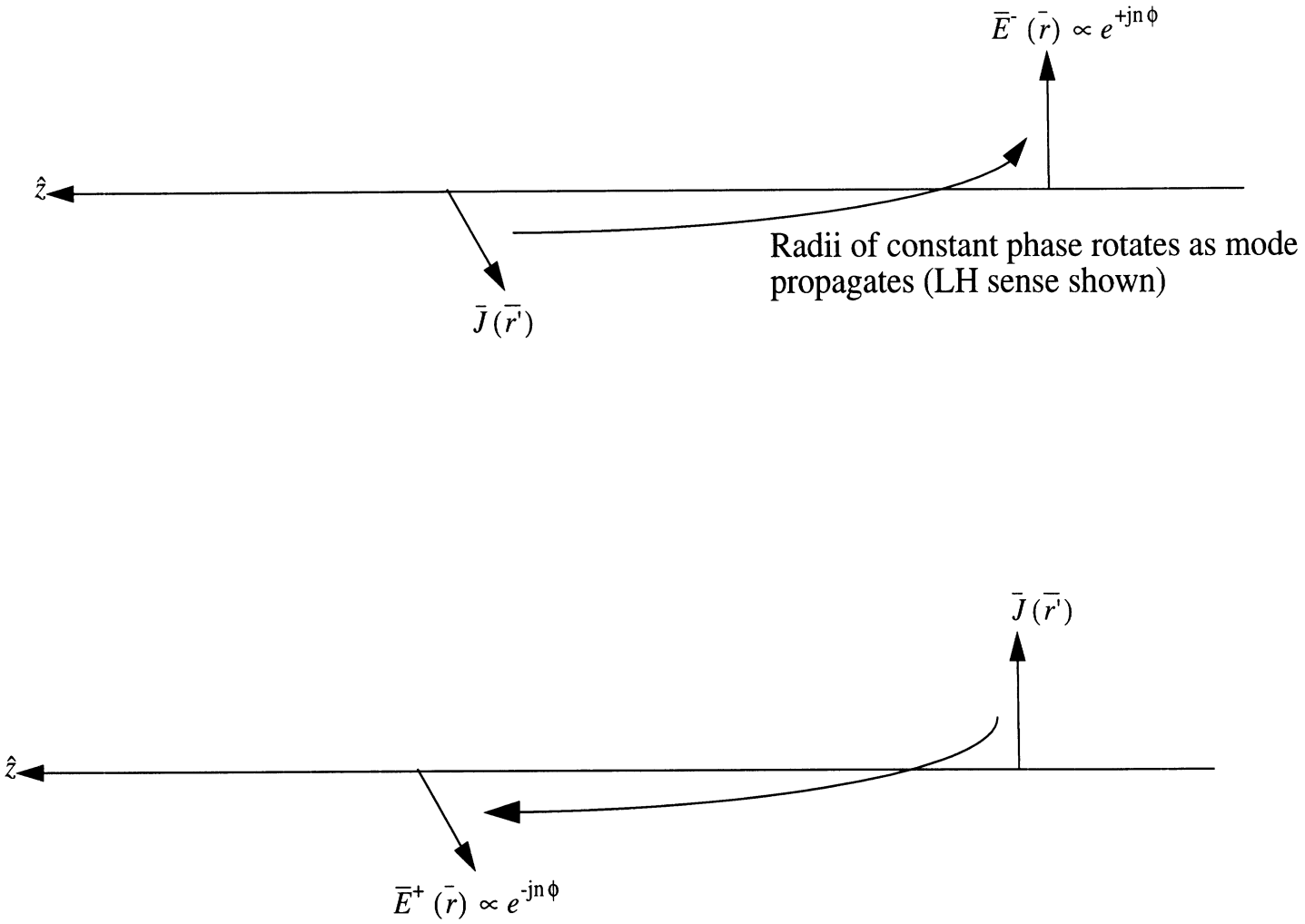

FIGURE 3. Reciprocity of dyadic Green's function with corkscrew modes.

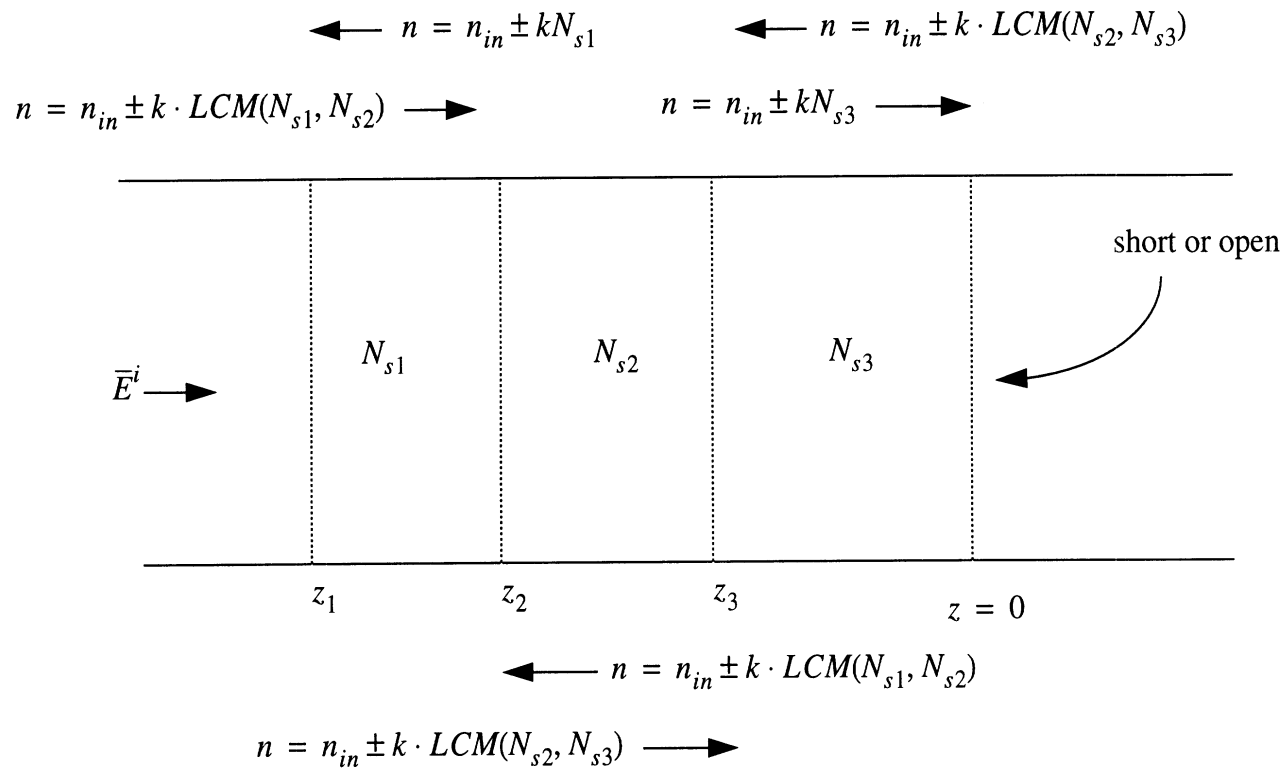

METHOD 1: Solve coupled system using coupled limited travelling modes in cascaded engine face.

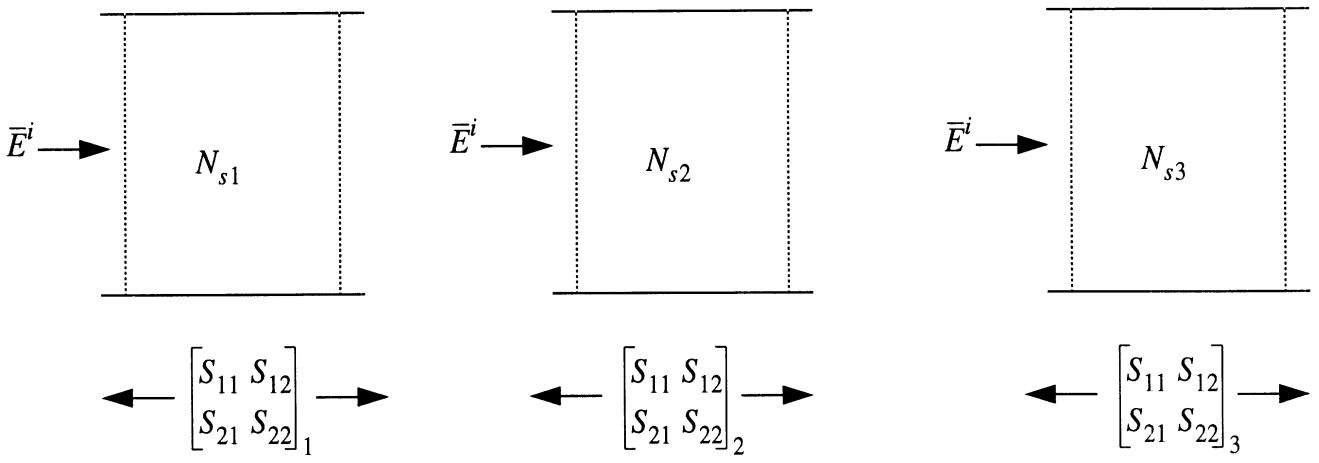

METHOD 2: Solve each section independently and cascade scattering matrices.

FIGURE 4. Two ways of modeling multiple sections with different symmetry numbers

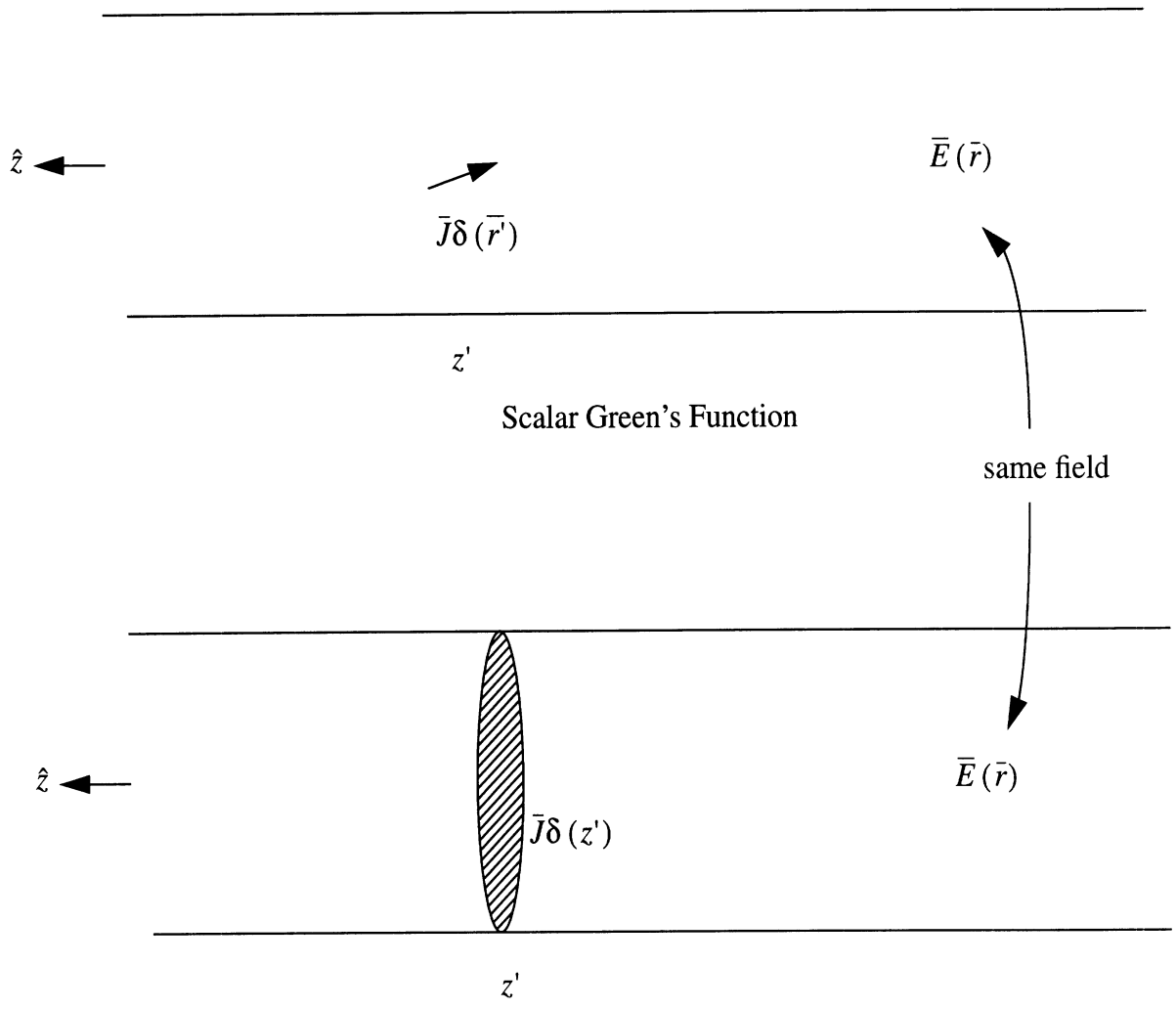

Modal Dyadic Green's Function: Equivalent Sheet Current

FIGURE 5. Equivalent sheet current representation of delta source for dyadic Green's function.

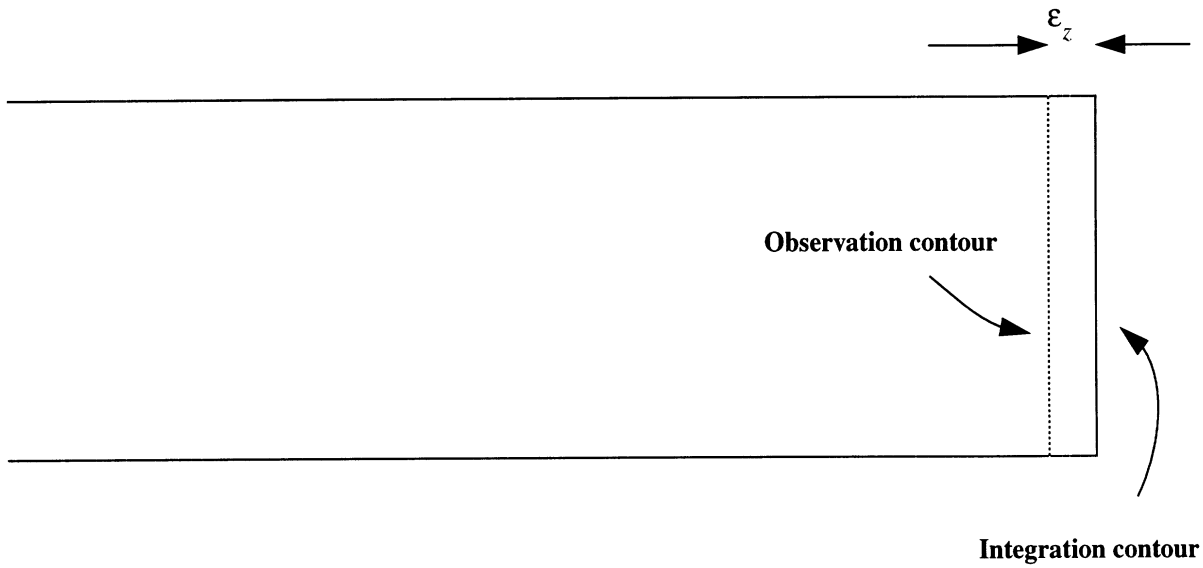

FIGURE 6. Displacement of observation boundary for handling the singularity of the Green's function

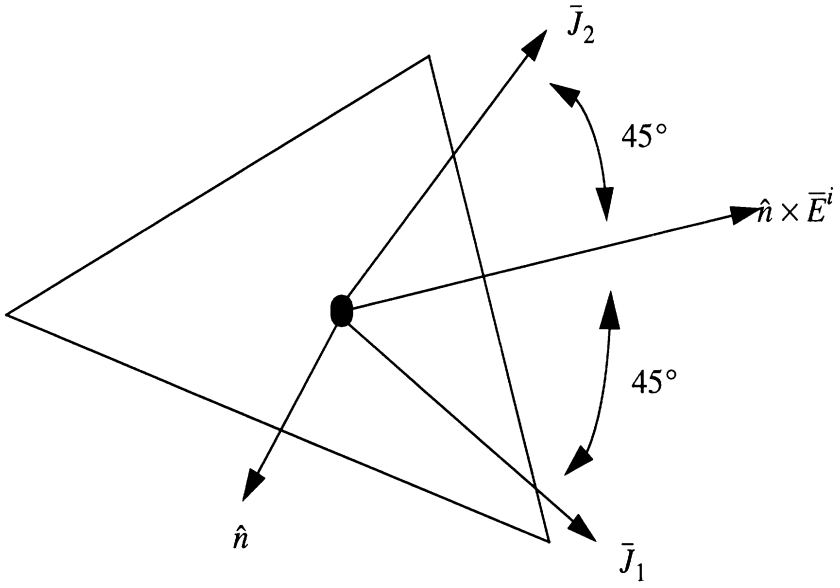

FIGURE 7. Optimal choice of current basis directions.

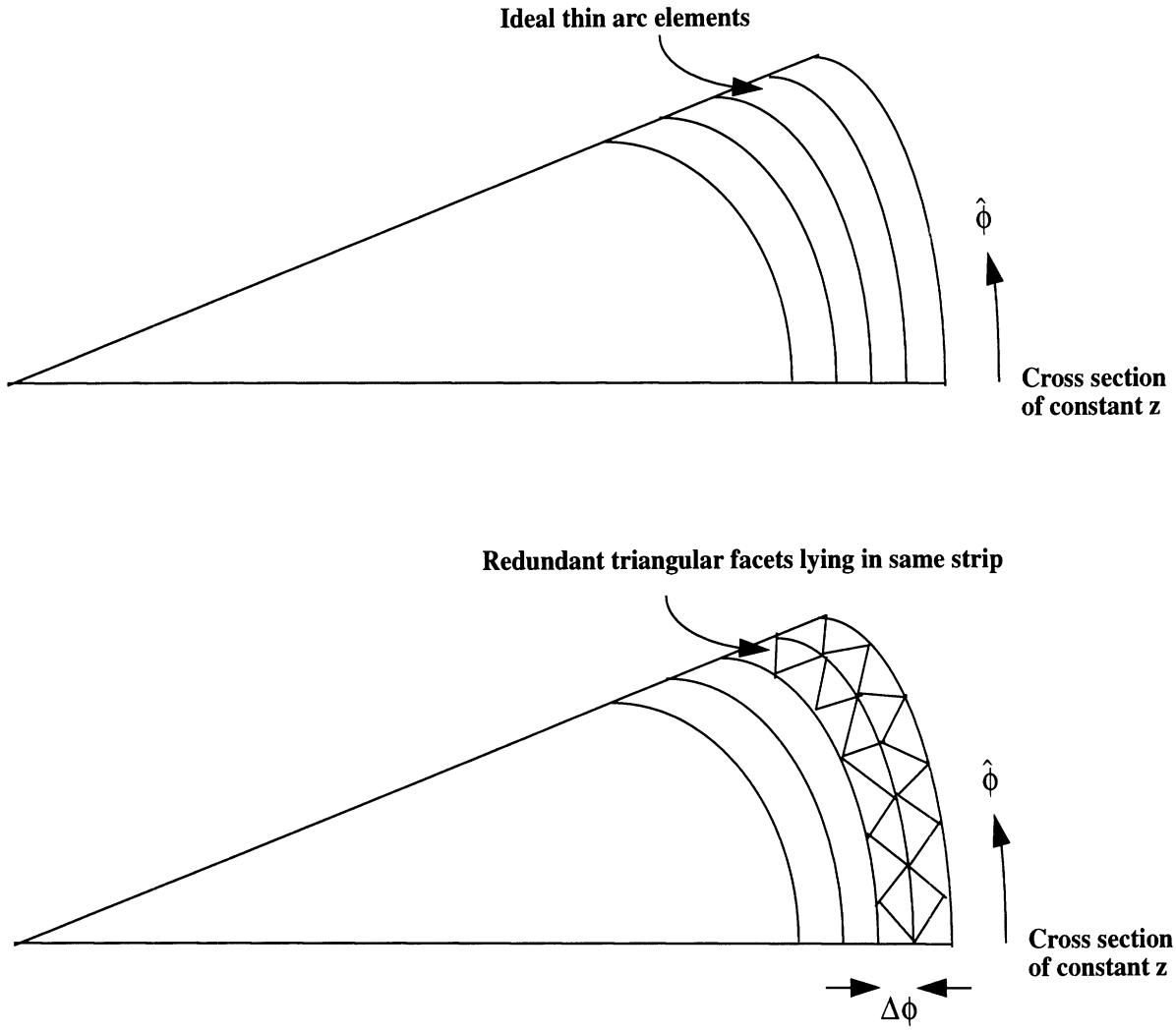

FIGURE 8. Redundant elements

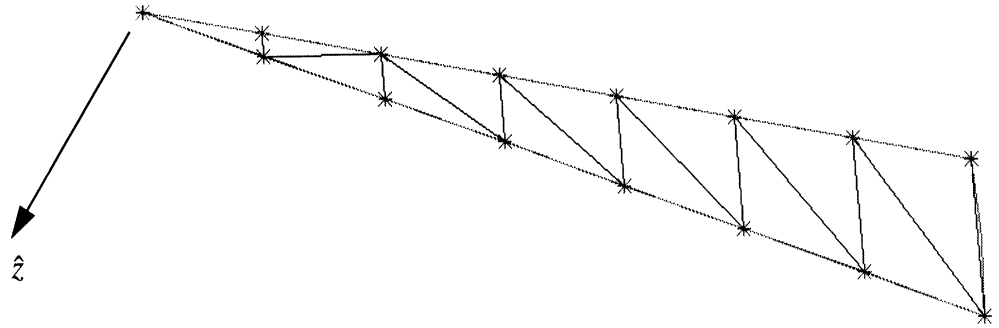

DOFs	
FEM	LMM
10,551	26

SHORT ($r = 0.66\lambda$)

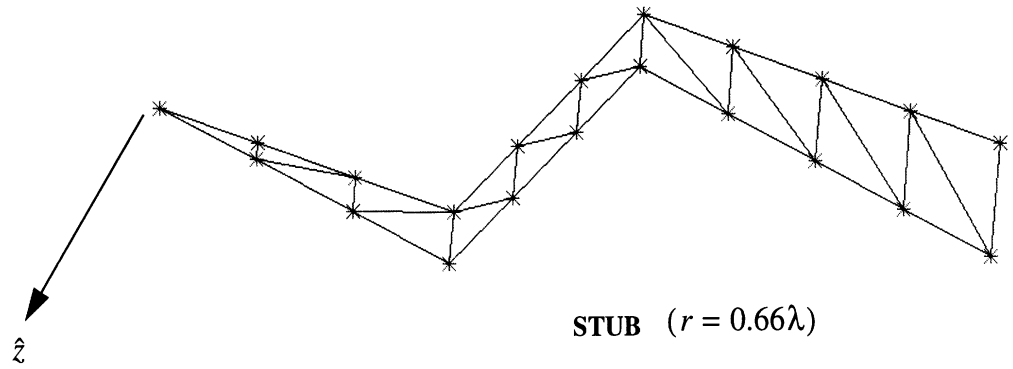

DOFs	
FEM	LMM
14,199	38

STUB ($r = 0.66\lambda$)

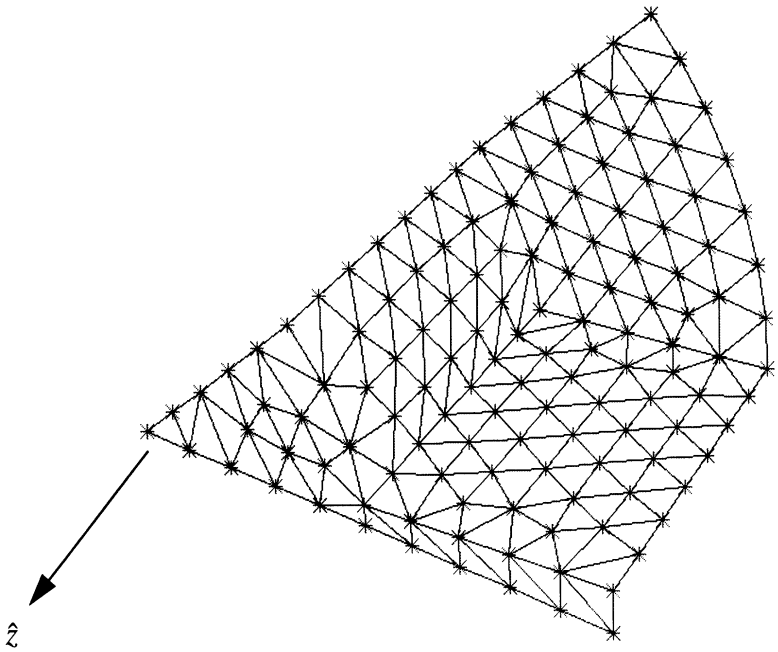

DOFs	
FEM	LMM
23,769	444

EIGHT STRAIGHT BLADES ($r = 1\lambda$)

FIGURE 9. Some limited mode method meshes and comparisons of costs to FEM

References

[1] Robert E. Collin, "Field Theory of Guided Waves", second edition, IEEE Press, New York, 1991.

[2] Johnson J.H. Wang, "Analysis of a Three-Dimensional Arbitrarily Shaped Dielectric or Biological Body Inside a Rectangular Waveguide", *IEEE Transactions on Microwave Theory and Techniques* , vol 26, no. 7, July 1978.

[3] Chen-To Tai, "Dyadic Green Functions in Electromagnetic Theory", second edition, IEEE Press, New York, 1994

[4] Chen-To Tai, "Equivalent Layers of Surface Charge, Current Sheet, and Polarization in the Eigenfunction Expansions of Green's Functions in Electromagnetic theory", *IEEE Transactions on Antennas and Propagation,* vol. 29, no. 5, September 1981.

[5] S.M Rao, D.R. Wilton, and A.W. Glisson, "Electromagnetic Scattering by Surfaces of Arbitrary Shape", *IEEE Transactions on Antennas and Propagation,* vol. 30, no. 3, May 1982.